Entrance Channel Correlations in ^{40}Ca

Jeffrey Scott Bull

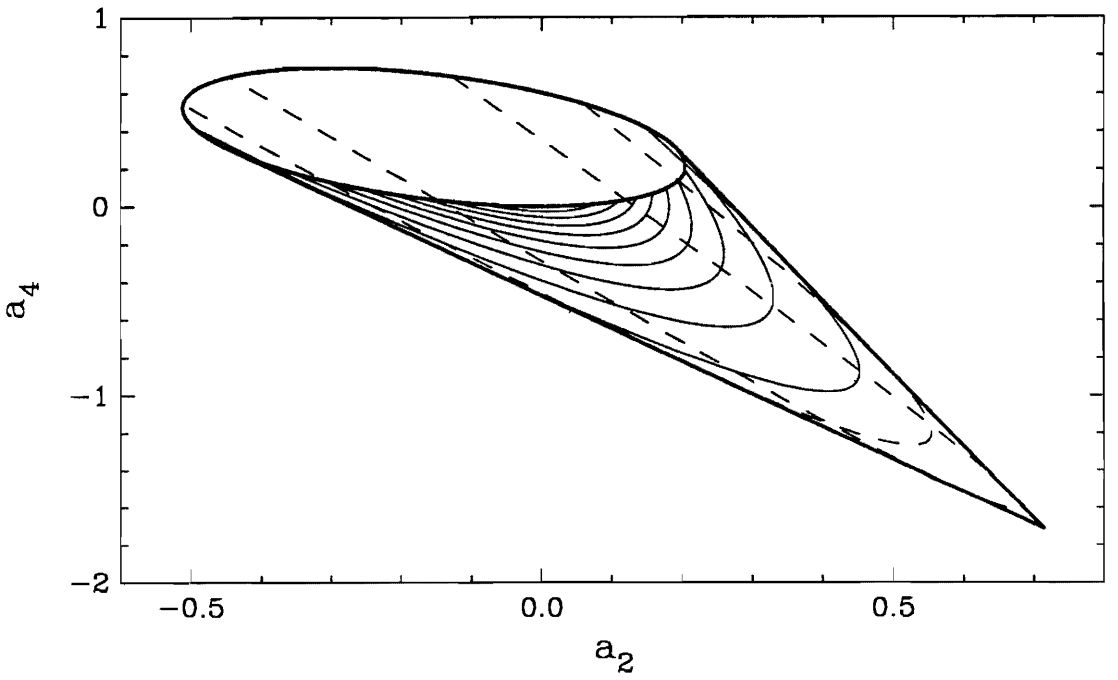

Triangle Universities Nuclear Laboratory

Department of Physics

Duke University

1989

ENTRANCE CHANNEL CORRELATIONS IN ^{40}Ca

by

Jeffrey Scott Bull

Department of Physics
Duke University

Date: April 6, 1989

Approved:

Edward G Bilpuch
E. G. Bilpuch, Supervisor

Richard L Walter

H Weller

Frank DeSucie

Cameron Howell

Dissertation submitted in partial fulfillment of the requirements
for the degree of Doctor of Philosophy in the
Department of Physics in the Graduate
School of Duke University

1989

ABSTRACT

(Physics-Nuclear)

ENTRANCE CHANNEL CORRELATIONS IN ^{40}Ca

by

Jeffrey Scott Bull

Department of Physics
Duke University

Date: April 6, 1989

Approved:

Edward S. Bilpuch
E. G. Bilpuch, Supervisor

Richard L. Walter

H. Russell Robertson

Frank DeJarnette

Lawrence Cranberg

An abstract of a dissertation submitted in partial fulfillment of
the requirements for the degree of Doctor of Philosophy
in the Department of Physics in the Graduate
School of Duke University

1989

ABSTRACT

Angular distributions and excitation functions of the $^{39}K(p,\alpha_0)$ reaction were measured for 68 resonances in the proton energy range $E_p = 2.2$ MeV to 4.0 MeV. This experiment was performed with an overall energy resolution of 350 eV to 400 eV (FWHM) at the Triangle Universities Nuclear Laboratory KN Van de Graaff accelerator.

Angular correlation methods were used to derive expressions for the $^{39}K(p,\alpha_0)$ angular distributions. For several of the 2^+ resonances, the experimental angular distributions yielded two possible solutions for the proton partial reduced widths. These solutions were then compared with the elastic scattering data to determine the correct solution. Three sets of reduced widths and one pair of reduced width amplitudes were obtained for 30 of the 2^+ resonances. For the 1^- resonances, the angular distributions and excitation functions did not provide sufficient information to uniquely determine the reduced widths, although detailed spectroscopic information was obtained for 13 resonances.

Statistical analyses were performed on the 2^+ reduced widths and amplitudes. The proton partial widths agree well with the Porter-Thomas distribution. There are strong width correlations between two of the three proton channels and between the γ_{20} and γ_{22} reduced width amplitudes. These data were transformed into the zero representation; again there is a strong width correlation. These channel correlations are interpreted as evidence for direct reactions. These data are the first results on entrance channel width and amplitude correlations.

ACKNOWLEDGMENTS

I would like to thank my advisor, Dr. E. G. Bilpuch, for his support and encouragement during my graduate studies. The assistance of Dr. J. F. Shriner, Jr. towards the completion of this project is also appreciated. I am also very grateful to Dr. G. E. Mitchell for many helpful discussions and guidance in the preparation of this dissertation.

I am indebted to C. R. Westerfeldt for the instruction and guidance he has given me as well as for his maintenance of the accelerator and computer systems. I also wish to thank Dr. W. K. Brooks, Dr. D. Fang, and Dr. J. R. Vanhoy for their helpful discussions and assistance in completing this experiment. Hats off to B. Smith, L. James, K. Keeter, S. Frankle, and C. Frankle for their help in taking the data.

The assistance of S. E. Edwards, R. Rummel, P. Carter, and P. Mulkey in the maintenance of the electronics and accelerator systems is gratefully acknowledged. The excellent work of the machine shop, headed by A. W. Lovette, is appreciated.

I am thankful for the support and guidance of my family throughout my life.

This work was supported in part by the United States Department of Energy.

TABLE OF CONTENTS

APPENDICES

LIST OF FIGURES

LIST OF TABLES

ENTRANCE CHANNEL CORRELATIONS IN ^{40}CA

CHAPTER I

INTRODUCTION

For a number of years the High Resolution Laboratory of the Triangle Universities Nuclear Laboratory has studied the properties of proton resonance reactions. Early measurements with cyrogenic gas targets yielded an overall energy resolution of 100 eV. Although changing to thin foil targets dramatically increased the number of nuclei accessible to study, the overall resolution of the system was degraded to approximately 300 eV. This increase is due in large part to the Doppler broadening effect in the solid targets.

The earliest applications of the high resolution system were for the study of the fine structure of isobaric analog states. In these experiments, excitation functions for proton elastic scattering were measured and the resonance analysis performed in terms of *R*-matrix parameters. The result was a large library of spectroscopic information on proton resonances. The first nuclei studied were even-even nuclei in the mass range $40 \leq A \leq 60$; these experiments are reviewed in Bilpuch *et al.* (1976). More recently, these proton resonance experiments were extended to nuclei with non-zero spin. These analyses were made possible by the availability of increased computer power, which is required to analyze the more complicated resonance reactions that occur on these nuclei.

A series of parallel experiments at this laboratory have focussed on the statistical properties of nuclei, such as reduced width and amplitude distributions, and channel correlations. Statistical models of the compound nucleus based on random matrix theory predict that the reduced width amplitude distributions should be Gaussian, and that the

width correlation between channels is the square of the amplitude correlation. While a general R-matrix analysis of reaction cross sections will provide the resonance reduced widths, a more complicated procedure (which was developed at this laboratory) is needed in order to determine the reduced width amplitudes. From the angular distributions of the inelastically scattered protons and the associated γ rays from the (p,p'γ) reaction, the relative signs of the reduced width amplitudes for proton resonances were first determined in the mid 1970s. These experiments were the first detailed application of the random matrix model to proton resonances. Since then many additional experiments have been performed; these are reviewed in Mitchell *et al.* (1985). The results of these experiments verified the Gaussian assumption. The strong correlations between the exit channels observed experimentally indicated that direct reactions contributed significantly to the reaction process. More recently, general interest in statistical properties of the nucleus revived after evidence emerged which suggested that the compound nucleus is a quantum chaotic system.

These previous experiments measured only exit channel reduced widths and amplitudes. A method was developed to measure the relative sign of entrance channel amplitudes. Utilizing the polarized proton beam and the FN tandem accelerator at TUNL, Shriner *et al.* (1983b) determined the relative signs of reduced width amplitudes from the angular distribution of the $(\vec{p},\alpha)$ reaction on ^{39}K. Since the polarized beam had a very low intensity, only one resonance was studied. This technique proved impractical for a complete statistical study, which requires many resonances. The present experiment repeats the earlier work, but with unpolarized beam, and measures many resonances in ^{40}Ca. This nucleus was chosen because there are a large number of resonances in the (p,α_0) channel in the E_p = 2 MeV to 4 MeV energy range. The limitation imposed by the unpolarized beam is that the relative signs can be determined for only one of the three pairs of entrance channel amplitudes.

Chapter II briefly discusses the theory of angular correlations as specialized to the (p,α_0) reaction, and presents the (p,α_0) angular distribution equations. In Chapter III, the experimental apparatus and high resolution system are described, along with the data acquisition system and the targets used in this experiment. Chapter IV describes the data analysis and presents the values obtained for the reduced widths and reduced width amplitudes. Statistical properties of these widths and amplitudes are discussed in Chapter V. The results are summarized in Chapter VI.

CHAPTER II

ANGULAR CORRELATIONS AND REACTION CROSS SECTIONS

A. Theoretical Background

Angular distribution measurements of emitted radiation have long provided spectroscopic information about the nucleus. In addition to determining angular momentum values and parities for compound nuclear states, angular correlation studies have been used to determine channel spin and *l*-mixing ratios, from which reduced widths and reduced width amplitudes have been calculated. The early theoretical work concerning angular correlations approached the problem by first constructing wave functions which describe the system, and then using the transformation properties of matrix elements between pure states to derive the angular distribution formulas. However, an experiment usually does not involve particles in pure states, but instead deals with a group of particles in an ensemble of states. In this instance, the derivation of the angular correlation expressions involves the tedious calculation of the sums and averages over unobserved quantum numbers, and thus the angular correlation equations were derived for only a few specific cases (Blatt and Biedenharn (1952), Biedenharn and Rose (1953)). To simplify these calculations, Fano (1953) and Coester and Jauch (1953) independently developed a method to derive the angular correlation formulas using the density matrix. This technique is also discussed by Devons and Goldfarb (1957), Ferguson (1965), and Thompson and van Rij (1968), among others.

In nuclear reactions, the quantum mechanical system consists of a beam of particles hitting a target. Neither of these systems is in a pure state; they can not be represented by a unique wave function. Instead, these systems contain an ensemble of particles in various states, in this case spin polarization states, of which the interaction of the entire ensemble is of interest, not the interaction of the individual particles. Such a collection of states can be expressed as a mixture of pure states, each with a statistical weight assigned to it from the probability of a particle in the ensemble being in that particular state. For example, if a system has probabilities $p_1, p_2, \ldots p_m$, of being in states $|1\rangle$, $|2\rangle$, $\ldots|m\rangle$, then a density matrix, ρ, can be defined in terms of the states and their probabilities

$$\rho = \sum_{\alpha} |\alpha\rangle p_{\alpha} \langle\alpha| . \tag{2.1}$$

One of the properties of the density matrix is that the expectation value of an operator **O** of a system described by the density matrix is the trace of the product of the operator and the density matrix. Thus $\langle \mathbf{O} \rangle = \mathrm{Tr}(\mathbf{O}\rho)$. Also, since the trace of a matrix is unaffected by unitary transformations, the expectation value of an operator is unaffected by the choice of representation of the system.

For angular correlation measurements, the efficiency matrix ε is the operator which relates the system to the particulars of the detection of the outgoing radiation, such as the detector configuration in the scattering chamber. Therefore the probability that a detector will record a scattered particle is

$$\mathbf{W} = \langle \varepsilon \rangle = \mathrm{Tr}(\varepsilon\rho) . \tag{2.2}$$

Thus the problem of determining the angular dependence of the reaction products has been reduced to the problem of deriving the matrices ε and ρ.

Since matrices are difficult to manipulate mathematically, it is convenient to transform the density and efficiency matrices into a set of statistical tensors. The elements of the statistical tensor $\rho_{kn}(B_1 B_2)$, with a representation associated with angular

momenta $\vec{B}_1$ and $\vec{B}_2$, can be expressed in terms of the density matrix ρ by

$$\rho_{kn}(B_1B_2) = \sum_{\beta_1\beta_2} (-1)^{B_2-\beta_2} (B_1\beta_1B_2 -\beta_2|kn)\langle B_1\beta_1|\rho|B_2\beta_2\rangle. \tag{2.3}$$

Here, β refers to the magnetic substates of angular momentum $\vec{B}$, $\vec{k} = \vec{B}_1 - \vec{B}_2$, n ranges from -k to k in integral steps, and $(B_1\beta_1B_2-\beta_2|kn)$ is a Clebsch-Gordan coefficient in the Condon and Shortley (1951) phase convention. Similarly, the efficiency tensor ε can be written

$$\varepsilon_{kn}(B_1B_2) = \sum_{\beta_1\beta_2} (-1)^{B_2-\beta_2} (B_1\beta_1B_2 - \beta_2|kn)\langle B_1\beta_1|\varepsilon|B_2\beta_2\rangle. \tag{2.4}$$

Inverting Eqns. 2.3 and 2.4 and substituting them into Eqn. 2.2 gives

$$\mathbf{W} = \mathrm{Tr}(\varepsilon\rho) = \sum_{B_1B_2kn} \rho_{kn}(B_1B_2)\varepsilon^*_{kn}(B_1B_2), \tag{2.5}$$

utilizing the Hermitian property of the ε matrix.

In several instances, $\vec{B}_1$ and $\vec{B}_2$ are the sum of two other angular momenta. For example, if $\vec{B}_1 = \vec{A}_1 + \vec{j}_1$ and $\vec{B}_2 = \vec{A}_2 + \vec{j}_2$, it is then necessary to express the tensors of Eqn. 2.5 in terms of $\vec{A}_1$, $\vec{A}_2$, $\vec{j}_1$, and $\vec{j}_2$. Since the density matrix of the composite system is the direct product of the density matrices of the two subsystems, it can be shown that the density tensor expands as

$$\rho_{k_Bn_B}(B_1B_2) = \sum_{k_An_Ak_jn_j} (k_An_Ak_jn_j|k_Bn_B)\hat{k}_A\hat{k}_j\hat{B}_1\hat{B}_2 \times \begin{Bmatrix} A_1 & j_1 & B_1 \\ A_2 & j_2 & B_2 \\ k_A & k_j & k_B \end{Bmatrix} \rho_{k_An_A}(A_1A_2)\rho_{k_jn_j}(j_1j_2). \tag{2.6}$$

Here the term in the brackets is a Wigner 9-j symbol and $\hat{k} = \sqrt{(2k+1)}$. Likewise, if either $\vec{A}$ or $\vec{j}$ is the sum of two angular momenta, then the density tensor of that system can also be expanded using Eqn. 2.6. In the same manner, the efficiency tensor $\varepsilon_{k_Bn_B}$

can be expanded into its individual parts. Thus, the angular correlation formula can be found by breaking down Eqn. 2.5 into its basic components and evaluating the remaining tensors.

B. Application to the (p,α_0) Reaction

So far, the discussion of angular correlations has concerned only the concept of angular momentum coupling. To apply this method to compound nuclear reactions, a specific process must be considered. Angular correlations as applied to the $(p,p'\gamma)$ reaction and (p,α_0) reaction have been previously described by Shriner (1983a) and Vanhoy (1986). Ramakrishnan (1984) used angular correlation methods to describe the $(p,p'\gamma)$ reaction when the inelastic proton and the γ ray are measured in coincidence. Here, the derivation for the $^{39}K(p,\alpha_0)^{36}Ar$ reaction is given, closely following the method outlined by Shriner (1983a).

In a nuclear reaction, an incident particle strikes a target nucleus, forming an intermediate state which decays by emitting a particle and leaving a residual nucleus. The channel spin representation will be used here to describe the reaction in terms of the angular momentum (Figure 2.1). Let the incident particle have an intrinsic angular momentum $\vec{i}$ and the target nucleus spin $\vec{A}$. In the channel spin notation, these two angular momenta are coupled to form the channel spin, $\vec{s} = \vec{A} + \vec{i}$. This in turn is coupled with the orbital angular momentum of the projectile $\vec{l}$ to form the compound state $\vec{B} = \vec{s} + \vec{l}$. This state then decomposes to an exit channel spin $\vec{s}'$ and orbital angular momentum $\vec{l}'$, as $\vec{B} = \vec{s}' + \vec{l}'$. The exit channel spin $\vec{s}'$ is in turn composed of the intrinsic spins of the emitted particle $\vec{i}'$ and the residual nucleus spin $\vec{C}$, such that $\vec{s}' = \vec{C} + \vec{i}'$.

It now is apparent how to derive the angular correlation formula. Starting from Eqn. 2.5 apply Eqn. 2.6 twice, splitting $\varepsilon^*_{kn}(B_1B_2)$ into its three parts: $\varepsilon^*_{k_{i'}n_{i'}}(l'_1l'_2)$,

Figure 2.1 Energy level and angular momentum coupling scheme for the $^{39}K(p,\alpha_0)^{36}Ar$ reaction in the channel spin representation.

Angular Momentum Coupling

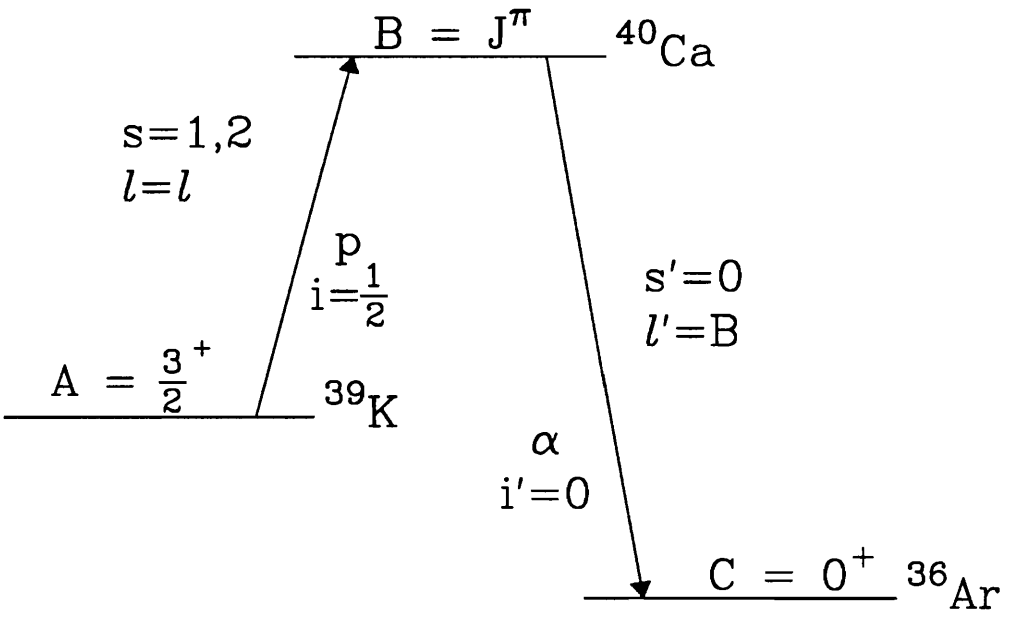

Channel Spin Representation	
Entrance Channel	Exit Channel
$\vec{s} = \vec{A} + \vec{i}$	$\vec{s'} = \vec{C} + \vec{i'}$
$\vec{B} = \vec{s} + \vec{l}$	$\vec{B} = \vec{s'} + \vec{l'}$

$\varepsilon^*_{k_{i'}n_{i'}}(i'_1 i'_2)$, and $\varepsilon^*_{k_C n_C}(C_1 C_2)$. However, the density tensor $\rho_{kn}(B_1 B_2)$ does not break down as simply. This is because the observations made in the laboratory are recorded after the compound nucleus decays, but the density matrix describes the system before the reaction. Let the disintegration of the compound state be described by the interaction operator **O**. The density matrix then transforms as

$$\rho' = \mathbf{O}\rho\,\mathbf{O}^\dagger. \tag{2.7}$$

Assuming **O** conserves angular momentum, this expression can be written in terms of statistical tensors as

$$\begin{aligned}\rho'_{kn}(B_1 B_2) &= \rho_{kn}\left(B_1 s'_1 l'_1 B_2 s'_2 l'_2\right) \\ &= \left\langle B_1 s'_1 l'_1 |\mathbf{O}| B_1 s_1 l_1\right\rangle \rho_{k_B n_B}(B_1 s_1 l_1 B_2 s_2 l_2)\left\langle B_2 s'_2 l'_2 |\mathbf{O}| B_2 s_2 l_2\right\rangle^*\end{aligned} \tag{2.8}$$

Now $\rho_{k_B n_B}(B_1 B_2)$ can be decomposed into its constituent parts: $\rho_{k_A n_A}(A_1 A_2)$ $\rho_{k_i n_i}(i_1 i_2)$, and $\rho_{k_l n_l}(l_1 l_2)$. Substituting in all of these parts, the angular correlation formula becomes

$$\begin{aligned}\mathbf{W} = \sum & \rho_{k_A n_A}(A_1 A_2)\rho_{k_l n_l}(l_1 l_2)\rho_{k_i n_i}(i_1 i_2)\varepsilon^*_{k_C n_C}(C_1 C_2)\varepsilon^*_{k_{l'} n_{l'}}(l'_1 l'_2)\varepsilon^*_{k_{i'} n_{i'}}(i'_1 i'_2) \\ & \times (k_A n_A k_i n_i | k_s n_s)(k_s n_s k_l n_l | k_B n_B)(k_C n_C k_{i'} n_{i'} | k_{s'} n_{s'})(k_{s'} n_{s'} k_{l'} n_{l'} | k_B n_B) \\ & \times \begin{Bmatrix} A_1 & i_1 & s_1 \\ A_2 & i_2 & s_2 \\ k_A & k_i & k_s \end{Bmatrix}\begin{Bmatrix} s_1 & l_1 & B_1 \\ s_2 & l_2 & B_2 \\ k_s & k_l & k_B \end{Bmatrix}\begin{Bmatrix} C_1 & i'_1 & s'_1 \\ C_2 & i'_2 & s'_2 \\ k_C & k_{i'} & k_{s'} \end{Bmatrix}\begin{Bmatrix} s'_1 & l'_1 & B_1 \\ s'_2 & l'_2 & B_2 \\ k_{s'} & k_{l'} & k_B \end{Bmatrix} \\ & \times \hat{k}_A \hat{k}_i \hat{s}_1 \hat{s}_2 \hat{k}_s \hat{k}_l \hat{B}_1 \hat{B}_2 \hat{k}_C \hat{k}_{i'} \hat{s}'_1 \hat{s}'_2 \hat{k}_{s'} \hat{k}_{l'} \hat{B}_1 \hat{B}_2 \left\langle B_1 s'_1 l'_1 |\mathbf{O}| B_1 s_1 l_1\right\rangle \left\langle B_2 s'_2 l'_2 |\mathbf{O}| B_2 s_2 l_2\right\rangle^*.\end{aligned} \tag{2.9}$$

A starting point in simplifying this equation is to derive first the specific density and efficiency tensors used in compound nuclear reactions. For both an unpolarized target and an unpolarized beam, the same number of particles are in each of the $2j + 1$ magnetic substates. Thus the density matrices describing the target and projectile beam are both diagonal, with each element equal to $1/(2j+1)$. These transform into statistical tensors as

$$\rho_{k_A n_A}(A_1 A_2) = \frac{\delta_{k_A 0}\delta_{n_A 0}\delta_{A_1 A_2}}{\hat{A}}; \qquad \rho_{k_i n_i}(i_1 i_2) = \frac{\delta_{k_i 0}\delta_{n_i 0}\delta_{i_1 i_2}}{\hat{i}}. \tag{2.10}$$

Similarly, the polarization states are not known for either the outgoing particles or the residual nuclei, so their efficiency tensors become

$$\varepsilon_{k_{i'} n_{i'}}(i'_1 i'_2) = \frac{\delta_{k_{i'} 0}\delta_{n_{i'} 0}\delta_{i'_1 i'_2}}{\hat{i}'}; \qquad \varepsilon_{k_C n_C}(C_1 C_2) = \frac{\delta_{k_C 0}\delta_{n_C 0}\delta_{C_1 C_2}}{\hat{C}}. \tag{2.11}$$

The incoming and outgoing particles can be represented as plane waves at large distances from the interaction. If the *z*-axis is defined in the direction of the incident beam, it can be shown that

$$\rho_{k_i n_i}(l_1 l_2) = \frac{\hat{l}_1 \hat{l}_2}{4\pi}(-1)^{l_2}(l_1 0 l_2 0 | k_l 0)\delta_{n_l 0}. \tag{2.12}$$

The expression for the efficiency tensor for the outgoing particle is similar, except that it is defined along the direction of propagation of the detected particle. Thus the tensor must be rotated to align the *z*-axis along the incident beam direction. Therefore

$$\varepsilon_{k_{i'} n_{i'}}(l'_1 l'_2) = \frac{\hat{l}'_1 \hat{l}'_2}{4\pi}(-1)^{l'_2}(l'_1 0 l'_2 0 | k_{l'} 0)\delta_{n_{i'} 0}\mathbf{D}^{k_{i'}*}_{n_i n_{i'}}(\alpha\beta\gamma), \tag{2.13}$$

where **D** is the rotation matrix about the Euler angles $\alpha\beta\gamma$. This reduces to

$$\varepsilon_{k_{i'} n_{i'}}(l'_1 l'_2) = \frac{\hat{l}'_1 \hat{l}'_2}{\sqrt{4\pi}\,\hat{k}_{l'}}(-1)^{l'_2}(l'_1 0 l'_2 0 | k_{l'} 0) Y^*_{k_{i'} n_{i'}}(\theta\varphi), \tag{2.14}$$

where *Y* is a spherical harmonic also with the phase convention of Condon and Shortley, and the angles $\theta\phi$ describe the detector position. Substituting in these values for the statistical tensors and simplifying the 9-*j* symbols and Clebsch-Gordan coefficients, Eqn. 2.9 reduces to

$$\mathbf{W} = \frac{1}{16\pi^2 \hat{A}\hat{i}} \sum_{l_1 l_2 B_1 B_2 sk} (-1)^{l_2 + l'_2 + s - l_1 + s' - l'_1} \bar{Z}(l_1 B_1 l_2 B_2; sk)\bar{Z}(l'_1 B_1 l'_2 B_2; s'k)$$

$$\times P_k(\cos\theta)\langle B_1 s_1' l_1' | \mathbf{O} | B_1 s_1 l_1 \rangle \langle B_2 s_2' l_2' | \mathbf{O} | B_2 s_2 l_2 \rangle^* , \quad (2.15)$$

where $\bar{Z}$ is the Z-coefficient defined by Blatt and Biedenharn (1952), as modified by Huby (1954).

These results can now be applied to the specific case of the $^{39}K(p,\alpha_0)^{36}Ar$ reaction (Figure 2.1). In this instance, the spin and parity of the target A is $3/2^+$ and the spin of the projectile i is 1/2. These combine to form channel spins of either 1 or 2. The compound nucleus state is B, which is equal to J. This state decays to the ground state of ^{36}Ar (spin and parity 0^+) by emitting an alpha particle with $i' = 0$. Thus $s' = 0$, and $l'_1 = l'_2 = J$. The angular correlation equation becomes

$$\mathbf{W} = \frac{1}{32\pi^2\sqrt{2}} \sum_{J l_1 l_2 s k} (-1)^{s-l_1-l_2} \bar{Z}(l_1 J l_2 J; s k)\, \bar{Z}(J J J J; 0 k) P_k(\cos\theta)$$
$$\times \langle J s_1' l_1' | \mathbf{O} | J s_1 l_1 \rangle \langle J s_2' l_2' | \mathbf{O} | J s_2 l_2 \rangle^* . \quad (2.16)$$

All that is left is to evaluate the matrix elements of the operator $\mathbf{O}$. For a nuclear reaction of the type described here, $\mathbf{O}$ is the reaction matrix $\mathfrak{R} = \mathbf{S} - \mathbf{1}$, where $\mathbf{S}$ is the scattering matrix of Heisenberg (1943). Biedenharn (1960) has shown that the matrix element is proportional to

$$\langle J s_1' l_1' | \mathfrak{R} | J s_1 l_1 \rangle \propto e^{i(\zeta_{l_1} - \zeta_{l_1'})} \frac{i\sqrt{\Gamma_{s_1 l_1} \Gamma_{s_1' l_1'}}}{E_0 - E - i\frac{\Gamma}{2}} . \quad (2.17)$$

Here E_0 is the resonance energy, Γ_{sl} is the partial width of the resonance in channel sl, Γ is the total width of the resonance, and ζ_l is an energy dependent phase shift which includes both the Coulomb and hard sphere phase shifts. The phase shift ζ_l is defined as

$$\zeta_l = -\tan^{-1}\frac{F_l}{G_l} + \sum_{m=1}^{l} \tan^{-1}\frac{\eta}{m} , \quad (2.18)$$

where F_l and G_l are the regular and irregular Coulomb functions, and $\eta = 0.1574\, Z_0 Z_1 [m/E]^{1/2}$, the Coulomb parameter. Eqn. 2.9 shows that the matrix elements always

appear in the bilinear pair $\langle\,|\mathfrak{R}|\,\rangle\,\langle\,|\mathfrak{R}|\,\rangle^{*}$. Thus

$$\left\langle Js_1'l_1'|\mathfrak{R}|Js_1l_1\right\rangle\left\langle Js_2'l_2'|\mathfrak{R}|Js_2l_2\right\rangle^{*} \propto e^{i\left(\zeta_{l_1}+\zeta_{l_2'}-\zeta_{l_1'}-\zeta_{l_2}\right)}\frac{\sqrt{\Gamma_{s_1l_1}\Gamma_{s_1'l_1'}\Gamma_{s_2l_2}\Gamma_{s_2'l_2'}}}{\left(E_0-E\right)^2+\left(\frac{\Gamma}{2}\right)^2}. \quad (2.19)$$

Since an absolute cross section measurement is not necessary in this experiment, the angular distribution formula can be simplified further by dividing out all overall constants. Then, for an isolated resonance with spin J, the angular correlation equation reduces to

$$\mathbf{W}_{\alpha J}(\theta) = \sum_{l_1 l_2 sk}(-1)^{s-l_1-l_2}\bar{Z}\left(l_1Jl_2J;sk\right)\bar{Z}(JJJJ;0k)P_k(\cos\theta) \times e^{i\left(\zeta_{l_1}+\zeta_{l_2'}-\zeta_{l_1'}-\zeta_{l_2}\right)}\sqrt{\Gamma_{s_1l_1}\Gamma_{s_1'l_1'}\Gamma_{s_2l_2}\Gamma_{s_2'l_2'}}. \quad (2.20)$$

To further simplify the equations for the (p,α_0) angular distributions, the partial widths are expressed in terms of mixing ratios. The convention used here is based on Nelson *et al.* (1985). The channel spin mixing ratio for the case of a spin $3/2^+$ target is defined as

$$\xi = \frac{\sum_l \Gamma_{s=2,l}}{\Gamma_p}, \quad (2.21)$$

where Γ_p is the total proton width of the resonance. The range of ξ is from 0 to 1. The orbital angular momentum mixing angle, ψ_s, is defined as

$$\tan\,\psi_s = \sqrt{\frac{\Gamma_{s,l+2}}{\Gamma_{sl}}}. \quad (2.22)$$

Since only the relative signs between the reduced widths can be measured, ψ_s is limited to $\pm 90°$. Only the two lowest l values are used in calculating the (p,α_0) angular distribution equations, since the higher l values can be neglected due to their low penetrability values.

Table 2.1 lists the Legendre coefficients for the (p,α_0) angular distribution for $J = 1$ to 4. In this table, a final reduction has been performed by dividing out the coefficient for P_0 leaving the angular distribution in the form

$$W_{\alpha J}(\theta) = a_0\left(1 + a_2P_2 + a_4P_4 + \ldots\right). \tag{2.23}$$

Since these equations are very lengthy to evaluate by hand, Vanhoy (1986) has written a program using the symbol manipulation language SMP, which greatly reduces the time needed to evaluate these coefficients. Table 2.1 was compiled with the help of this program.

It is convenient to consider reduced widths and reduced width amplitudes which remove the penetrability effects on the laboratory widths. The reduced width amplitude γ_{sl}, and the reduced width γ_{sl}^2, are related to the partial laboratory width by the relation $\gamma_{sl}^2 = \Gamma_{sl}/2P_l$, where P_l is the penetrability of the reaction product with orbital angular momentum l. The angular correlation formulas can then be expressed as a function of the reduced width mixing ratio and mixing angle. Table 2.2 lists the Legendre coefficients for the (p,α_0) angular distribution equations for the $J^\pi = 1^-$ and 2^+ cases, as well as the reduced width mixing angle and ratio definitions. In this table, P_l represents the proton penetrability.

C. Discussion of the Angular Distribution Equations

A closer examination of the (p,α_0) angular distribution equations provides insight about the information that can be extracted from an angular distribution measurement. Since ψ_2 appears in each set of equations in the term $\sin(2\psi_2)$, sign information about ψ_2 can be obtained. This is important because ψ_2 is the only variable related to the reduced width amplitudes; the sign of ψ_2 reveals the relative sign between the $s = 2$ reduced

Table 2.1

Legendre Coefficients for (p, α_0) Angular Distributions from a $3/2^+$ Target

$J^\pi = 1^-$

$$a_0 = 1$$

$$a_2 = -(1-\xi) + \frac{1}{5}\xi\cos^2\psi_2 + \frac{4}{5}\xi\sin^2\psi_2 - \frac{3}{5}\sqrt{6}\,\xi\sin(2\psi_2)\cos(\zeta_1 - \zeta_3)$$

$J^\pi = 2^+$

$$a_0 = 1$$

$$a_2 = \frac{5}{7}(1-\xi) - \frac{15}{49}\xi\sin^2\psi_2 - \sqrt{\frac{10}{7}}\sin(2\psi_2)\cos(\zeta_0 - \zeta_2)$$

$$a_4 = -\frac{12}{7}(1-\xi) + \frac{36}{49}\xi\sin^2\psi_2$$

$J^\pi = 3^-$

$$a_0 = 1$$

$$a_2 = (1-\xi) + \frac{4}{5}\xi\cos^2\psi_2 + \frac{19}{45}\xi\sin^2\psi_2 - \frac{4}{5}\sqrt{\frac{3}{7}}\,\xi\sin(2\psi_2)\cos(\zeta_1 - \zeta_3)$$

$$a_4 = \frac{3}{11}(1-\xi) + \frac{9}{11}\xi\sin^2\psi_2 - 2\sqrt{\frac{3}{7}}\,\xi\sin(2\psi_2)\cos(\zeta_1 - \zeta_3)$$

$$a_6 = \frac{25}{11}(1-\xi) + \frac{125}{99}\xi\sin^2\psi_2$$

$J^\pi = 4^+$

$$a_0 = 1$$

$$a_2 = \frac{85}{77}(1-\xi) + \frac{50}{49}\xi\cos^2\psi_2 + \frac{4415}{5929}\xi\sin^2\psi_2 - \frac{30}{49}\sqrt{\frac{5}{22}}\,\xi\sin(2\psi_2)\cos(\zeta_2 - \zeta_4)$$

$$a_4 = \frac{729}{1001}(1-\xi) + \frac{27}{49}\xi\cos^2\psi_2 - \frac{16767}{77077}\xi\sin^2\psi_2 - \frac{486}{539}\sqrt{\frac{10}{11}}\,\xi\sin(2\psi_2)\cos(\zeta_2 - \zeta_4)$$

$$a_6 = -\frac{1}{11}(1-\xi) - \frac{113}{121}\xi\sin^2\psi_2 - \frac{30}{11}\sqrt{\frac{5}{22}}\,\xi\sin(2\psi_2)\cos(\zeta_2 - \zeta_4)$$

$$a_8 = -\frac{392}{143}(1-\xi) + \frac{2744}{1573}\xi\sin^2\psi_2$$

Table 2.2

Legendre Coefficients for (p,α_0) Angular Distributions
for a $3/2^+$ Target as a Function of
the Reduced Width Mixing Ratio and Mixing Angle

$$J^\pi = 1^-$$

$$a_0 = 1$$

$$a_2 = \frac{\frac{1}{5}(1-\varepsilon^2) - \left[\cos^2\varphi - \frac{4}{5}\sin^2\varphi\right]P\varepsilon^2}{1-\varepsilon^2-P\varepsilon^2} - \frac{\frac{6}{5}\sqrt{6P}\cos(\zeta_0-\zeta_2)\varepsilon\sqrt{(1-\varepsilon^2)}\sin\varphi}{1-\varepsilon^2-P\varepsilon^2}$$

$$\tan\varphi = \frac{\gamma_{21}}{\gamma_{11}} \qquad \varepsilon^2 = \frac{\gamma_{21}^2+\gamma_{23}^2}{\gamma_{11}^2+\gamma_{21}^2+\gamma_{23}^2} \qquad P = \frac{P_3}{P_1}$$

$$J^\pi = 2^+$$

$$a_0 = 1$$

$$a_2 = \frac{\left[\frac{5}{7}\cos^2\varphi - \frac{15}{49}\sin^2\varphi\right]P\varepsilon^2}{1-\varepsilon^2-P\varepsilon^2} - \frac{\frac{2}{7}\sqrt{70P}\cos(\zeta_0-\zeta_2)\varepsilon\sqrt{(1-\varepsilon^2)}\sin\varphi}{1-\varepsilon^2-P\varepsilon^2}$$

$$a_4 = \frac{\left[-\frac{12}{7}\cos^2\varphi - \frac{36}{49}\sin^2\varphi\right]P\varepsilon^2}{1-\varepsilon^2-P\varepsilon^2}$$

$$\tan\varphi = \frac{\gamma_{22}}{\gamma_{12}} \qquad \varepsilon^2 = \frac{\gamma_{12}^2+\gamma_{22}^2}{\gamma_{20}^2+\gamma_{12}^2+\gamma_{22}^2} \qquad P = \frac{P_2}{P_0}$$

width amplitudes. These are the only pair of amplitudes for which the relative sign can be obtained from this experiment. Hidden in these equations is the fact that although all of these equations are written in terms of two variables, the combinations of s and l values allow for three partial widths for each J^{π}. The required third variable is the total proton width Γ_p, which is determined from the elastic scattering data.

The (p,α_0) angular distribution for the 2^+ resonances contains contributions from both P_2 and P_4. Thus there are two equations, one for each of the two Legendre coefficients, and a complete solution for the mixing parameters is expected from the alpha angular distribution measurement.

Assuming time reversal invariance requires that the reduced amplitudes must be real. Shriner (1983a) has shown that for $J^{\pi} = 2^+$ this requirement limits the possible values of a_2 and a_4 for the (p,α_0) angular distributions to the region of the a_2a_4 plane enclosed by the heavy line in Figure 2.2. The equations of the two straight lines are

$$\begin{aligned} 12a_2 + \left[5 + 7\cos(\zeta_0 - \zeta_2)\right] a_4 + 12\cos(\zeta_0 - \zeta_2) = 0 \\ 12a_2 + \left[5 - 7\cos(\zeta_0 - \zeta_2)\right] a_4 - 12\cos(\zeta_0 - \zeta_2) = 0 \end{aligned} \tag{2.24}$$

and the equation of the ellipse connecting the two lines at the top is given by:

$$\begin{aligned} 1296a_2^2 + \left[225 + 13720\cos^2(\zeta_0 - \zeta_2)\right] a_4^2 \\ + 1080a_2a_4 - \left[10080\cos^2(\zeta_0 - \zeta_2)\right] a_4 = 0\,. \end{aligned} \tag{2.25}$$

The solid and dashed lines in the interior are contour lines of ε^2. As the value of ε^2 increases the ends of the curves trace out the ellipse of Eqn. 2.25. Above $\varepsilon^2 = 0.9$, the curve endpoints continue to circle around the top of the ellipse, crossing over the curves of lower ε^2. This demonstrates that for values of a_2 and a_4 which lie inside the ellipse of Eqn. 2.25, only one solution to the (p,α_0) angular distribution equations exists, while if the value is located in the lower region where the curves cross each other, two different values of φ and ε^2 can be found which satisfy the equations. Only one of these

Figure 2.2 Physically allowed region of a_2 and a_4 for the 2^+ ^{39}K(p,α_0) angular distribution at E_p = 3.0 MeV. The solid and dashed lines in the interior are curves of constant ε^2. The value of ε^2 is indicated for several of the lines. As the value of ε^2 increases, the endpoints of the curves trace out the ellipse in the upper region of the figure. For values of $\varepsilon^2 \geq 0.9$, the endpoints of the curves lie on the upper half of the ellipse. Thus, if a value of a_2 and a_4 lies inside the ellipse, only one solution to the Legendre coefficient equations exists, with $\varepsilon^2 \geq 0.9$. If the value of a_2 and a_4 lies in the lower region, then two solutions exist for the Legendre coefficient equations. For at least one of the solutions, ε^2 is greater than 0.9.

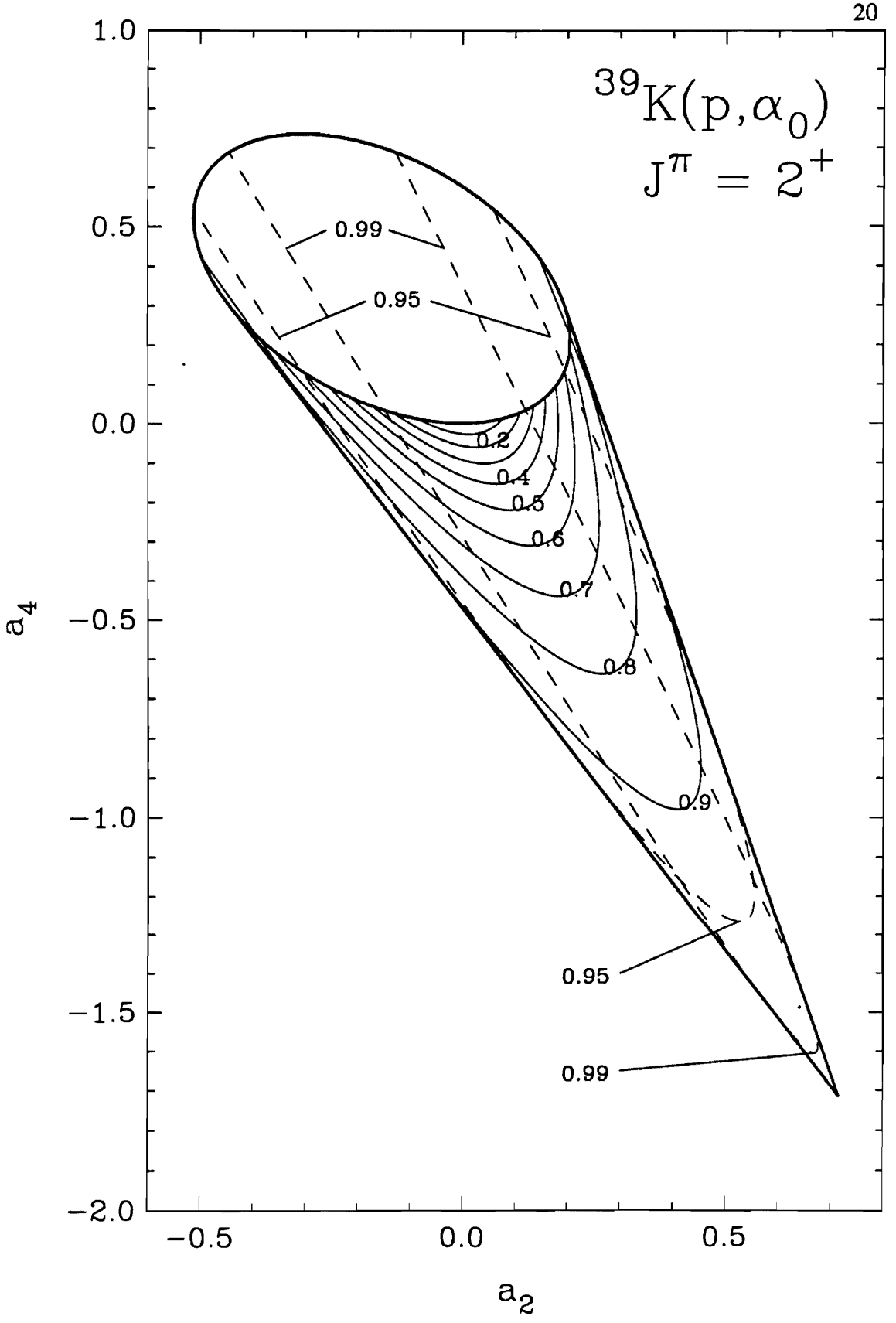
$^{39}K(p,\alpha_0)$
$J^\pi = 2^+$
0.99
0.95
0.2
0.4
0.5
0.6
0.7
0.8
0.9
0.95
0.99
1.0
0.5
0.0
−0.5
−1.0
−1.5
−2.0
−0.5
0.0
0.5
a_4
a_2

solutions gives the correct values for the partial widths. The elastic scattering data must be used to resolve the discrepancy between the two solutions obtained from the angular distribution measurement.

For the $J^\pi = 1^-$ resonances, the (p,α_0) angular distribution contains only a P_2 term, and thus is linear with respect to $\cos^2\theta$, where θ is the detector angle. Therefore, only one Legendre coefficient, a_2, can be determined from the experiment, and the maximum information that can be obtained from the angular distribution is a relationship between the mixing ratio and the mixing angle. Additional information must come from the resonance shapes of the elastic scattering data. Since MULTI6, a computer code based on R-matrix theory which calculates cross sections, requires the laboratory widths Γ_{sl}, the properties of the $J^\pi = 1^-$ equation from Table 2.1 will be examined along with the mixing ratio ξ and the mixing angle ψ_2. The ranges of these two variables limit the lower value of a_2 to -1.0. The upper limit of a_2 is related to the term $\cos(\zeta_0 - \zeta_2)$ which depends on the energy of the incoming proton. For the energy range of this experiment, the upper bound of a_2 varies from 0.9 for $E_p = 2.2$ MeV to 1.1 for $E_p = 4.0$ MeV.

A plot of ψ_2 versus ξ for selected values of a_2 at two different values of E_p is given in Figure 2.3. Since ξ is not single valued for this function, ψ_2 is used as the variable which defines the values of the partial widths of a resonance with a certain a_2. As the value of a_2 increases, the values of ψ_2 become limited due to the restricted range of ξ. In addition, as a_2 become larger, ξ extends more in range, which causes a greater variance in the shapes of the elastic cross section over the range of ψ_2. This is demonstrated in Figure 2.4, which shows the shapes of the elastic cross section for certain values of ψ_2 at two values of a_2. For $a_2 = -0.8$, the shape of the cross section changes only slightly over the entire range of ψ_2, while for $a_2 = -0.1$, the shape of the cross section changes drastically as ψ_2 is varied. Thus for higher values of a_2, it will be easier to determine the value of ψ_2 from the shape of the elastic yield curve.

Figure 2.3 A plot of the orbital angular momentum mixing angle ψ_2 versus the channel spin mixing ratio ξ for various values of a_2 for a 1^- resonance. The solid lines are for $E_p = 2.2$ MeV and the dashed lines are for $E_p = 4.0$ MeV.

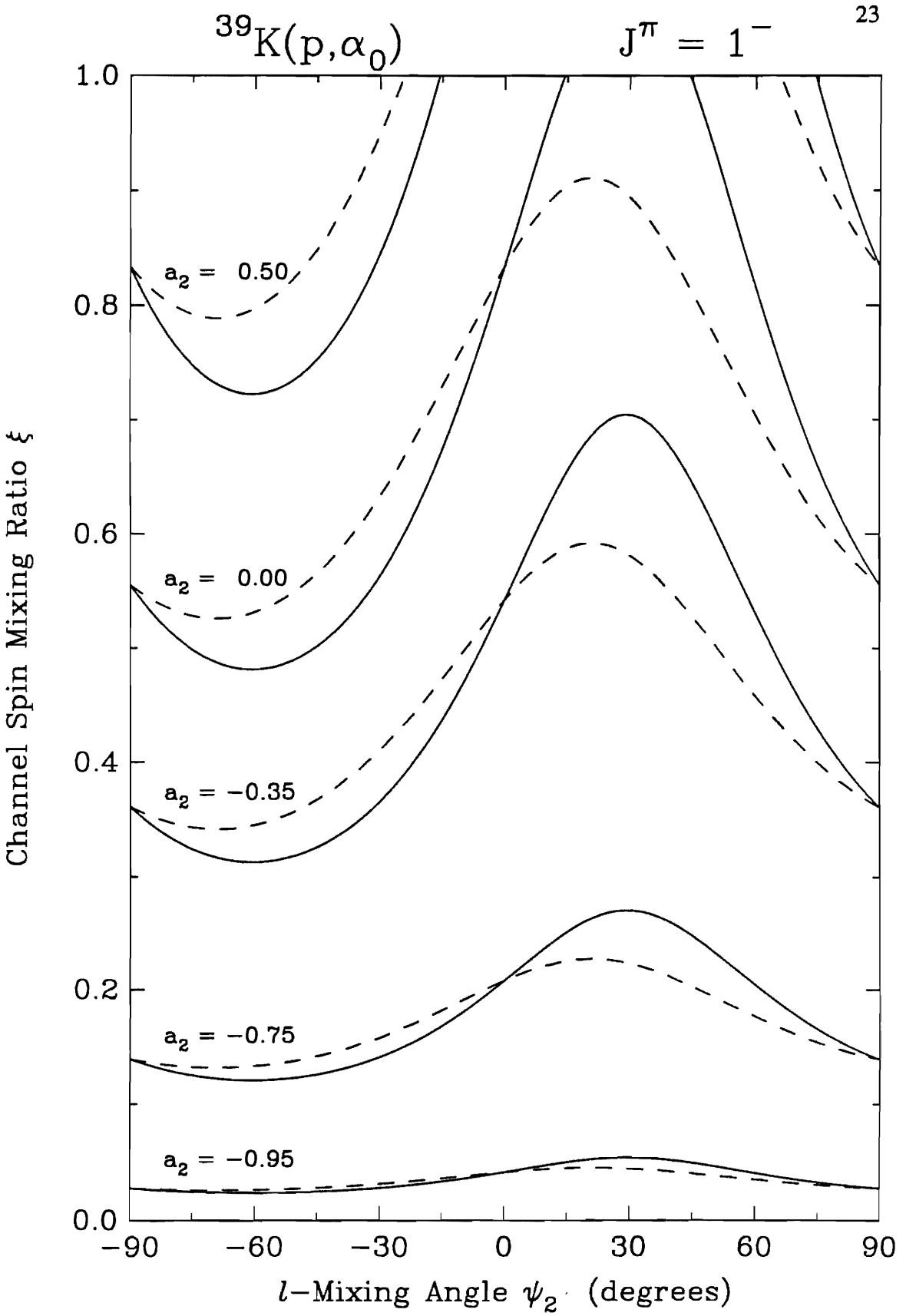
$^{39}K(p,\alpha_0)$
$J^\pi = 1^-$
Channel Spin Mixing Ratio ξ
$a_2 = 0.50$
$a_2 = 0.00$
$a_2 = -0.35$
$a_2 = -0.75$
$a_2 = -0.95$
1.0
0.8
0.6
0.4
0.2
0.0
−90
−60
−30
0
30
60
90
l−Mixing Angle ψ_2 (degrees)

Figure 2.4 Elastic scattering cross section shapes for a 1^- resonance at $E_p = 3.2$ MeV. Proton resonance shapes for alpha angular distributions with Legendre coefficients $a_2 = -0.8$ and $a_2 = -0.1$ are shown for ten different values of the orbital mixing angle ψ_2. The values of ψ_2, following the markers from left to right, are -90°, -75°, -60°, -45°, 0°, 20°, 30°, 45°, 70°, and 90°. Notice that in both figures, the curves for $\psi_2 = -90°$ and 90° (the first and last markers), $\psi_2 = -75°$ and 45° (the second and eighth markers), and $\psi_2 = -45°$ and 30° (the fourth and seventh markers) are identical.

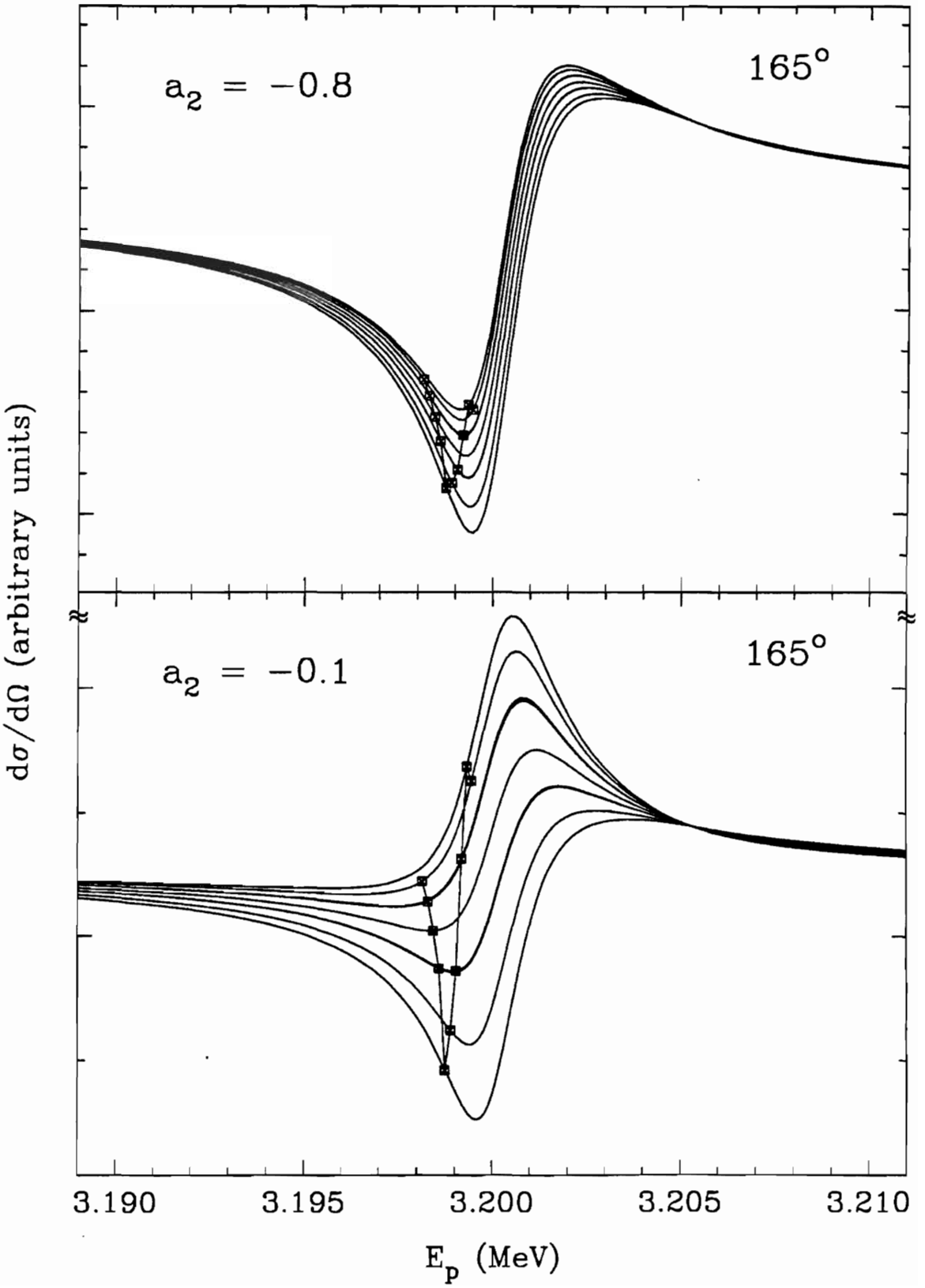
^{39}K(p,p)
$J^{\pi} = 1^{-}$
$a_2 = -0.8$
165°
$a_2 = -0.1$
165°
dσ/dΩ (arbitrary units)
3.190
3.195
3.200
3.205
3.210
E_p (MeV)

An examination of both plots of Figure 2.4 reveals a pattern between the value of ψ_2 and the cross section. In both plots, the first marker from the left corresponds to the cross section for $\psi_2 = -90°$. As ψ_2 increases, the curves move down the figures until at $\psi_2 = 0°$, the corresponding cross section curve is the lowest curve on the plots. Then, as ψ_2 increases above 0°, the curves move up the pictures until they peak at $\psi_2 = 75°$. After that, the curves move back down as ψ_2 increases still more, until at $\psi_2 = 90°$, the cross section is identical to the curve for $\psi_2 = -90°$. Thus, except for the two extremes of ψ_2 at 0° and 75°, a particular cross section shape can be produced from two different values of ψ_2. A comparison of the partial widths of the identical cross sections reveals that the magnitudes of Γ_{23} are equal for the two values of ψ_2. This property occurs for all values of a_2, and thus is independent of the values of the other widths. Since the cross sections are not unique for a set of widths, one will not be able to pinpoint the values of the reduced widths for the 1^- resonances from this experiment, but instead, should find two sets of widths which satisfy both the angular correlation equations and the resonance shape of the elastic scattering data.

D. Reaction Cross Sections

Although angular correlation methods are a powerful tool in nuclear spectroscopy, the measured angular distributions do not provide sufficient information to determine all of the spectroscopic information for a resonance. In some cases, however, enough additional information can be extracted from the excitation functions to determine the reduced widths of a resonance. As shown in the previous section, the different combinations of the partial widths of a resonance cause different shapes in the reaction cross section. These curves were calculated using the *R*-matrix theory for low energy nuclear reactions, which was first developed by Wigner and Eisenbud (1947). A detailed treatise

on R-matrix theory is given by Lane and Thomas (1958), and another discussion of the theory can be found in Vogt (1962). Only a very brief outline, based on Nelson (1983) will be presented here.

The major assumption of R-matrix theory is that the nuclear potential has a short, finite range, beyond which the nuclear potential has no effect. This divides the radial space of the projectile-target system into two regions, with $r = a_c$ defined as the limit of the nuclear potential. For the region $r > a_c$, the Schrödinger equation is solved with the Coulomb potential as the only potential affecting the incoming projectile. The solutions for this problem are the regular and irregular Coulomb functions, usually combined to represent incoming and outgoing waves. In the interior region $r < a_c$, the potential is complicated by the addition of the nuclear potential. The difficulty now arises because there is no analytical form for the nuclear potential, making it impossible to derive explicit equations for the interior wavefunctions. The problem now becomes how to calculate a cross section if the form of the scattering potential is unknown.

To circumvent this complication, the R-matrix is introduced. Assume that there exists a set of orthonormal wavefunctions, X_λ, with eigenvalues E_λ, which are solutions to the unknown Hamiltonian of the interior region, such that $HX_\lambda = E_\lambda X_\lambda$. The total wavefunction Ψ can be expressed as a linear combination of the X_λ. The one place at which the value of these wavefunctions is known is at the nuclear surface, where Ψ must combine smoothly with the wavefunctions of the outer region, as well as satisfy the appropriate boundary conditions. The R-matrix is invented to relate the value of the total wavefunction Ψ on the surface to its boundary conditions and its derivative (demonstrating continuity) at the surface,

$$\Psi_c(r_c) = \mathbf{R}_{cc'}\left[a_c\frac{d\Psi_c(r_c)}{dr} - B_c\Psi_c(r_c)\right]_{r_c = a_c}, \tag{2.26}$$

where B_c, a constant, is the boundary condition and

$$\mathbf{R}_{cc'} = \sum_{\lambda} \frac{\gamma_{\lambda c}\gamma_{\lambda c'}}{(E_{\lambda} - E)}, \tag{2.27}$$

is the R-matrix. The subscript c refers to the different channels, and the terms γ_{sl} are the reduced width amplitudes, which are related to X_{λ} by:

$$\gamma_{\lambda c} = \sqrt{\frac{\hbar^2}{2M_c a_c}} \int_{a_c} \chi_c^* \Psi_{\lambda} dS \,, \tag{2.28}$$

where the integral is over the nuclear surface $r = a_c$. Here M_c is the reduced mass of the projectile-target pair and χ_c is the channel wave function of the external region. The advantage to this method is that the reduced widths, which are related to the partial laboratory widths, contain all the information specific to the nuclear potential.

After the R-matrix has been formulated, Lane and Thomas proceed to calculate the differential cross section from the reduced widths. Sellin (1969) incorporated these cross section equations into the computer code MULTI. This program can calculate the differential cross section of a nucleus for up to 300 levels with 12 different J^{π} values and for 5 groups of decay channels. To fit a resonance with this program, an input file containing information specific to a particular nucleus, such as atomic number, weight, and reaction channels, is created. Next, the energy, J^{π}, and partial widths of a resonance are entered. The program then computes the cross section for specified detector angles, which are then compared with the excitation function data. This process can be very time consuming as the number of resonances increases and as ambiguities appear for some of the resonances. Angular correlation techniques used in conjunction with resonance shape analysis can simplify the fitting process by limiting the possible reduced width combinations for a resonance, and thus reducing some of the guesswork involved in the fitting process.

CHAPTER III

EXPERIMENTAL EQUIPMENT

Section A. Accelerator and Electrostatic Analyzer

These experiments were conducted on the Triangle Universities Nuclear Laboratory (TUNL) KN model Van de Graaff accelerator. Although originally designed for operation at a terminal voltage of 3 MV, in recent years an accelerator tube with stainless steel electrodes was installed and the accelerator modified to provide a 4 MV terminal voltage. Together with the high resolution feedback system, consisting of an electrostatic analyzer and associated electronics, this laboratory is capable of producing very stable proton beams over the energy range of 1 - 4 MeV with an overall resolution of 350 - 400 eV, as measured with thin foil targets. A system of this design was first described by Parks *et al.* (1958) and has been most recently described in detail by Westerfeldt *et al.* (1988). A schematic of the High Resolution Laboratory and control systems is shown in Figure 3.1.

Located in the terminal of the accelerator, the 100 MHz radio frequency ion source disassociates hydrogen gas to produce both protons and molecular HH^+ ions. Forced into the accelerating tube by a high voltage probe and focusing electrode, these two ion species are accelerated down the voltage gradient and into the analyzing magnet. Here the two beams are split, with the HH^+ beam deflected 17° towards the electrostatic analyzer and the proton beam bent 25° into a series of focusing and steering magnets before entering the scattering chamber.

Figure 3.1 Schematic of the TUNL KN Van de Graaff Laboratory and associated high resolution control systems.

High Resolution Laboratory and Control Systems

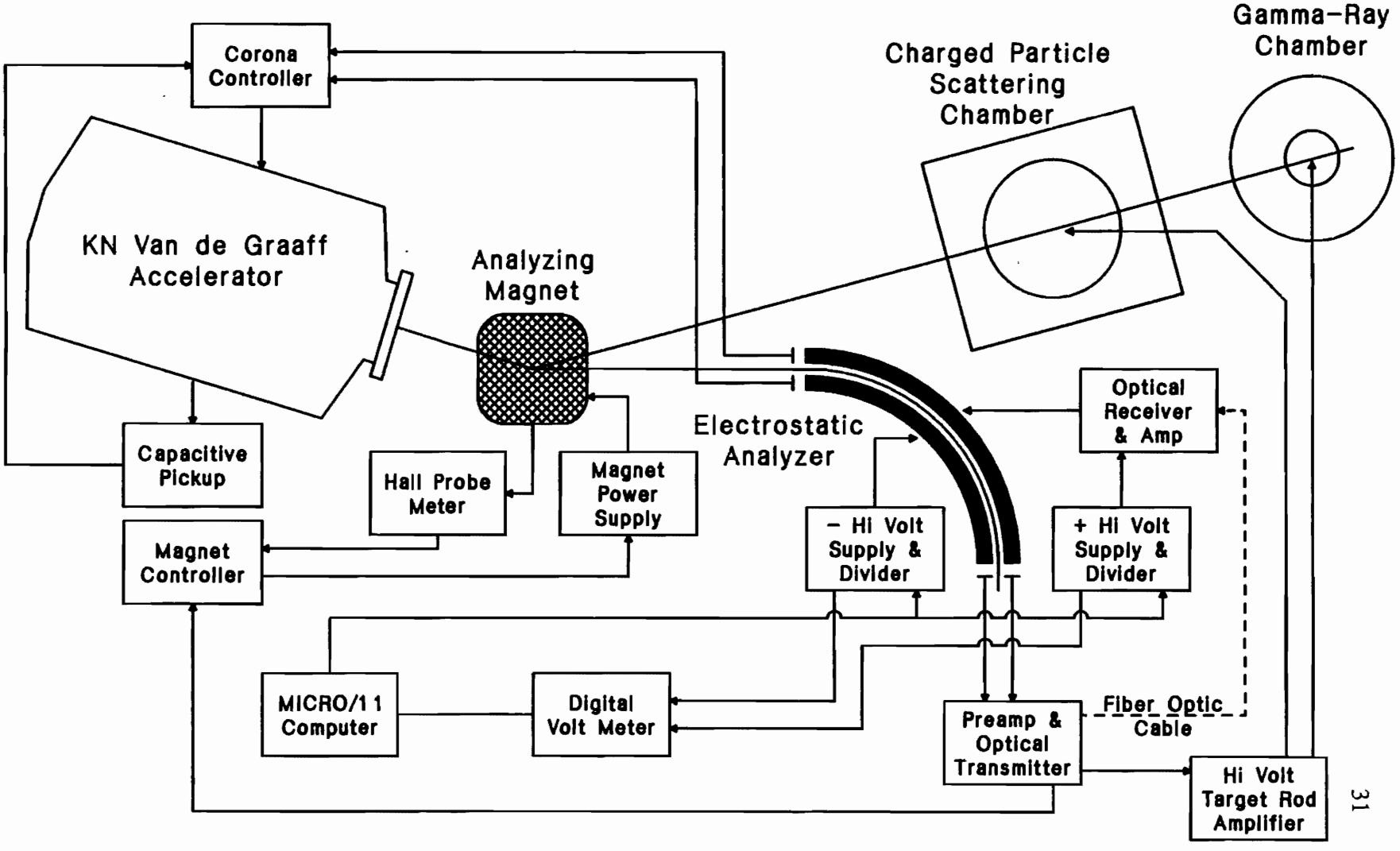

Soon after emerging from the bending magnet, the HH^+ beam passes through a pair of vertical slits, the first stage of the corona feedback circuit. Voltage fluctuations of the accelerator cause the beam to shift back and forth across these slits, resulting in a difference in the amount of beam current each slit intercepts. An energy correction signal is derived from this difference, which is sent back to the terminal through several sharp corona needles located in the pressure tank just above the voltage dome. Due to the high electric field at the needle points, ions are formed which then migrate onto the voltage dome, completing the circuit. Because of the slow drift time of the ions from the needles to the terminal, this system can only correct for voltage fluctuations below 10 Hz. While these experiments were in progress, another circuit was included to control the terminal voltage. In this circuit, terminal voltage fluctuations are measured using a capacitive pickup, an electrically isolated metal plate situated on the pressure tank above the terminal. This signal is then combined with the correction signal from the corona slits and sent to the corona needles. Using the combination of the two systems, the terminal voltage ripple has been reduced to approximately 1 kV.

After the corona slits, the HH^+ beam passes through a pair of beam limiting slits before entering the electrostatic analyzer. The analyzer consists of two steel plates curved in a 90° arc and separated by a 4.5 mm gap. These two metal plates are biased with equal and opposite high voltages provided by a pair of programmable Bertan power supplies. These power supplies are controlled by a digital voltmeter and a PDP-11 microprocessor. The beam travels through the analyzer in a circular arc until it emerges from the analyzer and strikes another pair of slits. As the energy of the beam changes, its radius of curvature through the analyzer also changes, causing the beam to move back and forth across the exit slits. The analyzer was designed such that a 1 V fluctuation on the analyzer plates corresponds to a 111 eV change in beam energy. The signal from the

exit slits is a direct measurement of the beam energy fluctuations. This signal is amplified by 111 and then sent to the target. The beam energy fluctuations are thus corrected by varying the voltage of the target. This correction signal is also fed back to the outer analyzer plate to keep the beam inside the analyzer. Finally, the signal is sent through a low pass filter to the analyzing magnet controller. This enables the magnet to keep the beam centered in the analyzer as the voltage on the plates is changed during the course of the experiment.

Section B. Scattering Chamber and Detectors

A top view of the scattering chamber and detector placement is shown in Figure 3.2. Before entering the chamber, the beam is reduced to a spot roughly 2 mm^2 in size by a series of collimators. The beam then passes through the target, located in the center of the chamber, before it is collected by a Faraday cup placed at the end of the chamber. The target is mounted on a sliding rod, which holds up to four targets and a tuning ring; this arrangement makes target changes and beam tuning simple. Typical beam currents are 2-3 μA on the Faraday cup with 20 nA of beam on the tuning ring. To maintain a vacuum of 1 μTorr during experiments, the chamber is equipped with a diffusion pump, refrigerated baffle, and liquid nitrogen trap.

Six surface barrier silicon detectors were used to measure the protons and alpha particles. These detectors were placed at angles of 90°, 108°, 127°, 145°, 150°, and 165° with respect to the incoming beam. A collimation assembly was mounted in front of each detector to limit the number of counts from secondary scattering. The solid angle of each detector was set to 2.5 msr. The target was rotated 25° with respect to the beam, so that all the detectors could view the target surface.

Figure 3.2 Top view of the charged particle scattering chamber showing the detector placement.

Charged Particle Scattering Chamber

(Top View)

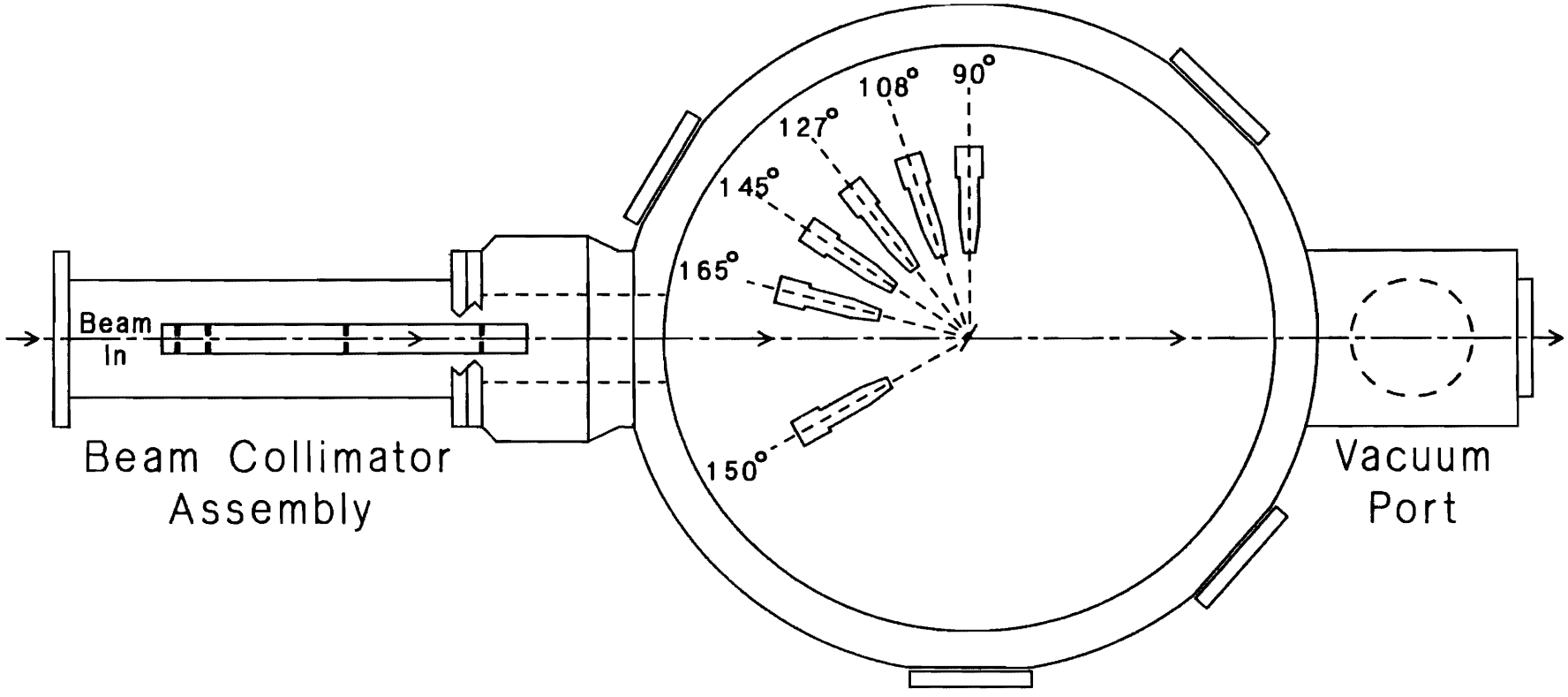

Section C. Data Acquisition

The data acquisition electronics consist of several NIM and CAMAC modules, a microprogrammable branch driver (MBD) and a VAX 11/750 computer. The software used to accumulate and process the data is the XSYS package developed at TUNL (King, 1981) and slightly modified to the specific uses of the High Resolution Laboratory. A discussion of the software used in the High Resolution Laboratory is contained in Appendix A. A block diagram of the electronics is shown in Figure 3.3.

Signals from each surface barrier detector are first sent through a preamp before being routed to the spectroscopy amplifier. Two types of output signals are then used from the amplifier. The unipolar signal is delayed 900 ns before it is sent to an eight input gated multiplexer. The output of the multiplexer is sent to the ADC, where it is digitized and then stored in one of two buffers contained in the CAMAC Borer buffer module. When one of the buffers is full, the module signals the MBD to empty that buffer. Meanwhile, incoming signals are stored in the other buffer, allowing continuous data processing. To reduce the number of wires used between the laboratory and the computer room, the routing signal from the multiplexer is encoded into a 3-bit word. In the computer room, it is then decoded and also sent to the buffer.

The other output from the linear amplifier, the bipolar signal, is used to reject the signals caused by protons scattering from the carbon backings of the target. If left in the spectra, these carbon signals will cause pileup peaks and broaden the peaks of interest in the spectra, as well as increase the dead time of the data acquisition system. The bipolar signal from the spectroscopy amplifier is routed in two directions, with one branch, after a 900 ns delay, sent to the input of the gated SCA, which is then connected to the gate of the multiplexer. The other bipolar signal is routed to the TSCA, which has a window set on the carbon signals, and whose output is connected to the gate of the SCA. When the

Figure 3.3 Block diagram of the data acquisition electronics.

Data Acquisition Electronics Setup

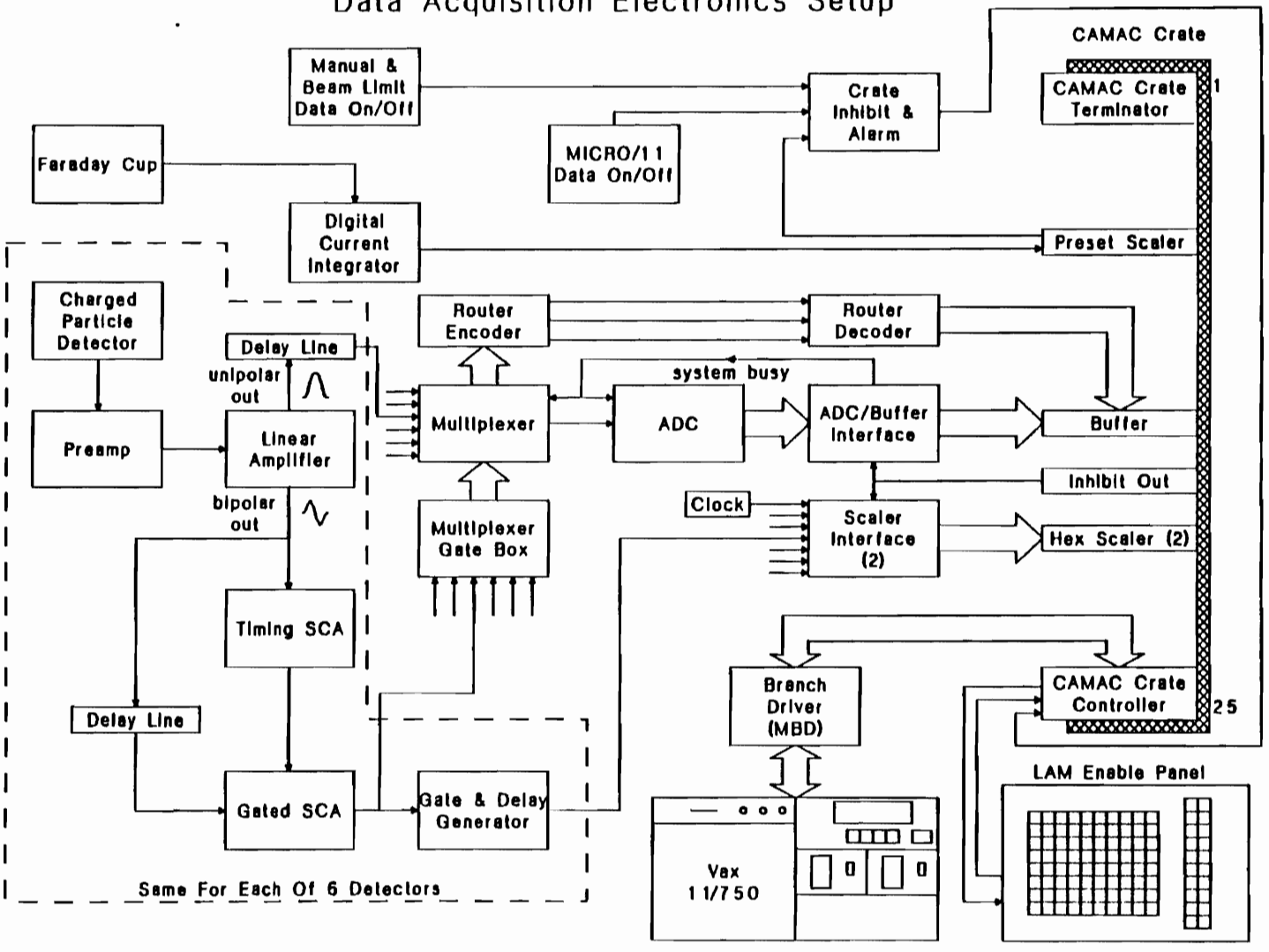

TSCA receives a pulse within the window, it sends a signal to the SCA which rejects the signal coming from the amplifier. The output from the SCA is also sent to a Gate and Delay module, which produces a short logic pulse. These signals are counted by a CAMAC scaler. By comparing the counts in the spectrum with the counts of the scaler, the dead time of the data acquisition system can be computed.

A current integrator is used to determine the amount of beam charge going through the target by digitizing the current hitting the Faraday cup beyond the scattering chamber. The output of the integrator is connected to a preset scaler, which, when the number of counts reaches the preset value, inhibits the data acquisition and signals the VAX that the data run is complete. The output of the current integrator is also connected to a meter with an adjustable window. To insure that data is taken with a steady beam, the data acquisition is halted if the beam current is outside the limits of the window. The data collection can also be inhibited by the microprocessor controlling the voltage on the electrostatic analyzer plates. If the voltage difference on the analyzer plates is greater than the amount needed to cause a 10 eV shift in the beam energy, the microprocessor inhibits the CAMAC crate, thus stopping the data collection. This procedure helps to ensure that the proper corrections for beam energy fluctuations have been made.

The XSYS data acquisition software package was used to control the CAMAC crate and the MBD, in addition to providing online data analysis. This software was developed at TUNL (King, 1981); an overview is given by Roberson and Gould (1985). When the data run is completed, several functions are performed to process the data just received and to prepare the equipment for the beginning of the next data run. First, the analyzer plate voltage is changed for the next beam energy while the spectra are written to a tape for offline analysis. Next, several excitation functions are computed by summing the areas beneath the appropriate peaks. Finally, all the spectra and scalers are

cleared and the data acquisition is resumed. Recently the time required to perform these tasks has been reduced through the use of a hibernating subprocess. At the beginning of the experiment, the subprocess is started, which, after some initialization, goes into a hibernate state. When the preset scaler is reached, the subprocess is awakened and performs the necessary procedures before returning to a hibernate state. This reduces the time between data runs from eleven to three seconds, saving over eleven hours on a typical seven day experiment of 5000 data runs.

Section D. Targets

Targets for this experiment were prepared at TUNL using a high vacuum high current evaporator system. A discussion on target preparation for high resolution charged particle spectroscopy has been given by Brooks (1988). Commercially available 5 $\mu g/cm^2$ carbon foils were separated from glass slides onto stainless steel target rings. These foils were then placed 7" from the bottom of the evaporator and covered with glass slides to prevent material from depositing on the back side of the targets. The vacuum chamber was pumped down to 1 μTorr before evaporation was begun.

Approximately 1 $\mu g/cm^2$ of gold was evaporated on the carbon foils. The purpose of the gold was twofold. First, it increased the stability of the targets by isolating the potassium carbonate from the carbon backing and by improving the thermal conductivity of the target. Second, the gold was used to normalize the detectors for each resonance, since the scattering from Au was pure Coulomb scattering. Next, 2 - 3 $\mu g/cm^2$ of potassium carbonate was evaporated onto the foils. This compound was obtained from Oak Ridge National Laboratory, enriched to 99.97 % ^{39}K.

Despite the layer of gold, the targets still required conditioning. The targets were bombarded with 3 μA of beam until any noticeable target degradation disappeared. The

typical conditioning time was 30 minutes and, once conditioned, the targets lasted for 1 - 2 days before needing to be replaced. A typical spectrum with the major reaction peaks labeled is shown in Figure 3.4.

Figure 3.4 Charged particle spectrum from Au backed $^{39}K_2CO_3$ targets. This spectrum was taken at detector angle 165° on the (p,α_0) resonance at E_p = 3.5490 MeV. The $^{12}C(p,p)$ reaction peak has been gated out.

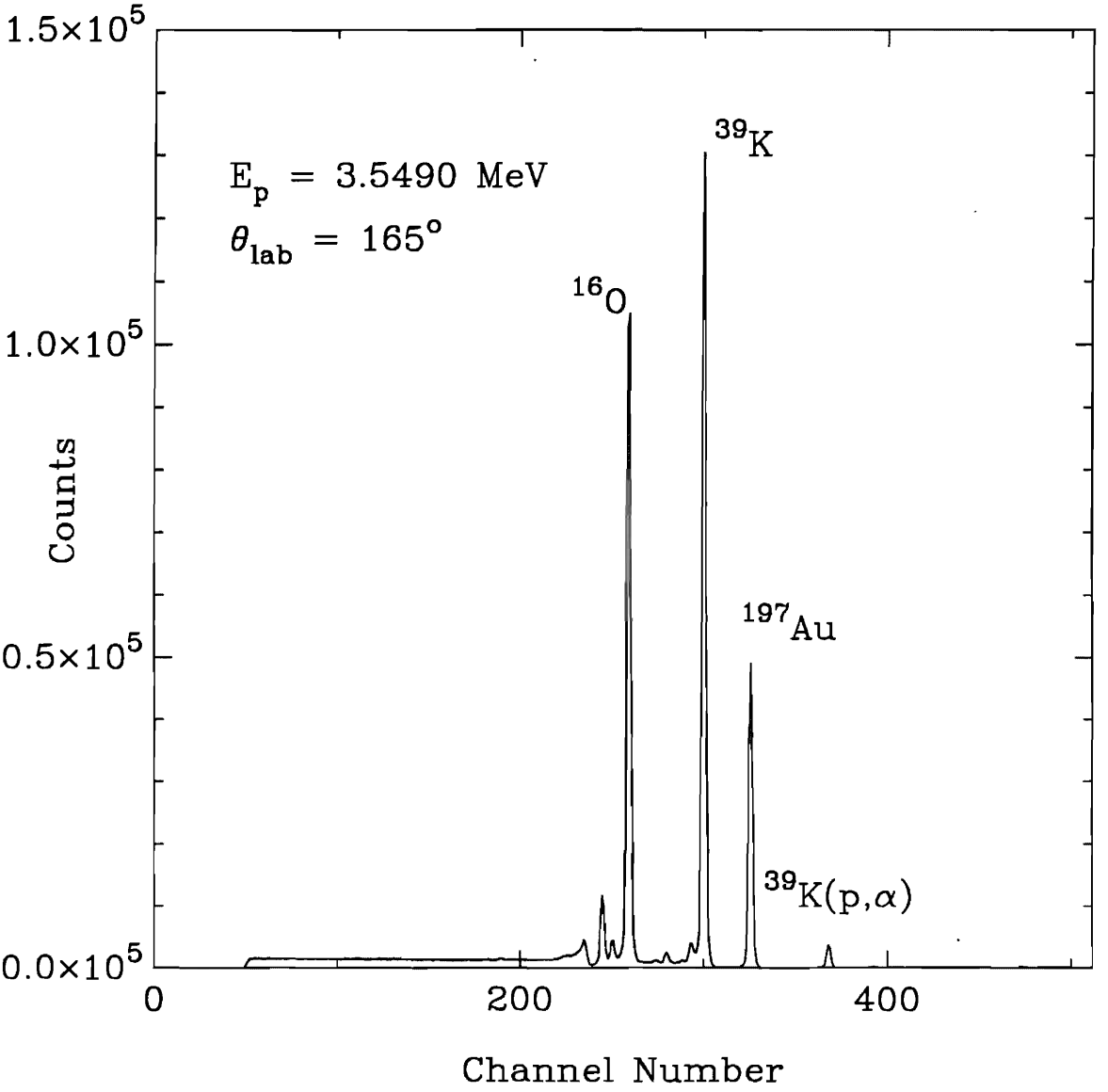
1.5×10^5
1.0×10^5
0.5×10^5
0.0×10^5
Counts
E_p = 3.5490 MeV
θ_lab = 165°
16O
39K
197Au
39K(p,α)
0
200
400
Channel Number

CHAPTER IV

EXPERIMENTAL PROCEDURE AND PRELIMINARY RESULTS

Section A. General Method

A complete high resolution study of the $^{39}K(p,p_0)$ and the $^{39}K(p,\alpha_0)$ reaction from E_p = 1.9 MeV to 4.0 MeV was recently completed by Warthen (1987). Figure 4.1 shows the cross section data for both reactions at a laboratory angle of 165°. The solid line represents the fit which was obtained with MULTI6, a multi-level, multi-channel *R*-matrix program based on the differential cross section formulas of Lane and Thomas (1958). In this study energies, spins, and parities were assigned to 248 proton resonances, of which 148 also had a measurable alpha width. Most of the resonances observed in the α_0 decay channel were assigned J^π values of either 1^- or 2^+. Since a large number of resonances is necessary in order to obtain statistically significant linear correlations, this experiment was restricted to an in-depth study of the 1^- and 2^+ resonances.

The experimental procedure began with the measurement of an excitation function for each resonance. Typically, each yield curve was started one to two keV below the beam energy at which the alpha yield was expected to rise. A charged particle spectrum was collected at each energy. Better than 2% counting statistics were obtained for the elastic reaction at each angle. This usually required from 150 μC to 300 μC of integrated beam current, depending on the thickness of the target. After the desired amount of charge was collected, a yield for each reaction was calculated by determining the number of counts in the appropriate peak, and then subtracting a linear background from

Figure 4.1 The $^{39}K(p,p_0)^{39}K$ and $^{39}K(p,\alpha_0)^{36}Ar$ differential cross sections at $\theta_{lab} = 165^{\circ}$ from $E_p = 2.00$ MeV to 4.02 MeV. The solid line is a fit to the data.

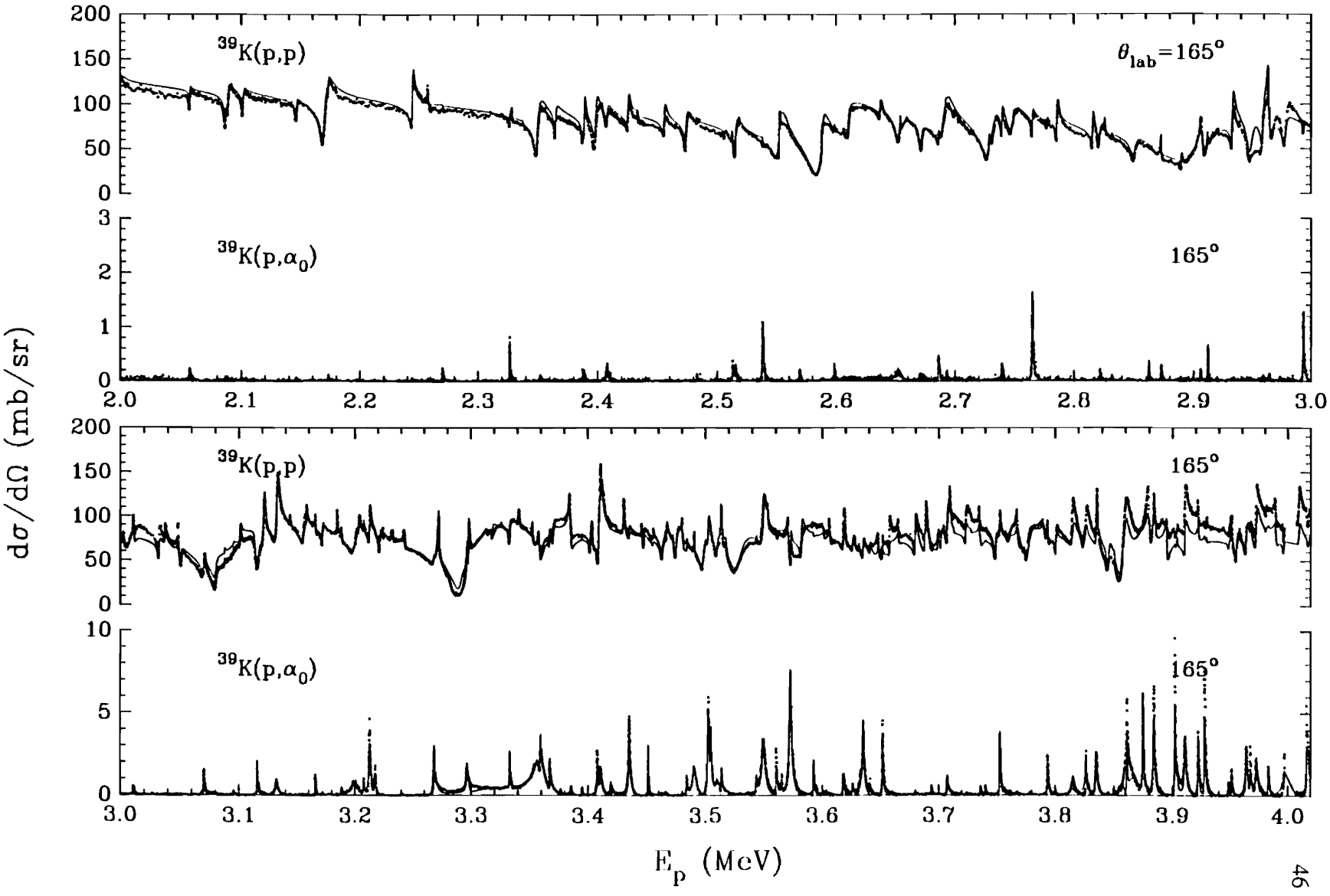
^{39}K(p,p)
θ_{lab}=165°
^{39}K(p,α_0)
165°
^{39}K(p,p)
165°
^{39}K(p,α_0)
165°
dσ/dΩ (mb/sr)
E_p (MeV)

the peak. This sum was then multiplied by the dead time factor to obtain the true number of counts. After the spectra and scalers were written to magnetic tape, the proton beam energy was incremented and the next set of spectra was collected. Most of the excitation functions were taken in steps of 100 eV on or near the resonance, except for a few resonances which had unusually large widths. The excitation curve was then ended 1 to 2 keV above the energy at which the alpha yield returned to background. In cases where two or more resonances in the α_0 channel were close together, one single yield curve was obtained which included all the resonances.

After the excitation function for the resonance was completed, the beam energy was set at the resonance energy to measure the (p,α_0) angular distribution. At this energy, the spectra were collected until enough counts were accumulated to obtain 1% counting statistics or until 10,000 μC of charge was collected at the Faraday cup. If insufficient alpha counts were collected after the first on-resonance measurement, then the resonance would be relocated by measuring a short yield curve before accumulating more data. This procedure was followed to insure that the accelerator energy had not drifted off resonance during the previous measurement. Data were then accumulated for another 10,000 μC of integrated beam current, or until the alpha counts reached 10,000. Only for a handful of resonances were the angular distributions collected for more than 20,000 μC of total beam charge. For a few resonances, another (p,α_0) resonance was close enough to affect the angular distribution of the resonance of interest. In these cases, data were accumulated a few hundred eV off the resonance energy, away from the second resonance.

The offline analysis began with the recreation of the excitation functions from the spectra stored on magnetic tape. These were calculated in the same manner as before, except that special attention was paid to the peak summation and to the background subtraction. Next, the angular distribution information was extracted from the spectra.

For the gold peaks and most of the alpha peaks, the same method used to compute the yield curve sums was used to obtain the reaction counts. But for some of the weaker resonances, the region of the spectrum around the alpha peak fluctuated significantly. In these instances, a Gaussian peak with a quadratic background was fit to the data. The Gaussian area was then multiplied by the dead time factor to obtain the true number of counts.

The proton-gold angular distribution was used to normalize the detectors. After transforming the detector angles and collimator solid angles to the center of mass reference frame, the proton-gold angular distribution was fit to $\mathbf{W}(\theta) = A/\sin^4(\theta/2)$, the form for Coulomb scattering. From this fit, normalization factors were computed for each angle, which were used to correct for any discrepancies in the detector efficiencies and solid angles. The normalization factors were consistent for each data run, and usually differed by no more than 3%.

After normalization, the (p,α_0) angular distributions were fit to a Legendre polynomial expansion. For the 1^- resonances, the distribution was fit to the form

$$\mathbf{W}_{\alpha 1^-}(\theta) = a_0\left(1 + a_2 P_2\right), \tag{4.1}$$

while the 2^+ resonances were fit up to the form

$$\mathbf{W}_{\alpha 2^+}(\theta) = a_0\left(1 + a_2 P_2 + a_4 P_4\right). \tag{4.2}$$

Examples of the data and fit for both a 1^- and a 2^+ resonance are given in Figure 4.2. From the coefficients in the expansion, the values of the mixing parameters φ and ε^2 were solved for directly in the case of the 2^+ resonances. Only a relationship between φ and ε^2 was found for the 1^- resonances. Further analysis using the elastic scattering data was necessary to obtain the actual proton partial widths for each case. The next sections in this chapter will describe the procedures used in more detail.

After the proton partial widths had been obtained from the combination of the (p,α_0) angular distribution and the elastic cross section data, the alpha widths were

Figure 4.2 Typical alpha angular distribution and fit for a 1^- and a 2^+ resonance in ^{40}Ca.

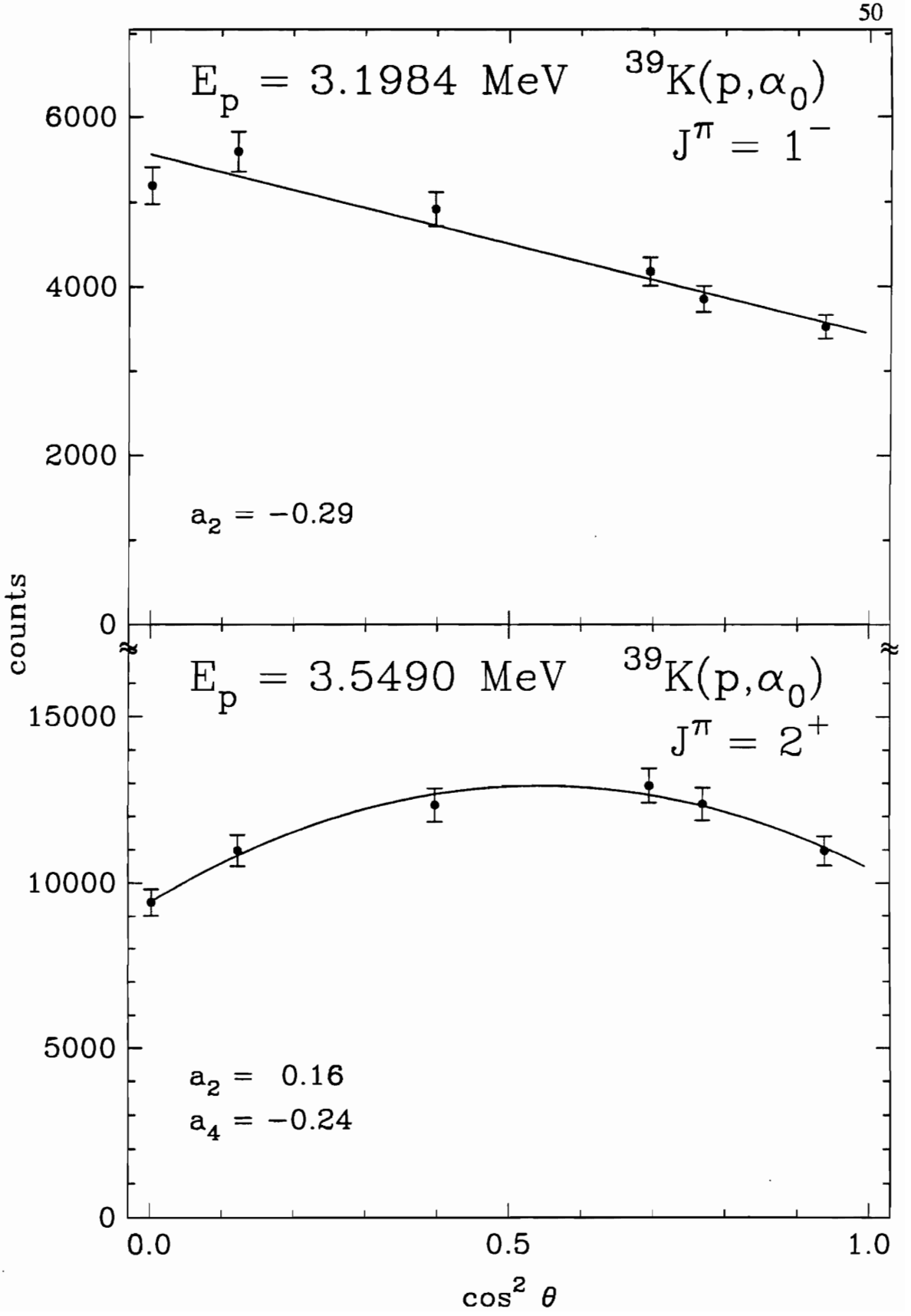
E_p = 3.1984 MeV
$^{39}K(p,\alpha_0)$
$J^\pi = 1^-$
$a_2 = -0.29$
E_p = 3.5490 MeV
$^{39}K(p,\alpha_0)$
$J^\pi = 2^+$
$a_2 = 0.16$
$a_4 = -0.24$
counts
6000
4000
2000
0
15000
10000
5000
0
0.0
0.5
1.0
$\cos^2 \theta$

determined with MULTI6, utilizing a χ^2 minimum search routine based on a method outlined in Bevington (1969). With an initial guess for the alpha width, a value of χ^2 is calculated for the excitation functions of the six detector angles and the cross sections calculated by MULTI6. Next, the alpha width is increased by 5% and the χ^2 is recalculated. If the new χ^2 value is less than the first, then the alpha width is increased again and another χ^2 is calculated. Otherwise, the direction of the search is reversed, and the next χ^2 is calculated from a fit generated with an alpha width smaller than the initial value. The search then continues in the direction of decreasing χ^2 until a value for the alpha width is found which causes χ^2 to increase. The last three estimates for the alpha width and the χ^2 values describe a parabola, with the middle value of χ^2 less than the first and third values. The minimum of this curve is computed to find the final value of the alpha width, for which a final χ^2 value is then calculated. In addition, the step size of the search is changed, based on the number of alpha width increments used to find the minimum χ^2 value. This entire process is then repeated until the final χ^2 values differ by less than 0.1%. The number of iterations needed depends on the initial guess, but typically the χ^2 values converge in 2-4 iterations.

Section B. Results for 2^+ Resonances

Of the fifty resonances previously assigned J^π values of 2^+, (p,α_0) angular distribution data were obtained for only 42 resonances. For the other eight resonances, the resonances in the α_0 channel were either too small to be observed, or interfered with another nearby resonance. Of the 42 (p,α_0) angular distributions measured, 11 yielded a_2 and a_4 values outside the physically allowed region and 3 had poor elastic scattering fits based on the (p,α_0) information; this left 28 resonances with satisfactory results. Later,

this number was increased by 2 to 30 by studying some of the resonances previously assigned different J^{π} values. All of the (p,α_0) angular distributions for the unsatisfactory resonances were measured at least twice during separate experiments. Later, these resonances were reanalyzed to determine the cause of their poor results. It was concluded that 5 of them were not 2^+ resonances, but actually had other J^{π} values. For the remaining 9 resonances, the alpha peaks were either too small or so close to another (p,α_0) resonance that interference between the resonances caused inaccurate measurements of the angular distribution. The few resonances whose a_2 and a_4 values lie just outside the physically allowed region were also examined, but the elastic scattering data did not agree with the (p,α_0) angular distribution results. For some of the resonances, it was necessary to adjust the total elastic width in order to obtain the best fit. A plot of the a_2 and a_4 values for the 2^+ resonances is shown in Figure 4.3. Table 4.1 lists the values of a_2 and a_4 for each resonance.

As explained earlier, only one solution for the proton partial widths is obtained if the values of a_2 and a_4 lie inside the ellipse of Figure 4.3. However, if the values of a_2 and a_4 lie in the lower cone-shaped region, two solutions exist for the angular correlation equations, and the selection between these two solutions must be achieved using the elastic scattering data. In these cases, the *R*-matrix code MULTI6 was used to generate an elastic scattering cross section from the proton partial widths for each solution, and a comparison between the cross sections and the yield curves was sufficient to select the proper solution. Figure 4.4 shows the excitation function along with the two different cross sections computed from the (p,α_0) distribution results for the resonance at E_p = 3.5490 MeV. From this plot it is obvious that the correct solution is shown in the lower figure.

The three resonances at E_p = 2.7859 MeV, E_p = 3.4105 MeV and E_p = 3.5021 MeV proved to be special cases. The experimental values of the Legendre coefficients

Figure 4.3 Experimental Legendre coefficients for the 2^+ resonances in ^{40}Ca. The solid lines border the physically allowed regions. Only one solution to the angular correlation equations exists for each point in the region enclosed by the ellipse, while two solutions exist for each point in the lower cone-shaped region.

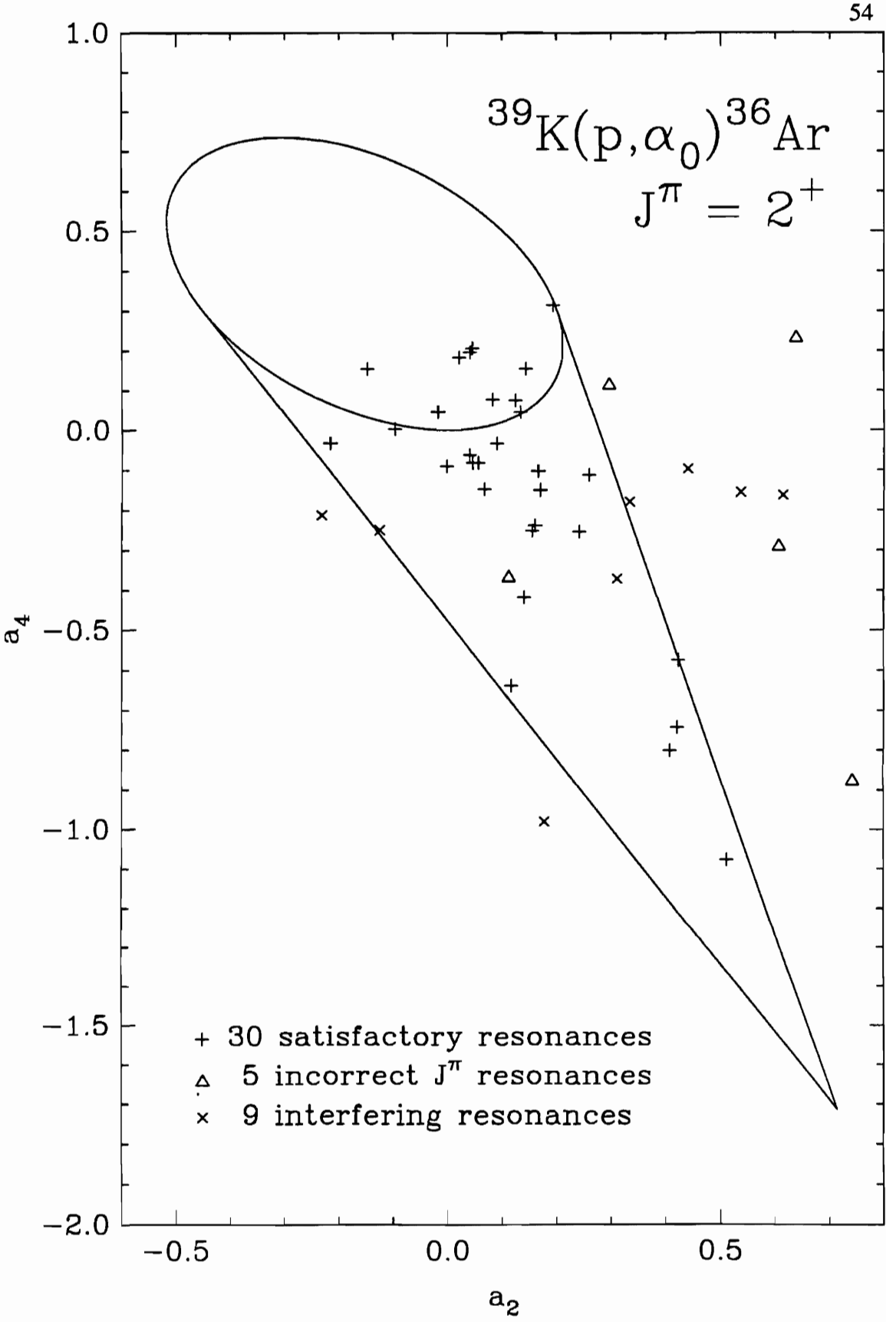
$^{39}K(p,\alpha_0)^{36}Ar$
$J^\pi = 2^+$
+ 30 satisfactory resonances
△ 5 incorrect J^π resonances
× 9 interfering resonances
a_4
a_2
1.0
0.5
0.0
−0.5
−1.0
−1.5
−2.0
−0.5
0.0
0.5

Table 4.1

Legendre Coefficients for (p,α_0) Angular Distributions for 2^+ Resonances in ^{40}Ca

E_p (MeV)	a_2	a_4	remarks
2.3891	0.04 ± 0.03	-0.06 ± 0.05	
2.5130	0.02 ± 0.04	0.18 ± 0.05	
2.5982	-0.22 ± 0.04	-0.03 ± 0.05	
2.6859	0.00 ± 0.03	-0.09 ± 0.05	
2.7859[a]	-0.15 ± 0.03	0.15 ± 0.05	
2.8623	0.42 ± 0.03	-0.57 ± 0.04	
3.0114	0.41 ± 0.03	-0.80 ± 0.04	
3.0705	0.06 ± 0.03	-0.08 ± 0.05	
3.1157	0.04 ± 0.04	0.20 ± 0.05	
3.1212	0.44 ± 0.04	-0.10 ± 0.05	unphysical result / interference
3.1322	0.09 ± 0.03	-0.03 ± 0.05	
3.1883	0.51 ± 0.02	-1.08 ± 0.03	
3.2125	0.26 ± 0.03	-0.11 ± 0.05	
3.2173	0.30 ± 0.04	0.11 ± 0.05	unphysical result / wrong J^π
3.2681	0.42 ± 0.03	-0.74 ± 0.04	
3.2726	0.31 ± 0.03	-0.37 ± 0.05	poor elastic result / interference
3.2964	0.54 ± 0.03	-0.16 ± 0.05	unphysical result / interference
3.3331	0.19 ± 0.04	0.31 ± 0.05	
3.3591	0.14 ± 0.03	-0.42 ± 0.04	
3.3855	0.14 ± 0.04	0.15 ± 0.05	
3.4038	0.24 ± 0.03	-0.25 ± 0.05	
3.4079	0.33 ± 0.03	-0.18 ± 0.05	unphysical result / interference
3.4105[b]	-0.02 ± 0.03	0.05 ± 0.05	
3.4347	0.17 ± 0.03	-0.10 ± 0.05	
3.5021[c]	0.08 ± 0.04	0.08 ± 0.05	
3.5048	0.64 ± 0.04	0.23 ± 0.06	unphysical result / wrong J^π
3.5490	0.16 ± 0.03	-0.24 ± 0.05	

Table 4.1 - continued

E_p (MeV)	a_2	a_4	remarks
3.5720	0.05 ± 0.04	0.21 ± 0.05	
3.5924	0.12 ± 0.04	0.07 ± 0.05	
3.6180	-0.10 ± 0.03	0.00 ± 0.05	
3.6326	0.61 ± 0.03	-0.29 ± 0.05	unphysical result / wrong J^π
3.6348	0.05 ± 0.03	-0.08 ± 0.05	
3.6886	0.16 ± 0.03	-0.25 ± 0.05	
3.7232	0.11 ± 0.03	-0.37 ± 0.05	poor elastic result / interference
3.7362	0.12 ± 0.03	-0.64 ± 0.04	
3.7675	0.18 ± 0.02	-0.98 ± 0.03	unphysical result / interference
3.8150	-0.23 ± 0.03	-0.21 ± 0.04	unphysical result / interference
3.8266	0.89 ± 0.04	0.11 ± 0.05	unphysical result / interference
3.8348	-0.13 ± 0.03	-0.25 ± 0.04	poor elastic result / interference
3.8795	0.62 ± 0.04	-0.16 ± 0.06	unphysical result / interference
3.9108	0.13 ± 0.04	0.04 ± 0.05	
3.9508	0.74 ± 0.03	-0.88 ± 0.05	unphysical result / wrong J^π
3.9636	0.17 ± 0.03	-0.15 ± 0.05	
3.9982	0.07 ± 0.03	-0.15 ± 0.05	

[a] The values a_2 = -0.15 and a_4 = 0.03 were used to calculate the partial widths of this resonance.

[b] The values a_2 = -0.10 and a_4 = 0.00 were used to calculate the partial widths of this resonance.

[c] The values a_2 = 0.10 and a_4 = 0.02 were used to calculate the partial widths of this resonance.

Figure 4.4 Excitation functions and R-matrix fits for the two solutions for the resonance at E_p = 3.5490 MeV. The upper figure shows the fit for the solution which is primarily l = 2 while the lower figure show the fit for the solution which is mostly l = 0.

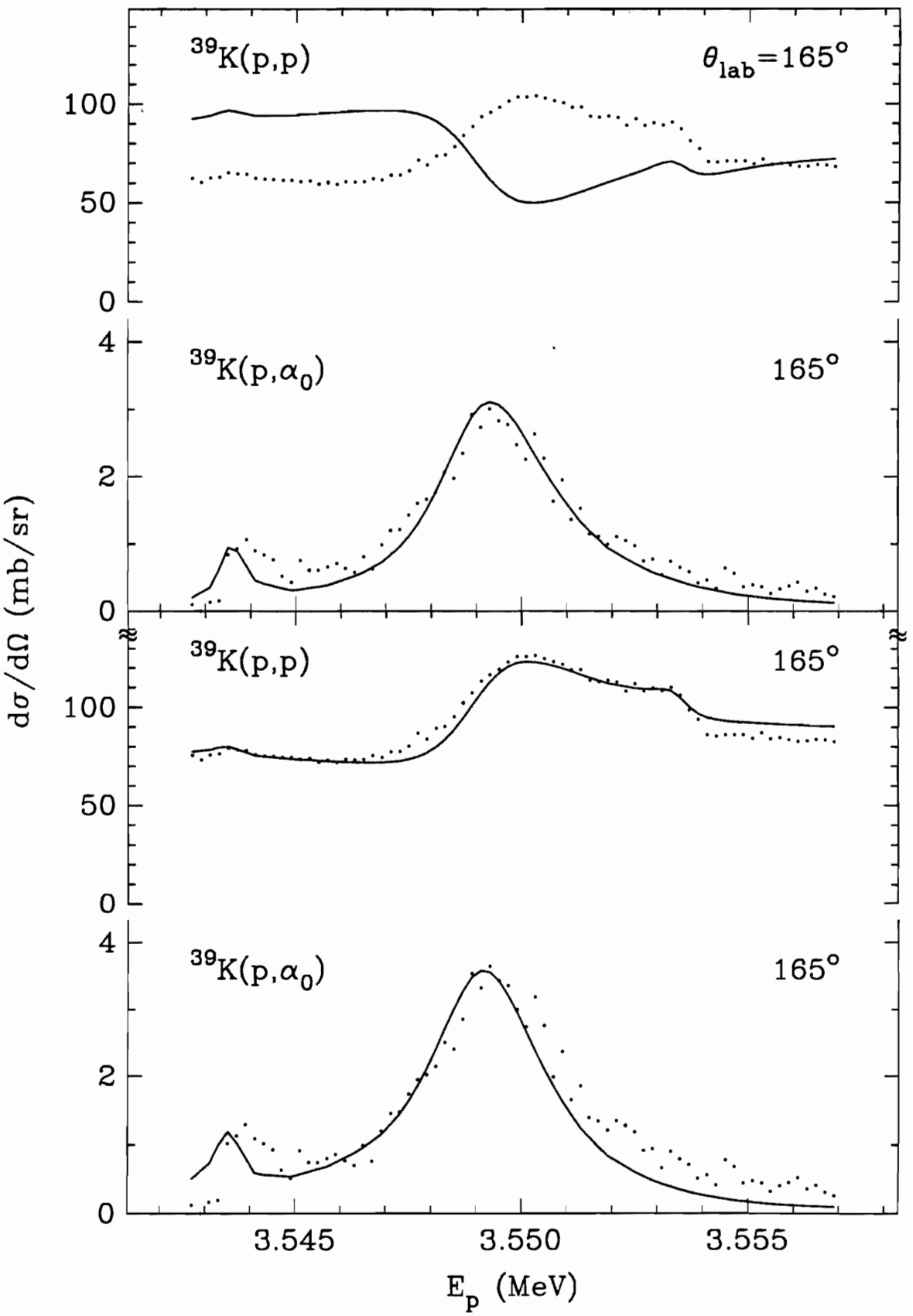
^{39}K(p,p)
θ_{lab}=165°
100
50
0
^{39}K(p,α_0)
165°
4
2
0
^{39}K(p,p)
165°
100
50
0
^{39}K(p,α_0)
165°
4
2
0
3.545
3.550
3.555
E_p (MeV)
dσ/dΩ (mb/sr)

placed these resonances inside the ellipse of Figure 4.3, allowing only one set of widths as a solution to the angular correlation equations. A value of a_2 and a_4 in this region implies that most of the proton strength is $l = 2$, but the elastic scattering data indicates that these states are primarily *s*-wave resonances. The values of a_2 and a_4 which lie on the ellipse and are closest to the experimental values were determined, and based on these values, another set of partial widths were calculated for each resonance. These new values of a_2 and a_4 are within a standard deviation of the experimental values, except for the a_4 values of two of the resonances. For the resonance at $E_p = 3.5021$ MeV, the new a_4 value is 0.02, which is outside of the standard error range by 0.01. The value of a_4 for the resonance at $E_p = 2.7859$ MeV is 0.03, over two standard deviations away from the experimental value. The partial width solutions of all of these adjusted values of a_2 and a_4 have a large value of Γ_{20}, and these results agree with the elastic scattering data. These values of a_2 and a_4 were used to calculate the reduced widths and amplitudes for these resonances.

Table 4.2 lists the final values of the total proton and alpha laboratory and reduced widths, while Table 4.3 lists the values of the reduced widths and the one set of amplitude products found for the 30 2^+ resonances. The errors in the reduced widths are presented in Appendix C. In Figures 4.5 to 4.9 the reduced widths are plotted versus energy. Each of these graphs is divided into three sections, with the magnitude of each width plotted in the lower part, the cumulative sum of the reduced widths shown in the middle section, and the location of the resonances given at the top of the figure. The cumulative sums of the reduced widths show no anomalies versus energy, suggesting that no special states occur in this energy region (*e.g.* fragments of analog states). The products of the reduced width amplitudes $\gamma_{20}\gamma_{22}$ are shown in Figure 4.10. The amplitude products show a steady upward trend in the cumulative sum above $E_p = 3.2$ MeV. If the entrance channels are uncorrelated, then the reduced amplitude products should have a

BULL PhD 1989 $R_0 = ?$

Table 4.2

Total Proton and Alpha Laboratory and Reduced Widths for 30 2^+ Resonances in ^{40}Ca

E_p (MeV)	Γ_p (eV)	γ_p^2 (keV)	Γ_α (eV)	γ_α^2 (keV)
2.3891	350	1.87	4	4.02
2.5130	180	5.64	4	2.99
2.5982	40	0.30	5	2.45
2.6859	215	0.75	11	4.01
2.7859	500	1.35	2	0.50
2.8623	40	0.48	6	1.08
3.0114	325	3.71	16	1.95
3.0705	475	0.90	41	4.13
3.1157	88	0.83	100	8.80
3.1322	2500	4.22	65	5.43
3.1883	200	1.70	15	1.04
3.2125	1030	3.35	140	9.48
3.2681	500	2.31	115	6.53
3.3331	180	0.66	45	2.10
3.3591	250	1.70	30	1.29
3.3855	70	0.40	15	0.60
3.4038	600	3.58	2	0.06
3.4105	1500	1.89	90	3.50
3.4347	180	0.29	775	28.03
3.5021	750	0.83	320	9.59
3.5490	2200	3.54	340	9.22
3.5720	770	3.75	975	24.72
3.5924	70	0.32	230	5.60
3.6180	325	0.33	60	1.37
3.6348	450	0.48	420	9.21
3.6886	2200	3.10	2	0.05

Table 4.2 continued

E_p (MeV)	Γ_p (eV)	γ_p^2 (keV)	Γ_α (eV)	γ_α^2 (keV)
3.7362	240	0.88	18	0.32
3.9108	1000	0.88	240	2.82
3.9636	1000	1.03	240	2.51
3.9982	425	1.34	9	9.12

Table 4.3

Proton Partial Reduced Widths and Amplitude Products
for 30 2^+ Resonances in ^{40}Ca

E_p (MeV)	γ_{20}^2 (keV)	γ_{12}^2 (keV)	γ_{22}^2 (keV)	$\gamma_{20}\gamma_{22}$ (keV)
2.3891	1.31	0.56	0.00	0.08
2.5130	0.01	1.26	4.37	0.23
2.5982	0.09	0.08	0.13	-0.11
2.6859	0.48	0.26	0.02	-0.09
2.7859	0.99	0.00	0.37	-0.60
2.8623	0.02	0.28	0.18	0.06
3.0114	0.02	2.36	1.33	0.15
3.0705	0.65	0.24	0.01	0.06
3.1157	0.01	0.18	0.65	0.06
3.1322	3.27	0.61	0.34	1.06
3.1883	0.01	1.28	0.41	0.07
3.2125	0.94	1.13	1.29	1.10
3.2681	0.29	1.79	0.24	0.26
3.3331	0.12	0.00	0.54	0.25
3.3591	0.00	0.80	0.90	-0.04
3.3855	0.01	0.09	0.30	0.06
3.4038	0.05	1.46	2.07	0.33
3.4105	1.57	0.00	0.00	0.00
3.4347	0.16	0.09	0.04	0.09
3.5021	0.71	0.00	0.12	0.30
3.5490	1.75	1.67	0.12	0.45
3.5720	0.04	0.78	2.93	0.34
3.5924	0.01	0.09	0.23	0.04
3.6180	0.28	0.01	0.04	-0.10
3.6348	0.38	0.10	0.00	0.01
3.6886	1.57	1.46	0.07	0.32

Table 4.3 continued

E_p (MeV)	γ_{20}^2 (keV)	γ_{12}^2 (keV)	γ_{22}^2 (keV)	$\gamma_{20}\gamma_{22}$ (keV)
3.7362	0.03	0.52	0.33	-0.10
3.9108	0.69	0.00	0.19	0.36
3.9636	0.61	0.33	0.09	0.24
3.9982	0.00	0.48	0.86	0.01

Figure 4.5 Proton reduced widths and cumulative sum of reduced widths versus energy for the 2^+ resonances in ^{40}Ca. The resonance locations are shown at the top of the figure.

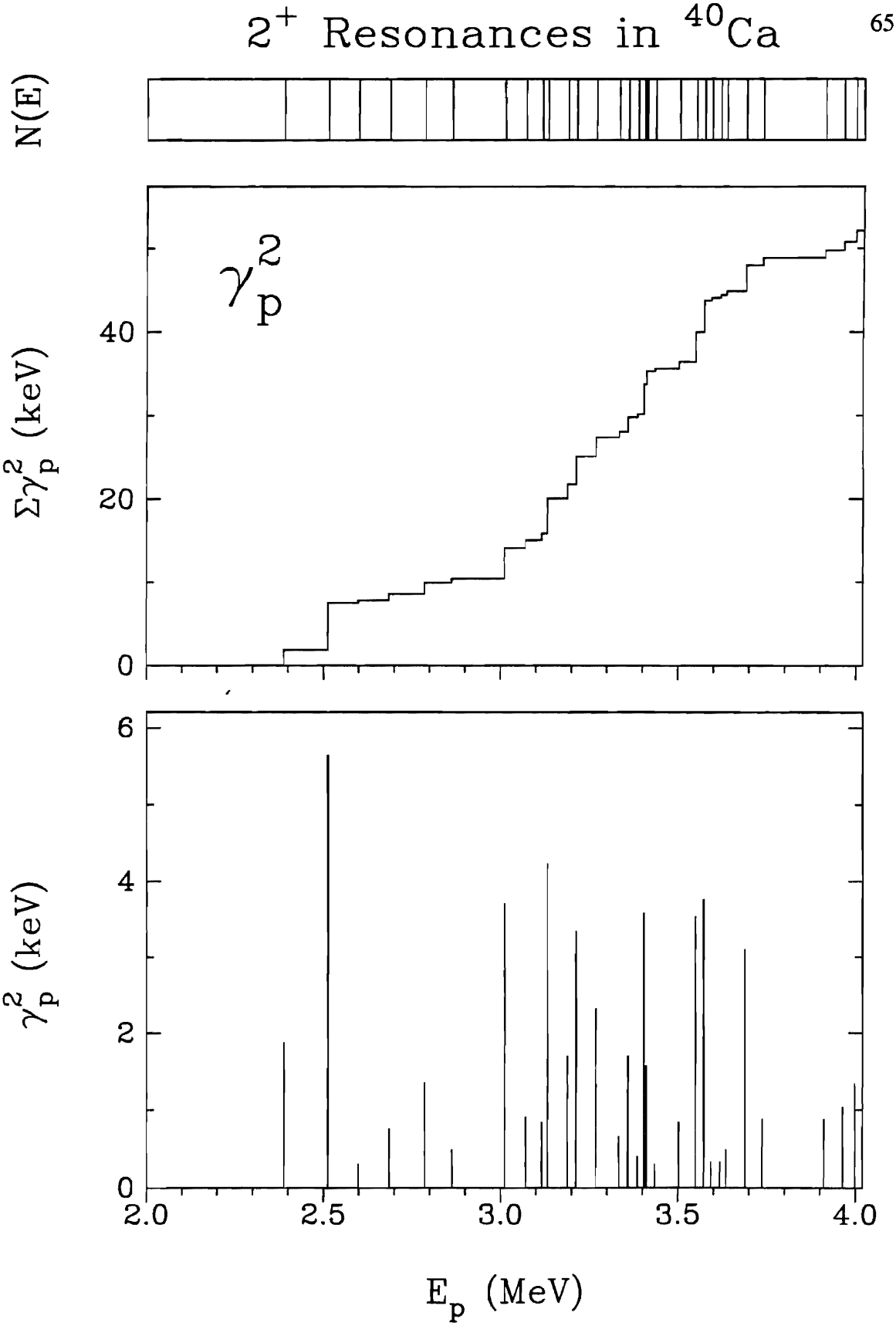
2+ Resonances in 40Ca
N(E)
γ²p
ΣΓ²p (keV)
40
20
0
Γ²p (keV)
6
4
2
0
2.0
2.5
3.0
3.5
4.0
Ep (MeV)

Figure 4.6 Alpha reduced widths and cumulative sum of reduced widths versus energy for the 2^+ resonances in ^{40}Ca. The resonance locations are shown at the top of the figure.

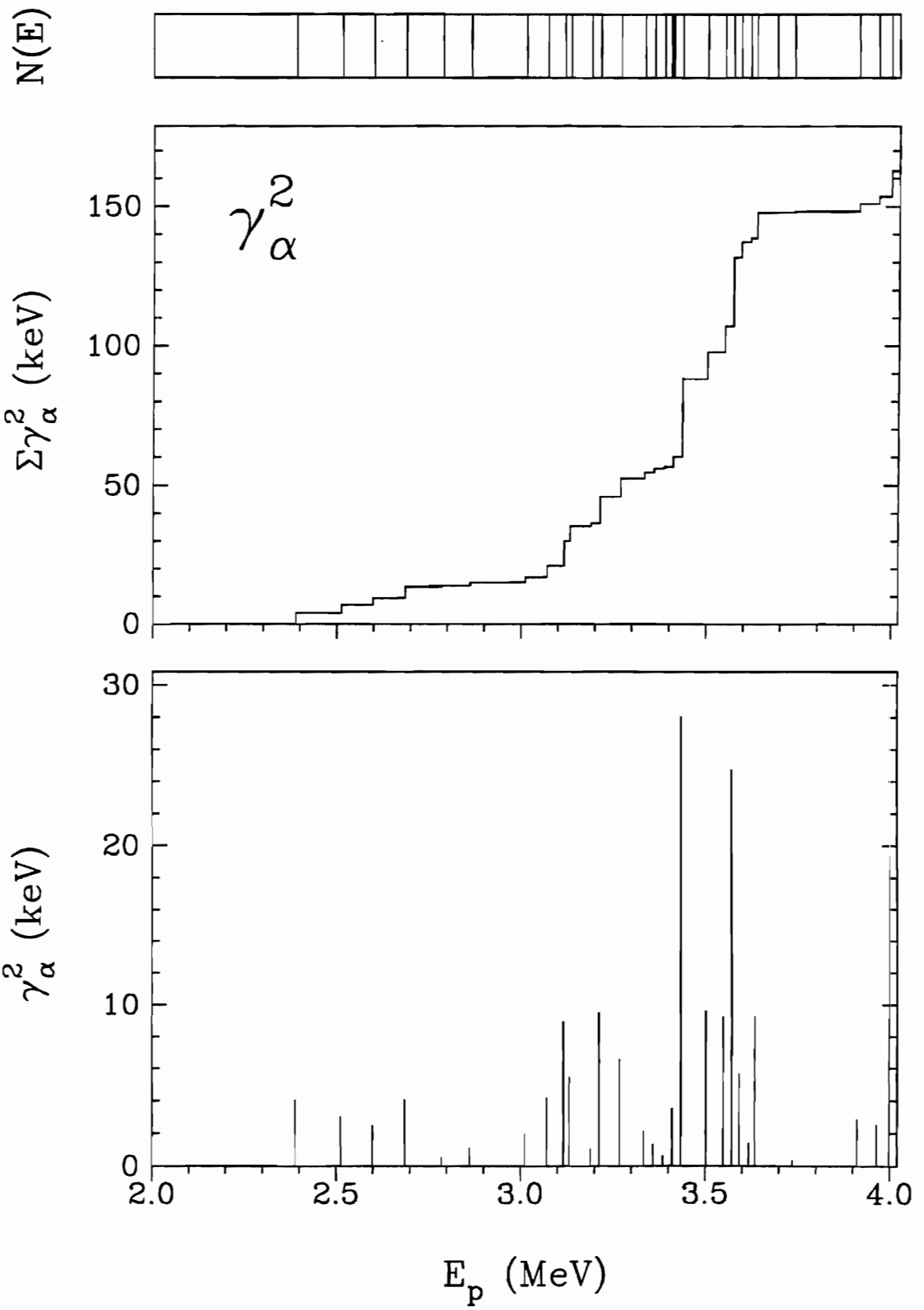
2+ Resonances in 40Ca
N(E)
γ_α^2
$\Sigma\gamma_\alpha^2$ (keV)
150
100
50
0
γ_α^2 (keV)
30
20
10
0
2.0
2.5
3.0
3.5
4.0
E_p (MeV)

Figure 4.7 The $s = 2, l = 0$ proton reduced widths and cumulative sum of reduced widths versus energy for the 2^+ resonances in ^{40}Ca. The resonance locations are shown at the top of the figure.

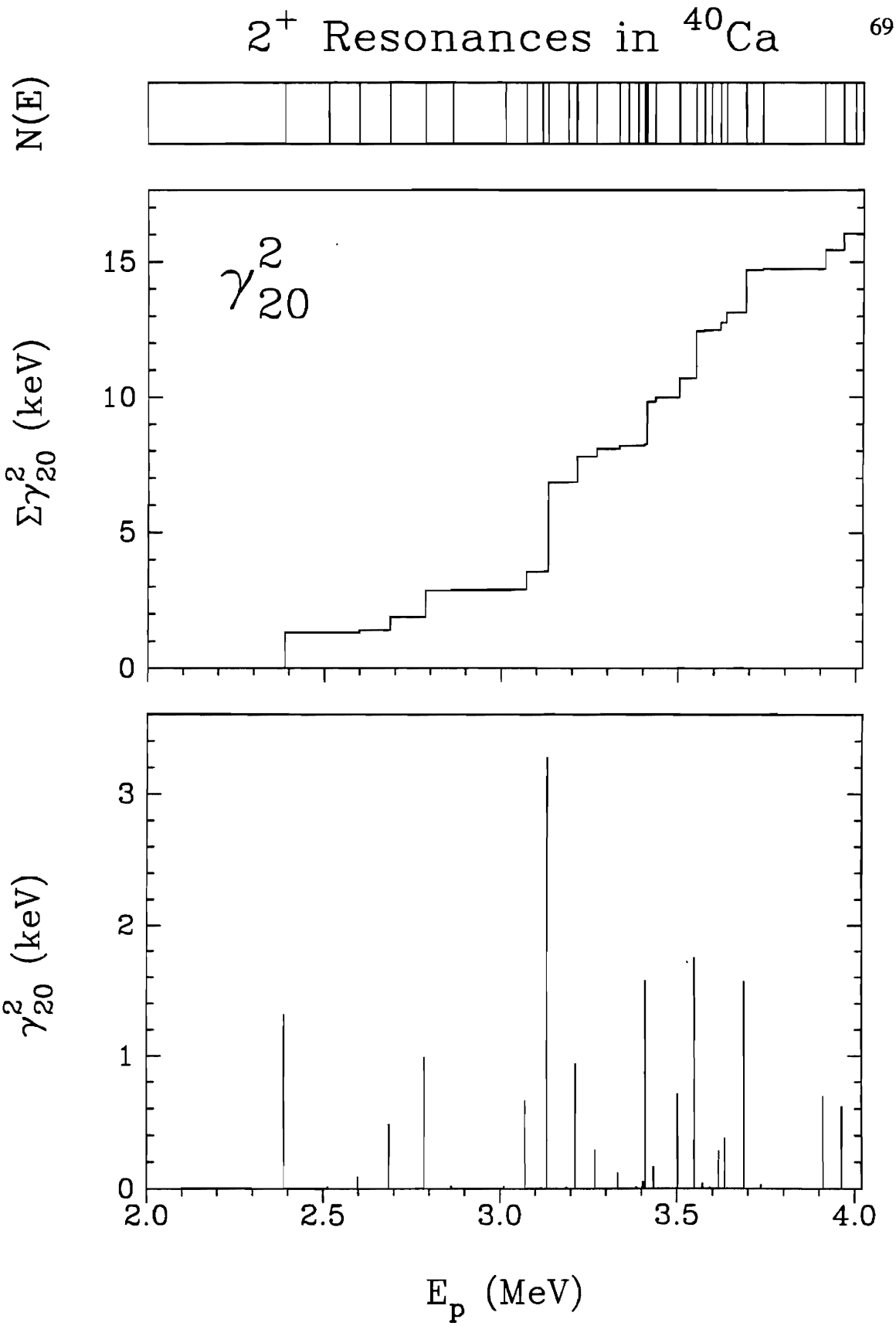
2+ Resonances in 40Ca
N(E)
γ^2_{20}
$\Sigma\gamma^2_{20}$ (keV)
15
10
5
0
γ^2_{20} (keV)
3
2
1
0
2.0
2.5
3.0
3.5
4.0
E_p (MeV)

Figure 4.8 The $s = 1, l = 2$ proton reduced widths and cumulative sum of reduced widths versus energy for the 2^+ resonances in ^{40}Ca. The resonance locations are shown at the top of the figure.

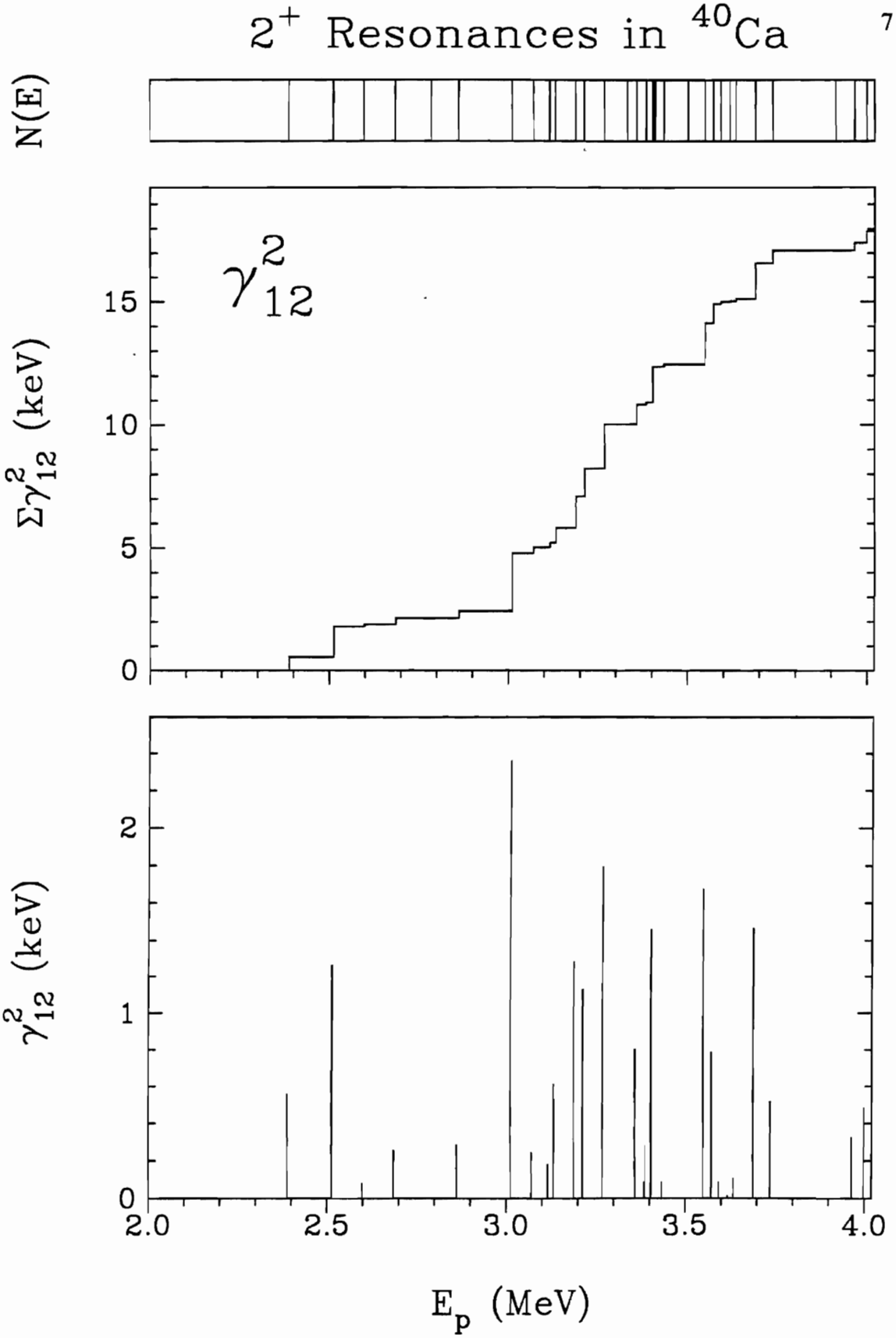
2+ Resonances in 40Ca
N(E)
γ²12
Σγ²12 (keV)
15
10
5
0
γ²12 (keV)
2
1
0
2.0
2.5
3.0
3.5
4.0
Ep (MeV)

Figure 4.9 The $s = 2$, $l = 2$ proton reduced widths and cumulative sum of reduced widths versus energy for the 2^+ resonances in ^{40}Ca. The resonance locations are shown at the top of the figure.

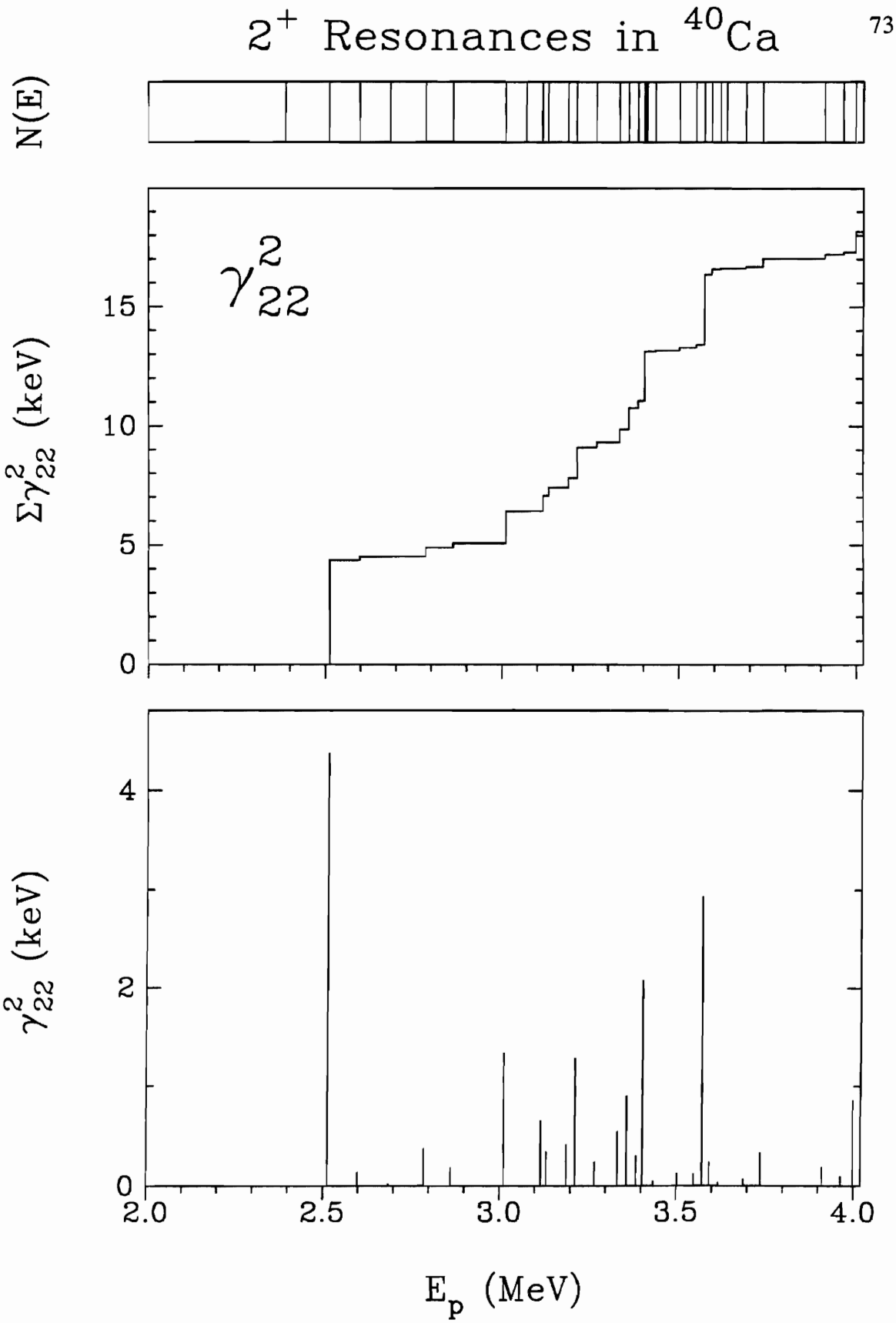
2+ Resonances in 40Ca
N(E)
γ^2_{22}
$\Sigma\gamma^2_{22}$ (keV)
0
5
10
15
γ^2_{22} (keV)
0
2
4
2.0
2.5
3.0
3.5
4.0
E_p (MeV)

Figure 4.10 The products of amplitudes γ_{20} and γ_{22} and their cumulative sum versus energy for the 2^+ resonances in ^{40}Ca. The resonance locations are shown at the top of the figure.

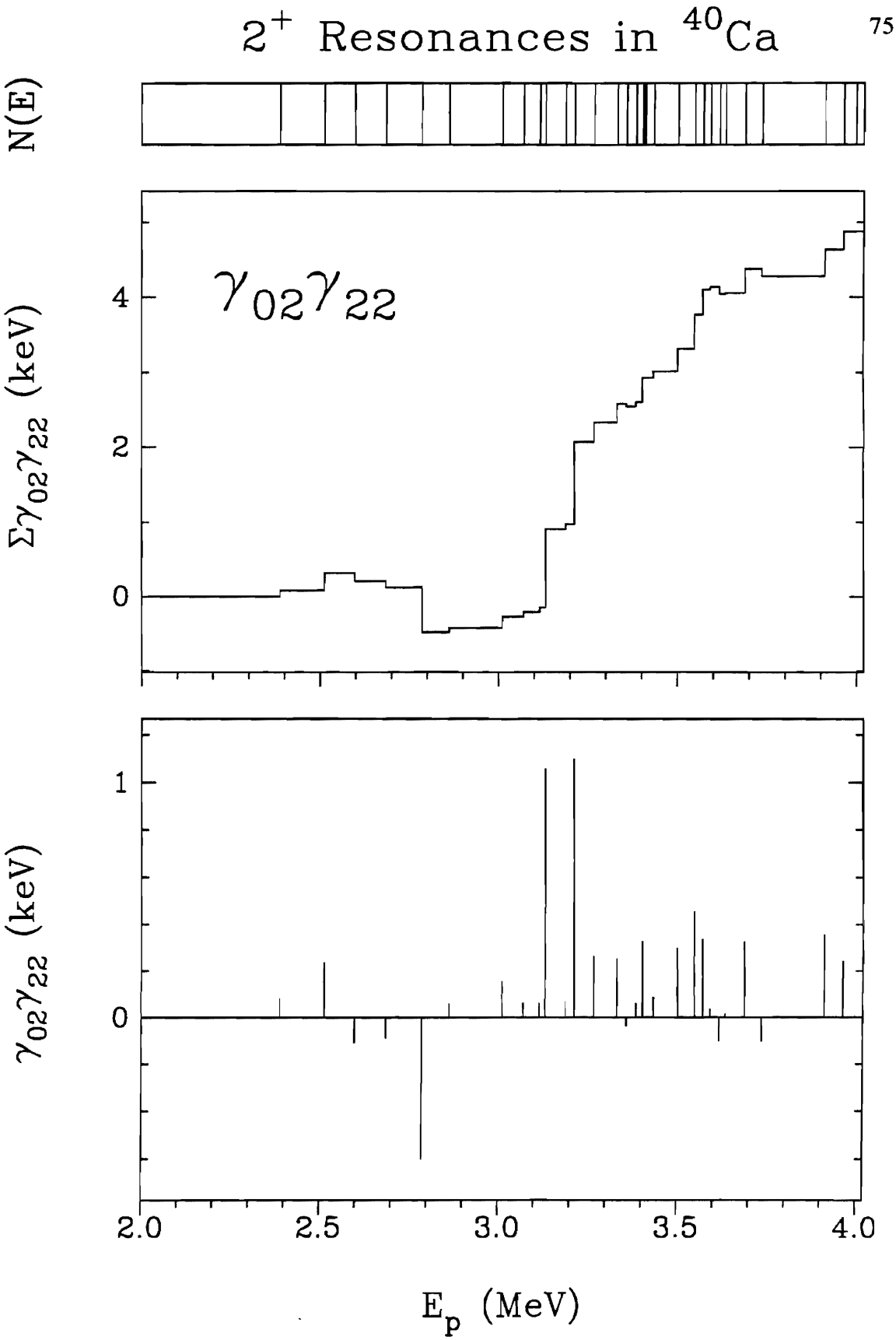
2+ Resonances in 40Ca
N(E)
γ02γ22
Σγ02γ22 (keV)
4
2
0
γ02γ22 (keV)
1
0
2.0
2.5
3.0
3.5
4.0
Ep (MeV)

random sign distribution. The relative signs of the $\gamma_{20}\gamma_{22}$ amplitude products are clearly nonrandom, with 24 of 30 amplitude products positive.

Section C. Results for 1^- Resonances

In the previous study, 51 resonances were assigned a J^π value of 1^-. The (p,α_0) angular distributions were obtained for only 25 of these resonances. Of the 26 unmeasured resonances, most of the resonances were too weak to study in the alpha channel, while the rest of the resonances showed too much interference with neighboring resonances. The 25 (p,α_0) angular distributions measured were fit to the form of Eqn. 4.1. A list of the a_2 coefficients determined from the Legendre fit is given in Table 4.4. Of these 25 resonances, satisfactory partial values were obtained for only 13 resonances. Of the remaining 12 resonances, the J^π value was changed for 5 of the resonances, and acceptable fits to the elastic scattering data were not obtained for 7 of the resonances. These latter resonances include states which interfered with other resonances and states which had elastic widths too small to determine accurately the proton partial widths. Table 4.4 summarizes all of these results.

The process for obtaining the proton partial widths relied heavily on the elastic scattering data. First the a_2 value for an angular distribution was determined. Then the channel mixing ratio ξ and the orbital angular momentum mixing angle ψ_2 were connected, via the Legendre coefficient equation from Table 2.1. This relation reduced the possible combinations of the proton partial widths; the value of ψ_2 determines the values of the proton partial widths. Utilizing a modified version of MULTI6, a minimum χ^2 search routine was then used to find the best value of ψ_2 by comparing the calculated elastic cross section with the elastic scattering data. The search procedure was identical

Table 4.4

Legendre Coefficients for (p, α_0) Angular Distributions for 1^- Resonances in ^{40}Ca

E_p (MeV)	a_2	remarks
2.2446	-0.81 ± 0.01	
2.3876	1.28 ± 0.03	unphysical a_2 result / interference
2.4076	-0.75 ± 0.02	
2.5154	0.90 ± 0.03	poor elastic result / wrong J^π
2.6522	0.14 ± 0.03	
2.6711	0.16 ± 0.04	
2.8207	1.00 ± 0.03	unphysical a_2 result / interference
3.0793	-0.01 ± 0.03	
3.1984	-0.29 ± 0.03	
3.3671	0.87 ± 0.03	poor elastic result / wrong J^π
3.3948	0.73 ± 0.04	Γ_p too small for conclusive results
3.4190	-0.18 ± 0.03	
3.4651	-0.07 ± 0.03	
3.4905	-0.54 ± 0.02	poor elastic result / interference
3.5092	-0.81 ± 0.01	
3.5136	0.37 ± 0.04	poor Legendre fit / wrong J^π
3.5817	0.14 ± 0.04	poor elastic result / wrong J^π
3.5924	0.10 ± 0.03	poor elastic result / wrong J^π
3.6408	0.53 ± 0.03	
3.7094	1.33 ± 0.06	unphysical a_2 result / interference
3.7404	0.98 ± 0.04	Γ_p too small for conclusive result
3.8457	-0.71 ± 0.02	
3.9481	-0.26 ± 0.03	
3.9636	0.80 ± 0.03	poor elastic result / interference
4.0178	-0.36 ± 0.26	

with the routine used to determine the alpha widths, except that the search was performed over more than one parameter. During the data analysis, it was observed that the signs of the reduced width amplitudes sometimes had a marked effect on the proton and alpha cross sections. Thus, for each resonance an initial search over the variables ψ_2 and Γ_p was performed four times, changing the combination of the relative signs of the reduced width amplitudes for each separate attempt. From the best fit of these four attempts, a final search was enacted over three parameters (ψ_2, Γ_p, and E_p) to obtain final values for the partial widths. As discussed in Chapter II, often there is a second set of proton partial widths which will produce an identical elastic cross section. The second solution was determined from the equation relating ξ and ψ_2 by calculating the second set of widths with the same magnitude of Γ_{23} as obtained in the first solution. The elastic cross sections calculated from the two sets of widths were found to give nearly identical resonance shapes. Table 4.5 lists the alpha and proton widths obtained for 13 1^- resonances in ^{40}Ca, with the preferred solution listed first for each resonance. The signs on the proton partial widths indicate the relative signs of the reduced width amplitudes.

Although the dual solutions for the 1^- resonances prevent the determination of correlations between the entrance channels, the in-depth study of both the 1^- resonances and the 2^+ resonances has provided valuable additional spectroscopic information for the ^{39}K(p,p$_0$)^{39}K and the ^{39}K(p,α_0)^{36}Ar reactions. The angular correlation studies of the (p, α_0) resonances have confirmed some resonance assignments and corrected others, while improving the overall resonance spectroscopy by the reexamination of nearby resonances. During the analysis of these experiments, the parameters of a number of resonances were changed. Table B.1 in the appendix summarizes all the changes made to the resonance parameters of ^{40}Ca obtained by Warthen (1987).

Table 4.5

Proton and Alpha Partial Widths for 13 1^- Resonances in ^{40}Ca

E_p (MeV)	Γ_p (eV)	Γ_α (eV)	Γ_{11}* (eV)	Γ_{21}* (eV)	Γ_{23}* (eV)
2.2446	2400.	15.	2000.	200.	150.
			2150.	100.	-150.
2.4076	1200.	60.	-950.	250.	10.
			-1000.	200.	-10.
2.6522	4700.	35.	650.	4000.	-10.
			no second solution		
2.6711	2600.	10.	200.	2400.	-5.
			10.	2600.	5.
3.0793	3500.	25.	1100.	2300.	-130.
			200.	3200.	130.
3.1984	5500.	300.	1700.	3600.	200.
			2900.	2400.	-200.
3.4190	75.	1100.	10.	50.	15.
			45.	15.	-15.
3.4651	320.	5.	-55.	100.	170.
			-160.	0.	170.
3.5092	2800.	750.	-2300.	500.	40.
			-2500.	300.	-40.
3.6408	630.	10.	75.	450.	-100.
			no second solution		
3.8457	1300.	35.	-950.	350.	5.
			-1000.	300.	-5.
3.9481	250.	65.	-100.	150.	-5.
			-75.	150.	5.
4.0178	1000.	1100.	-550.	450.	-15.
			-400.	600.	15.

*The signs on the partial widths indicate the relative signs of the reduced width amplitudes.

CHAPTER V

STATISTICAL PROPERTIES

A. Introduction

The proton separation energy for $^{39}K + p$ is 8.3 MeV, placing the excitation energies of the resonances studied in this experiment between 10.7 MeV and 12.3 MeV. In this energy region of the nucleus there are a large number of states, making it impractical to examine the properties of individual resonances. Instead, a statistical approach is used to analyze the resonances as a group by considering such properties as level spacings and reduced width and reduced width amplitude distributions. The rest of this section will give a brief theoretical background to the statistical properties of nuclei, followed by several sections which will discuss the application of these models to the 2^+ resonances in ^{40}Ca.

The first step in considering the statistical properties of any quantum mechanical system is the derivation of the appropriate Hamiltonian. Wigner (1951) was the first to postulate that the Hamiltonian could be treated as a random variable with a probability distribution $P(H)$. This distribution is then constrained by the properties of certain conserved quantities such as spin and parity. Thus numerous forms of $P(H)$ can be derived under various assumptions concerning the fundamental symmetries. Typically, the Hamiltonian is represented as a matrix, **H**, with components defined as

$$H_{ij} = \int \varphi_i^* H \varphi_j \, d\tau \, . \tag{5.1}$$

Here, the φ_i form a set of basis vectors in Hilbert space on which **H** is defined. The integration is performed over $3A$ variables, where A is the number of particles in the nucleus. By choosing a subset of the basis vectors φ_i, the infinite-dimensional Hilbert space can be reduced to an N-dimensional space where N is much greater than the number of levels under consideration. The result, if spin and parity are conserved, is a block diagonal matrix with each block encompassing all the energy levels with the same J^π. The interactions of levels in the same block are strong, and therefore dominate within the entire matrix, causing the blocks of different J^π to be statistically uncorrelated. A number of early papers on this method have been collected by Porter (1965) and a comprehensive review of random matrices has been given by Brody *et al.* (1981).

Constraining **H** to satisfy both time reversal invariance and rotational invariance forces **H** to be a real symmetric matrix. One further condition often employed is that the independent elements of **H** be statistically independent, which leads to a Gaussian distribution for the matrix elements. An ensemble of matrices satisfying these criteria is known as a Gaussian Orthogonal Ensemble (GOE). Recent work in quantum chaos has led to the concept that time-reversal invariant systems whose classical analogs are chaotic are also described by the GOE (Bohigas, 1984). Weidenmüller (1986) differentiates the regular and chaotic nature of the compound nucleus by describing two different types of features in nuclei: averages and fluctuations. Average properties are those such as the average level spacing and the mean value of S-matrix elements, which are determined from values averaged over many compound nuclear states of the same J^π. Fluctuations, on the other hand, are individual variations about these average values. They are generic to many types of systems, chaotic in nature, and are described by the GOE.

One of the first uses of random-matrix theory was to predict the distribution of level spacings (Wigner, 1957). This model predicts that the energy eigenvalues should be distributed according to the relation

$$P(E_\lambda) \propto \prod_{\mu<\lambda} |E_\lambda - E_\mu| e^{-a(E_\lambda - E_0)^2}. \qquad (5.2)$$

While many sets of data have been shown to obey this relation, the example cited most often is neutron scattering from ^{166}Er (Liou, 1972). For charged particle scattering, the $1/2^+$ resonances in ^{57}Co also show excellent agreement with the predicted distribution (Watson, 1981). A necessary requirement to verify this distribution is a complete set of resonances for a nucleus. In this experiment, however, too many levels were missed to satisfy this condition, and no further discussion of level spacings will be given.

To examine reduced width distributions, it is only necessary to have a reasonably large, but random, collection of resonances. Due to the energy resolution of the beam, resonances with smaller total widths are not detected in proton scattering experiments. However, the partial decay widths do consist of a random sample, since a resonance may be strong in one channel but weak in another, and still be observed. Porter and Thomas (1956) found that the distribution of neutron reduced widths is the same as a χ^2 random variable distribution with one degree of freedom. This distribution, known as the Porter-Thomas distribution, can be expressed as

$$P(y) = \frac{1}{\sqrt{2\pi y}} e^{-\frac{y}{2}}, \text{ where } y = \frac{\gamma^2}{\langle \gamma^2 \rangle}. \qquad (5.3)$$

This distribution implies that the reduced width amplitudes are distributed according to a Gaussian distribution.

The probability distribution for reduced width amplitudes was derived by Krieger and Porter (1963). Let there be m channels labeled by c, c', c'', etc. The reduced width amplitudes for channel c are labeled $\gamma_{\lambda c}$ and the covariance matrix Σ is defined as

$$\Sigma_{cc'} = \langle \gamma_{\lambda c} \gamma_{\lambda c'} \rangle . \tag{5.4}$$

Then the probability distribution for reduced width amplitudes is

$$P_{cc'c''\ldots} = \prod_{\lambda} \frac{\sqrt{|\mathbf{M}|}}{(2\pi)^{m/2}} e^{-\frac{1}{2}(\gamma_\lambda, \mathbf{M}\gamma_\lambda)}, \tag{5.5}$$

where $\mathbf{M} = \Sigma^{-1}$ and γ_λ is the vector $(\gamma_{\lambda c}, \gamma_{\lambda c''}, \gamma_{\lambda c'''}, \ldots)$. To obtain the distribution for a single channel, Eqn. 5.5 must be integrated over all channels but one. For a single channel, this result is

$$P(\gamma) = \frac{1}{\sqrt{2\pi \langle \gamma^2 \rangle}} e^{-\frac{\gamma^2}{2\langle \gamma^2 \rangle}}, \tag{5.6}$$

which leads to the Porter-Thomas distribution.

Another facet of the Krieger-Porter theory is the existence of linear correlations between the reduced width amplitudes. Unless $\mathbf{M}$ is diagonal, $P_{cc'c''}$ is not independent with respect to channel, and correlations can exist between the reduced width amplitudes. However, the Porter-Thomas distribution says nothing about width correlations. The linear correlation coefficient between two sets of data x_i and y_i is defined as

$$\rho(x, y) = \frac{\sum_i (x_i - \langle x \rangle)(y_i - \langle y \rangle)}{\sqrt{\sum_i (x_i - \langle x \rangle)^2 \sum_i (y_i - \langle y \rangle)^2}}. \tag{5.7}$$

If ρ is equal to ± 1, then the two sets of data are completely correlated, or if x and y are completely independent of each other, $\rho = 0$. Assuming $\langle \gamma_c \rangle = 0$, the amplitude correlation coefficient becomes

$$\rho(\gamma_c, \gamma_{c'}) = \frac{\langle \gamma_c \gamma_{c'} \rangle}{\sqrt{\langle \gamma_c^2 \rangle \langle \gamma_{c'}^2 \rangle}}. \tag{5.8.}$$

This leads to a simple relationship between the correlation coefficients of the reduced widths and reduced width amplitudes:

$$\rho\left(\gamma_c^2, \gamma_{c'}^2\right) = \rho^2(\gamma_c, \gamma_{c'}) . \tag{5.9}$$

This equation implies that the width correlations must be non-negative.

From the Krieger-Porter results one can obtain the probability distributions for reduced width amplitude ratios. These distributions have been calculated by Chou *et al.* (1980) for both the two and three channel case. Define a mixing ratio $\delta = \gamma_2 / \gamma_1$ where γ_1 and γ_2 are amplitudes. Since absolute signs cannot be measured, we shall assume γ_1 is positive. In order to obtain a variable with a finite range, define the mixing angle $\phi = \tan^{-1} \delta$, where the range of ϕ is limited to $\pm 90°$. The probability distribution of ϕ is

$$P(\phi) = \frac{\sqrt{|\mathbf{M}|}}{\pi \left(M_{11} \cos^2 \phi + M_{22} \sin^2 \phi + M_{12} \sin 2\phi \right)} , \tag{5.10}$$

where

$$|\mathbf{M}| = \frac{1}{\left\langle \gamma_1^2 \right\rangle \left\langle \gamma_2^2 \right\rangle - \left\langle \gamma_1 \gamma_2 \right\rangle^2} \tag{5.11}$$

and

$$M_{11} = \left\langle \gamma_2^2 \right\rangle |\mathbf{M}| \qquad M_{22} = \left\langle \gamma_1^2 \right\rangle |\mathbf{M}| \qquad M_{12} = - \left\langle \gamma_1 \gamma_2 \right\rangle |\mathbf{M}| . \tag{5.12}$$

If the two channels are uncorrelated, then $M_{12} = 0$. If in addition $\left\langle \gamma_1^2 \right\rangle = \left\langle \gamma_2^2 \right\rangle$, then P($\phi$) is a uniform distribution.

The Porter-Thomas distribution has been thoroughly tested for both neutron and proton resonances. The Krieger-Porter distribution has only been tested with proton resonances, and only for exit channels with the (p,p′) reaction (Mitchell, 1985). This experiment is the first to test the Krieger-Porter distribution for entrance channels.

Section B. 2^+ Resonances in ^{40}Ca

The 30 2^+ resonances in ^{40}Ca measured in this experiment provide a sufficiently random set of reduced widths and reduced width amplitudes to compare with the theoretical distributions discussed in the previous section. There are no spurious resonances, such as analog states, which would distort the distributions. However, the limited number of resonances is a disadvantage, since for significant statistical comparison between data and theory, more states would be preferable.

The distribution of the alpha reduced widths is shown in the two plots of Figure 5.1. The probability density is illustrated in the upper figure and the cumulative probability is shown in lower figure. In both plots, the smooth curve represents the calculated Porter-Thomas distribution, normalized to 30 levels. The data generally agree well with the density function, but they are initially below the cumulative probability function graph. This effect is caused by the omission of the smaller alpha widths, which, because of their size, were not measured. The distributions of the proton partial reduced widths γ_{20}^2, γ_{12}^2, and γ_{22}^2 are shown in Figures 5.2 - 5.4. In these graphs, the smaller widths are observed, and the widths agree with the Porter-Thomas distribution better than the did alpha widths. The γ_{22}^2 widths agree very well with the Porter-Thomas distribution.

Since γ_p^2 is equal to the sum of the three proton partial reduced widths, only if the partial widths are completely correlated should the distribution of γ_p^2 follow the Porter-Thomas distribution. On the other hand, if the γ_p are uncorrelated, and their mean widths of the three channels are equal, the γ_p should obey a χ^2 distribution with three degrees of freedom. The distribution of the proton reduced widths is shown in Figure 5.5, along with the χ^2 distribution for one (the Porter-Thomas distribution), two, and three degrees of freedom. Although the probability density for the γ_p^2 widths agrees with the Porter-

Figure 5.1 Distribution of the alpha reduced widths for the 2^+ resonances in ^{40}Ca. The upper figure shows the probability density function, and the lower figure shows the cumulative probability function. The smooth curve is the normalized Porter-Thomas distribution.

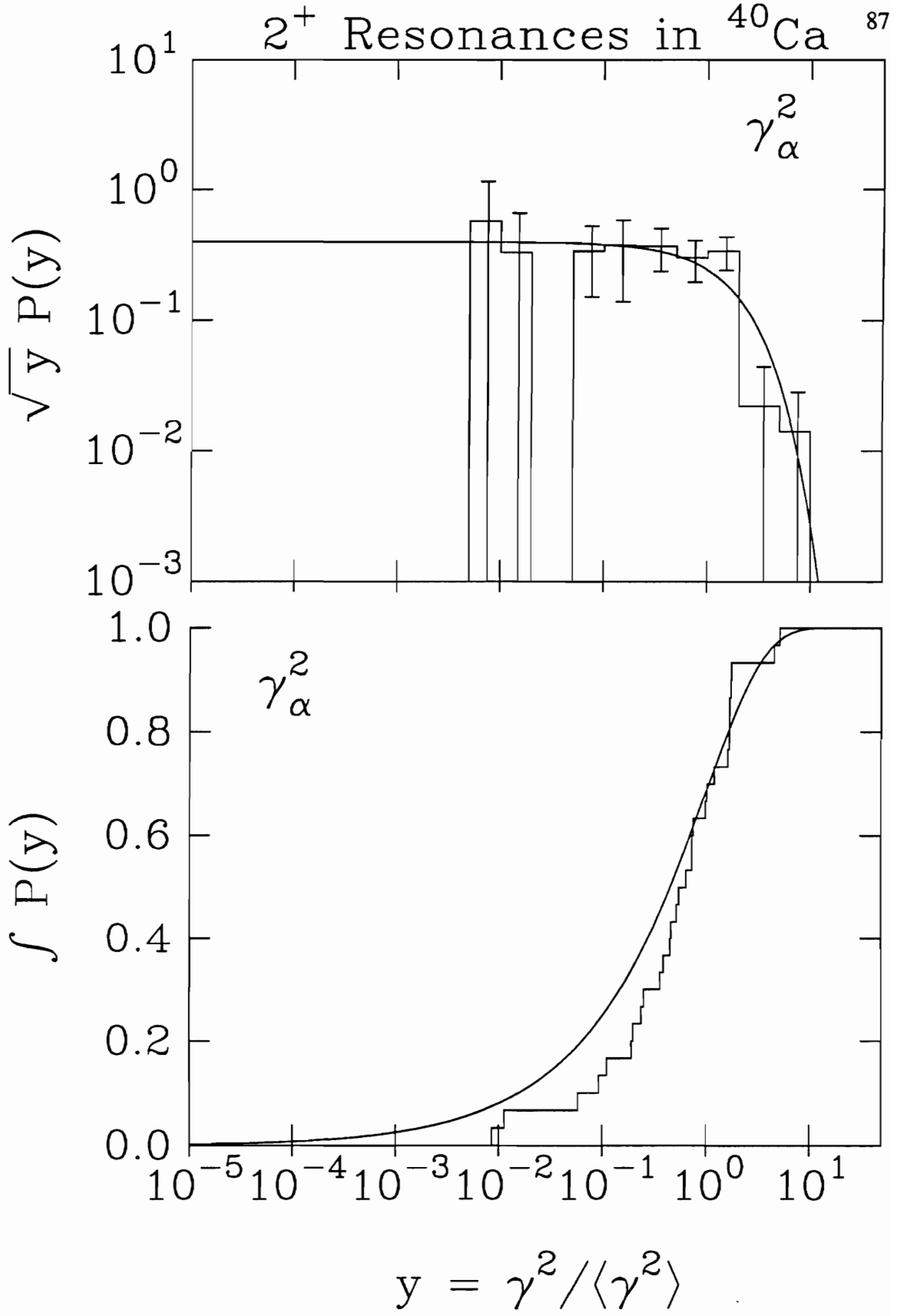
2+ Resonances in 40Ca
γ_α^2
$\sqrt{y}\ P(y)$
10^1
10^0
10^{-1}
10^{-2}
10^{-3}
γ_α^2
$\int P(y)$
1.0
0.8
0.6
0.4
0.2
0.0
10^{-5} 10^{-4} 10^{-3} 10^{-2} 10^{-1} 10^0 10^1
$y = \gamma^2/\langle\gamma^2\rangle$

Figure 5.2 Distribution of the proton reduced widths in the $s = 2, l = 0$ channel for the 2^+ resonances in ^{40}Ca. The upper figure shows the probability density function, and the lower figure shows the cumulative probability function. The smooth curve is the normalized Porter-Thomas distribution.

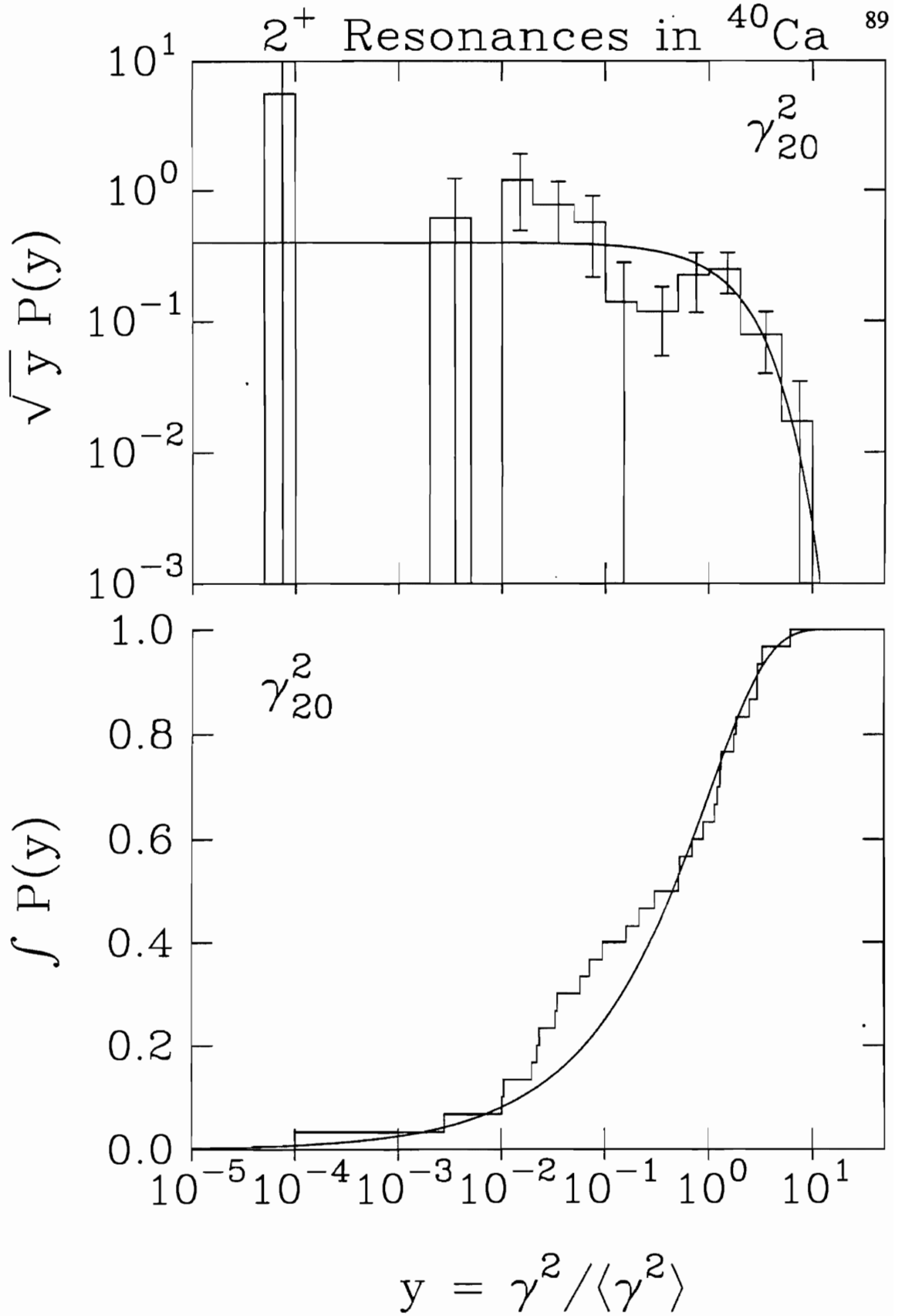
2+ Resonances in 40Ca
γ^2_{20}
$\sqrt{y}\ P(y)$
10^1
10^0
10^{-1}
10^{-2}
10^{-3}
γ^2_{20}
$\int P(y)$
1.0
0.8
0.6
0.4
0.2
0.0
10^{-5} 10^{-4} 10^{-3} 10^{-2} 10^{-1} 10^0 10^1
$y = \gamma^2/\langle\gamma^2\rangle$

Figure 5.3 Distribution of the proton reduced widths in the $s = 1, l = 2$ channel for the 2^+ resonances in ^{40}Ca. The upper figure shows the probability density function, and the lower figure shows the cumulative probability function. The smooth curve is the normalized Porter-Thomas distribution.

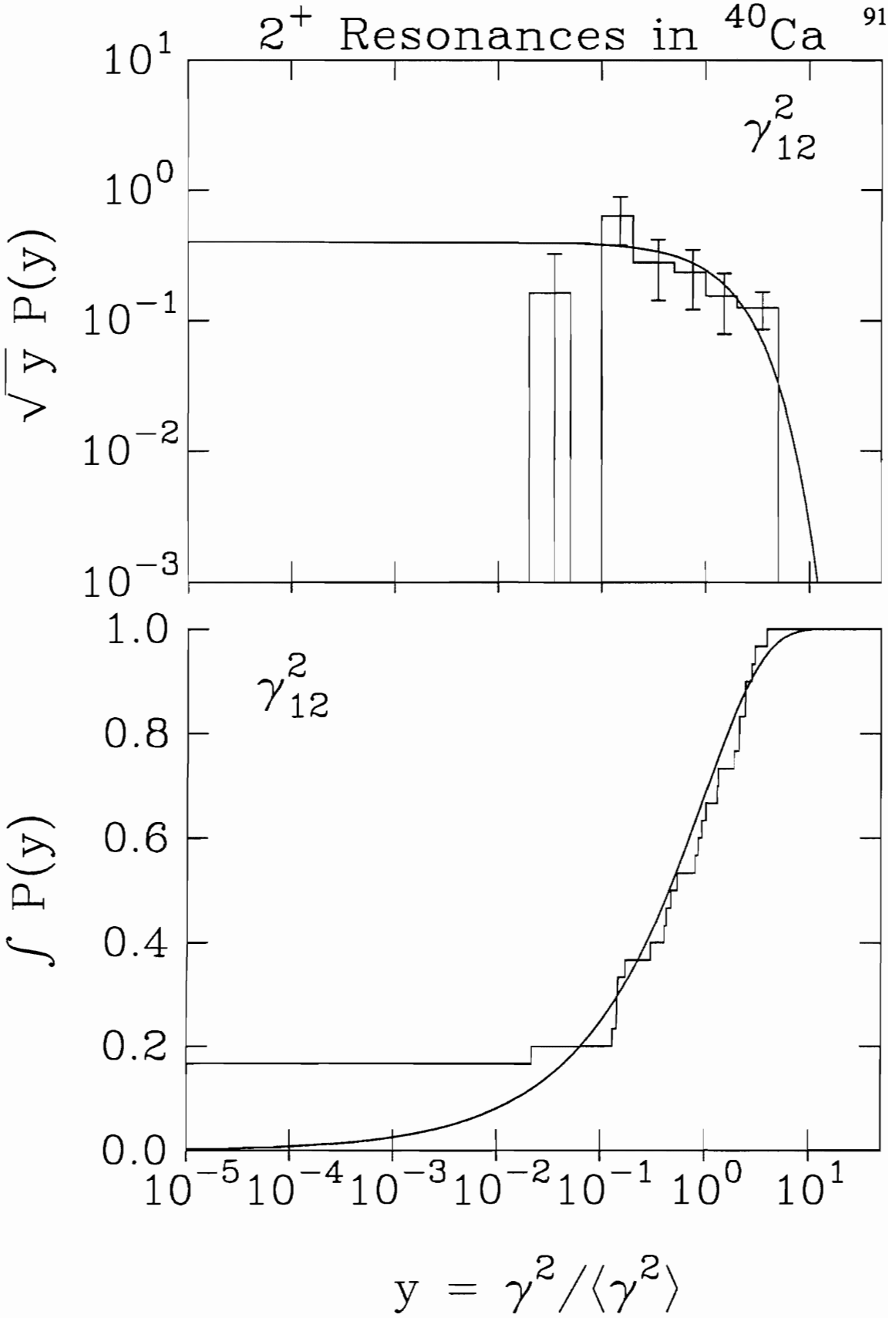
2+ Resonances in 40Ca
γ^2_{12}
$\sqrt{y}\ P(y)$
10^1
10^0
10^{-1}
10^{-2}
10^{-3}
γ^2_{12}
$\int P(y)$
1.0
0.8
0.6
0.4
0.2
0.0
10^{-5} 10^{-4} 10^{-3} 10^{-2} 10^{-1} 10^0 10^1
$y = \gamma^2/\langle\gamma^2\rangle$

Figure 5.4 Distribution of the proton reduced widths in the $s = 2, l = 2$ channel for the 2^+ resonances in ^{40}Ca. The upper figure shows the probability density function, and the lower figure shows the cumulative probability function. The smooth curve is the normalized Porter-Thomas distribution.

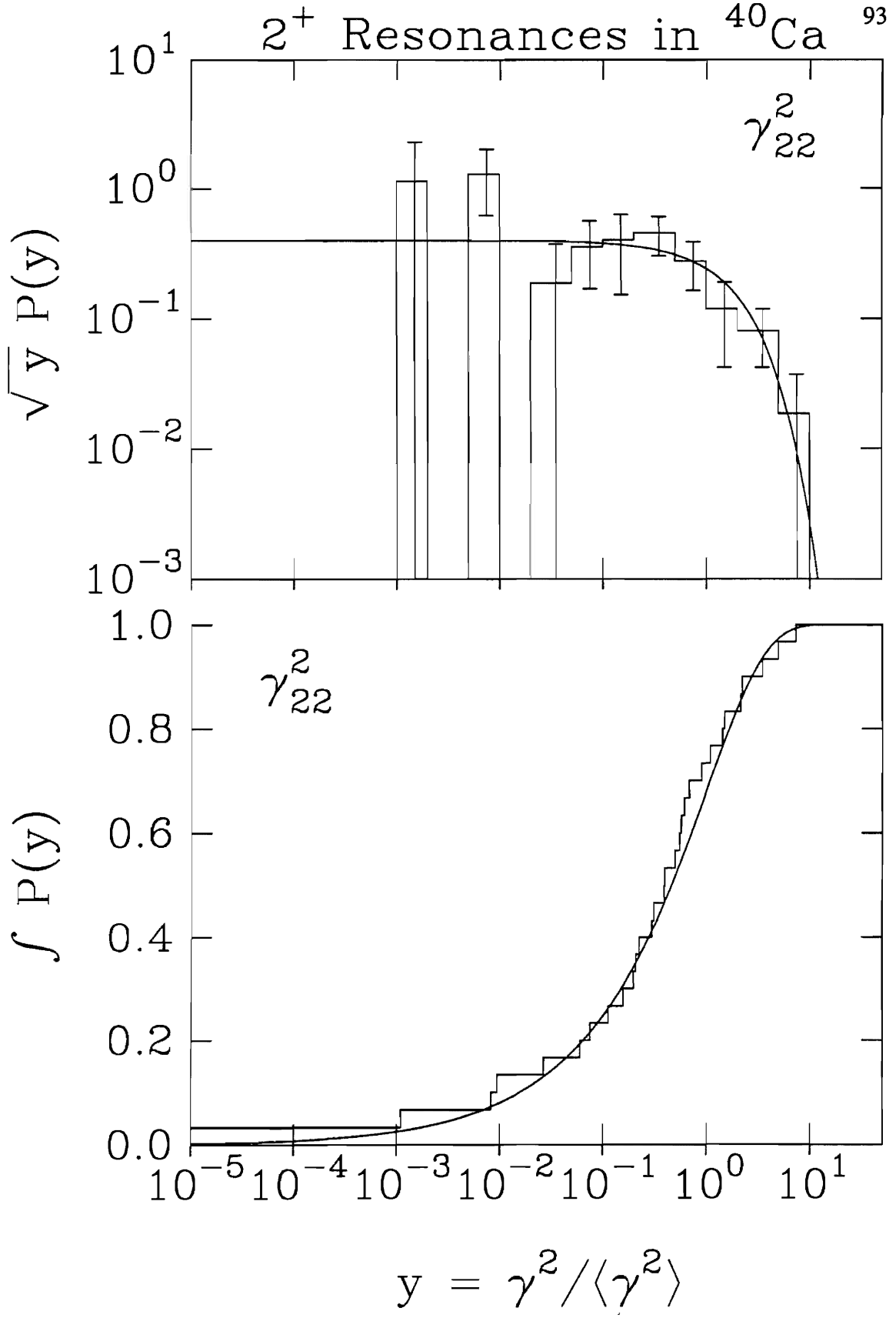
2+ Resonances in 40Ca
γ^2_{22}
$\sqrt{y}\ P(y)$
10^1
10^0
10^{-1}
10^{-2}
10^{-3}
γ^2_{22}
$\int P(y)$
1.0
0.8
0.6
0.4
0.2
0.0
10^{-5} 10^{-4} 10^{-3} 10^{-2} 10^{-1} 10^0 10^1
$y = \gamma^2/\langle\gamma^2\rangle$

Figure 5.5 Distribution of the proton reduced widths in the elastic channel for the 2^+ resonances in ^{40}Ca. The upper figure shows the probability density function, and the lower figure shows the cumulative probability function. The smooth curves are the χ^2 distributions for the one (solid line), two (dotted-dashed line), and three (dashed line) degrees of freedom. The Porter-Thomas distribution corresponds to a χ^2 distribution for one degree of freedom.

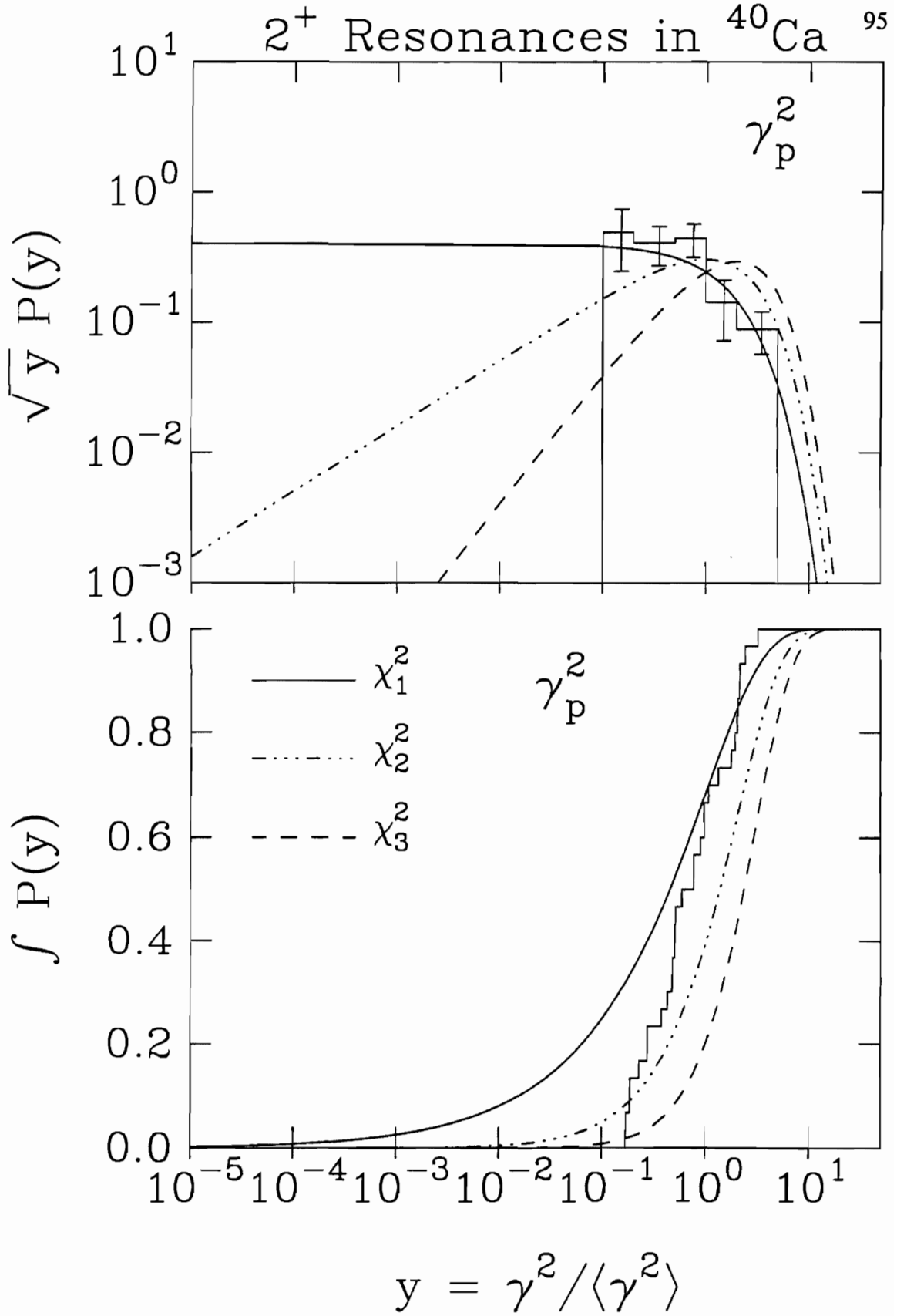
2+ Resonances in 40Ca
γ_p^2
$\sqrt{y}\ P(y)$
10^1
10^0
10^{-1}
10^{-2}
10^{-3}
χ_1^2
χ_2^2
χ_3^2
γ_p^2
$\int P(y)$
1.0
0.8
0.6
0.4
0.2
0.0
10^{-5} 10^{-4} 10^{-3} 10^{-2} 10^{-1} 10^0 10^1
$y = \gamma^2/\langle\gamma^2\rangle$

Figure 5.6 Distribution of the proton reduced widths obtained by averaging the reduced widths in the three elastic channels for the 2^+ resonances in ^{40}Ca The upper figure shows the probability density function, and the lower figure shows the cumulative probability function. The smooth curve is the normalized Porter-Thomas distribution.

Thomas distribution, none of the cumulative probability functions fit the data well. Instead, the cumulative probability indicates that a χ^2 degree of freedom between one and two would be the most appropriate distribution. This plot suggests that the partial widths are correlated.

Another method to combine the proton partial widths utilizes all the widths from the three channels. To form this distribution, the reduced widths for each channel are normalized to the average width of that channel, and then these three sets of widths are combined to form a final width distribution. The result of this procedure is shown in Figure 5.6. For these data, both the probability density and the cumulative probability functions show a good fit to the data.

The linear correlation coefficients, standard deviations, and significance levels for the reduced widths and reduced width amplitudes are listed in Table 5.1. Both the errors and the significance levels were determined by the bootstrap method of Efron (1979). Instead of relying on a analytical model, this method creates a probability distribution from the data themselves, and thus no assumptions are made about the form of the parent distribution. From a set of data with N values, the bootstrap method first generates a new set of data with N values by selecting, at random, data from the original set. Once a data point is selected, it can be chosen again. Therefore, a particular data value may be in a given data set once, more than once, or not at all. From this new set of data, the relevant quantity, such as the linear correlation coefficient, is computed. This process, of creating a new set of data and then calculating the appropriate value, is repeated a large number of times, in this case 25,000 times. The final result is a collection of computed values which form a probability distribution.

The bootstrap distributions for the linear correlation coefficient of the reduced width amplitudes γ_{20} and γ_{22} and the reduced widths γ_{20}^2 and γ_{22}^2 are shown in Figure 5.7. The error is chosen to be half the width of the central 68% of the distribution. The

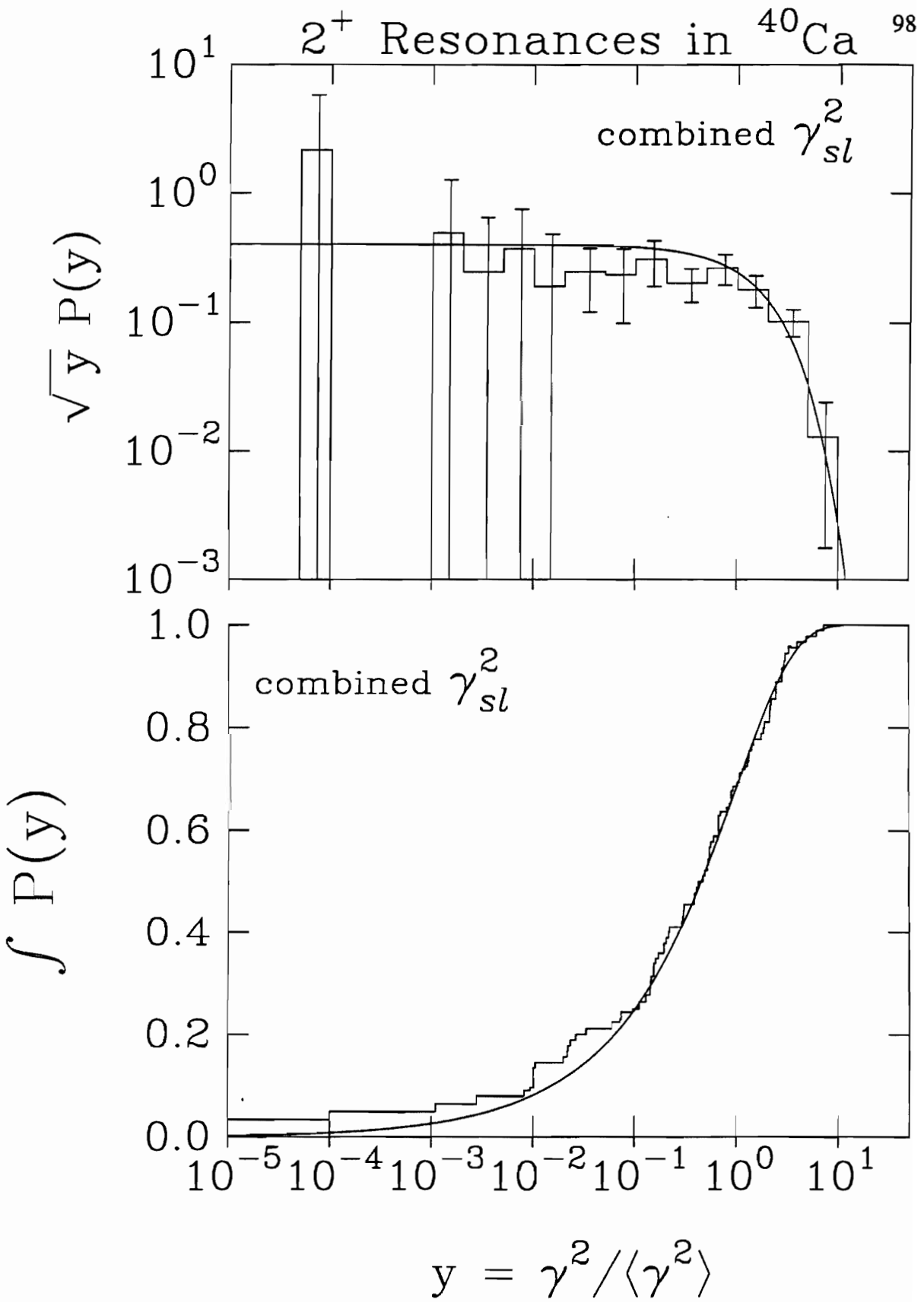
2^+ Resonances in ^{40}Ca
combined γ^2_{sl}
$\sqrt{y}\ P(y)$
10^1
10^0
10^{-1}
10^{-2}
10^{-3}
combined γ^2_{sl}
$\int P(y)$
1.0
0.8
0.6
0.4
0.2
0.0
10^{-5} 10^{-4} 10^{-3} 10^{-2} 10^{-1} 10^0 10^1
$y = \gamma^2/\langle\gamma^2\rangle$

Table 5.1

Linear Correlation Coefficients for 30 2^+ Resonances in ^{40}Ca in the Channel Spin Representation

	ρ	σ	Significance Level
$\gamma_p^2, \gamma_\alpha^2$	0.05	$\pm$ 0.22	58%
$\gamma_p^2, \gamma_{20}^2$	0.35	$\pm$ 0.21	94%
$\gamma_p^2, \gamma_{12}^2$	0.75	$\pm$ 0.06	>99%
$\gamma_p^2, \gamma_{22}^2$	0.71	$\pm$ 0.13	>99%
$\gamma_\alpha^2, \gamma_{20}^2$	-0.04	$\pm$ 0.13	62%
$\gamma_\alpha^2, \gamma_{12}^2$	-0.08	$\pm$ 0.14	70%
$\gamma_\alpha^2, \gamma_{22}^2$	0.15	$\pm$ 0.30	65%
$\gamma_{20}^2, \gamma_{12}^2$	0.05	$\pm$ 0.17	61%
$\gamma_{20}^2, \gamma_{22}^2$	-0.28	$\pm$ 0.08	>99%
$\gamma_{12}^2, \gamma_{22}^2$	0.41	$\pm$ 0.12	>99%
γ_{20}, γ_{22}	0.29	$\pm$ 0.09	>99%

significance level quoted in Table 5.1 is the percentage of the bootstrap distribution which is the same sign as the experimental correlation. Therefore, for a positive correlation, the significance level is the percentage of the bootstrap distribution which is greater than zero. A comparison of the bootstrap with other methods of determining the significance of linear correlation coefficients is discussed by Shriner *et al.* (1987a).

As expected, high correlations exist between all the proton partial reduced widths and γ_p^2. Also, no correlation exists between the alpha reduced widths and any of the proton reduced widths, including γ_p^2. This is consistent with the set of 30 resonances constituting a random collection of widths. All of the partial proton reduced widths show significant correlations between themselves except for the γ_{20}^2 and γ_{12}^2 pair. In addition, the negative width correlation coefficient between γ_{20}^2 and γ_{22}^2 violates the Krieger-Porter theory, while the amplitude pair γ_{20} and γ_{22} has a strong positive correlation. The negative width correlation can be illustrated by a plot of γ_{20} versus γ_{22} and γ_{20}^2 versus γ_{22}^2, shown in Figure 5.8. In both graphs, the data points are distributed along the axes, indicating that the resonances have a tendency to be in either the $s = 2$, $l = 0$ channel or the $s = 2$, $l = 2$ channel. It is this clustering which causes the negative width correlation.

A histogram plot of the amplitude ratio mixing angle ϕ, along with the Krieger-Porter distribution, is shown in Figure 5.9. These data are in poor agreement with the Krieger-Porter distribution. They also indicate the absence of substantial l-mixing in the individual resonances. The plot of the mixing angle ϕ versus E_p is given in Figure 5.10 and shows no apparent energy dependence of ϕ.

While the Krieger-Porter distribution allows for amplitude correlations, it says nothing about their origin. The compound nucleus model does not allow for amplitude correlations, while direct reaction processes require them. In the study of inelastic proton exit channel correlations, large correlation coefficients between channels were also obtained by Mitchell *et al.* (1985). These correlations were attributed to direct reaction

Figure 5.7 Bootstrap probability functions for $\rho(\gamma_{20},\gamma_{22})$ (upper figure) and $\rho(\gamma_{20}^2,\gamma_{22}^2)$ (lower figure) for the 2^+ resonances in ^{40}Ca. The vertical arrow marks the value of the experimental correlation, and the horizontal one indicates the width of the central 68% of the distribution.

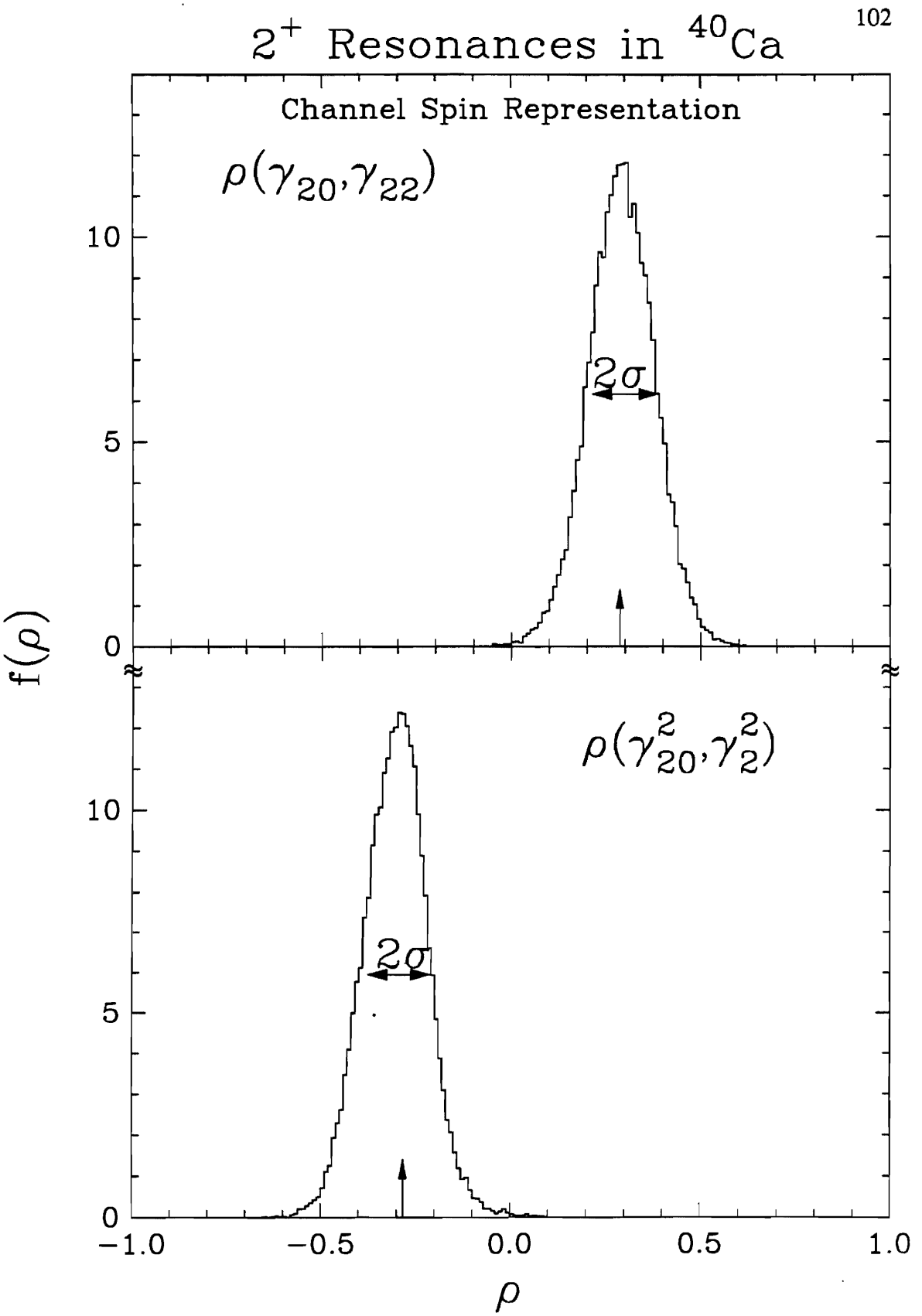
2⁺ Resonances in ⁴⁰Ca
Channel Spin Representation
ρ(γ20,γ22)
2σ
ρ(γ²20,γ²2)
2σ
f(ρ)
10
5
0
10
5
0
−1.0
−0.5
0.0
0.5
1.0
ρ

Figure 5.8 Plot of the reduced widths γ_{20}^2 versus γ_{22}^2 (left), and the reduced width amplitudes γ_{20} versus γ_{22} (right) for the 2^+ resonances in ^{40}Ca.

2^+ Resonances in ^{40}Ca

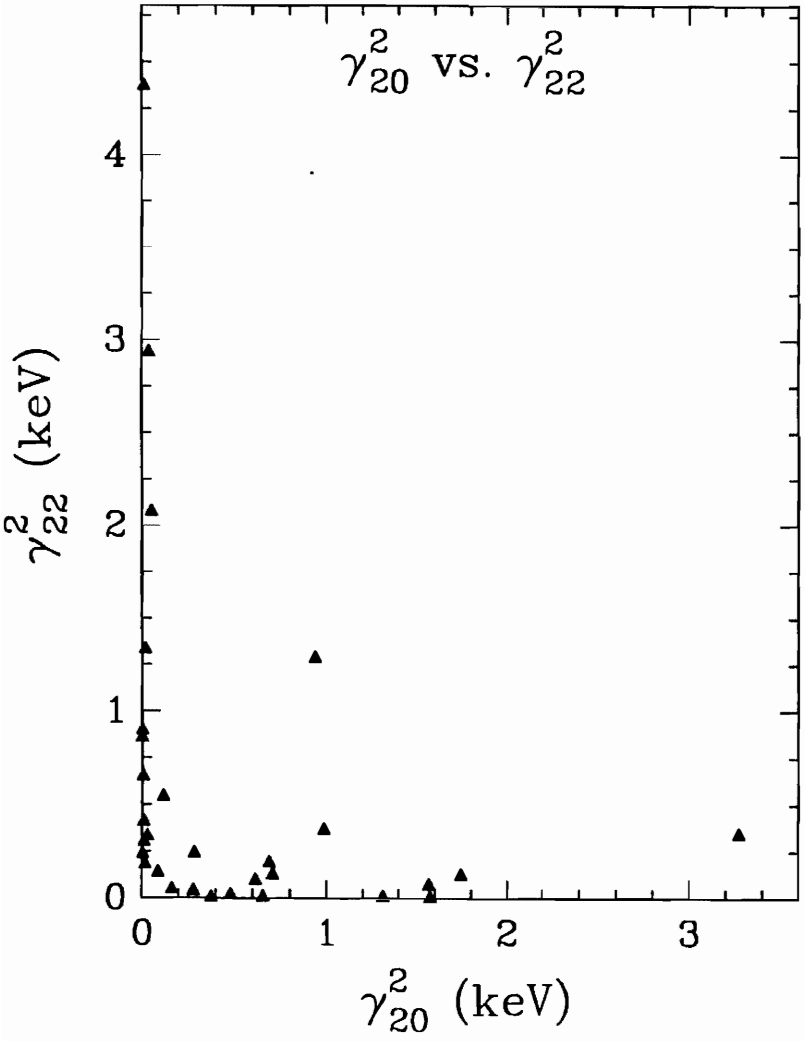

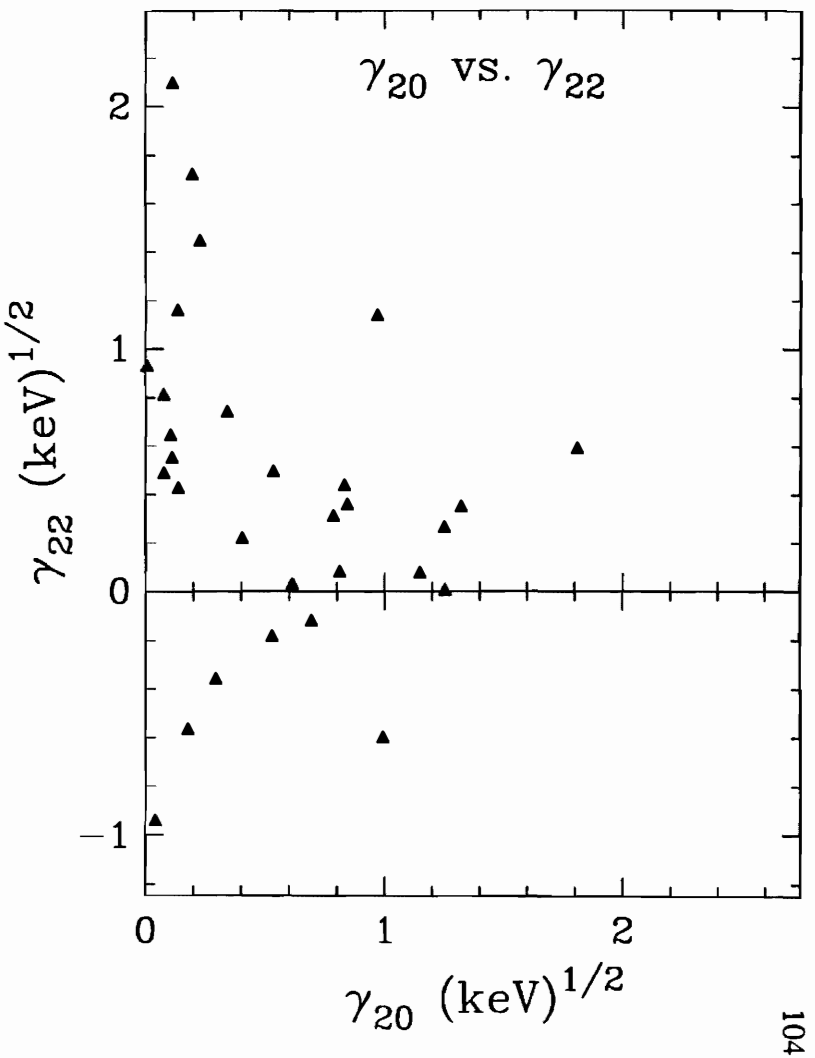

Figure 5.9 Distribution of the mixing angle ϕ for the 2^+ resonances in ^{40}Ca. The smooth curve is the Krieger-Porter distribution.

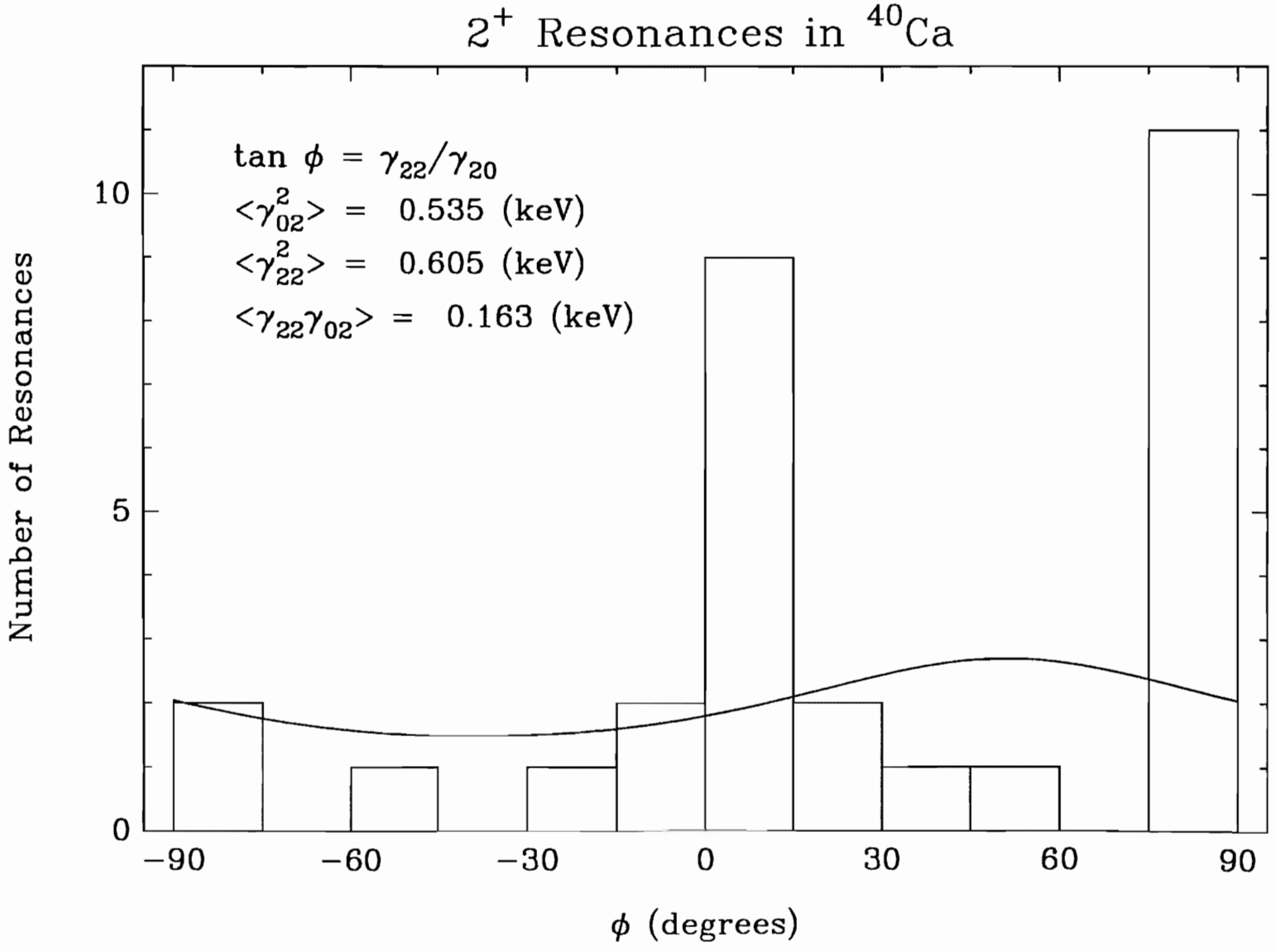
2+ Resonances in 40Ca
tan φ = γ22/γ20
<γ02²> = 0.535 (keV)
<γ22²> = 0.605 (keV)
<γ22γ02> = 0.163 (keV)
Number of Resonances
0
5
10
−90
−60
−30
0
30
60
90
φ (degrees)

Figure 5.10 Energy dependence of the mixing angle ϕ for the 2^+ resonances in ^{40}Ca.

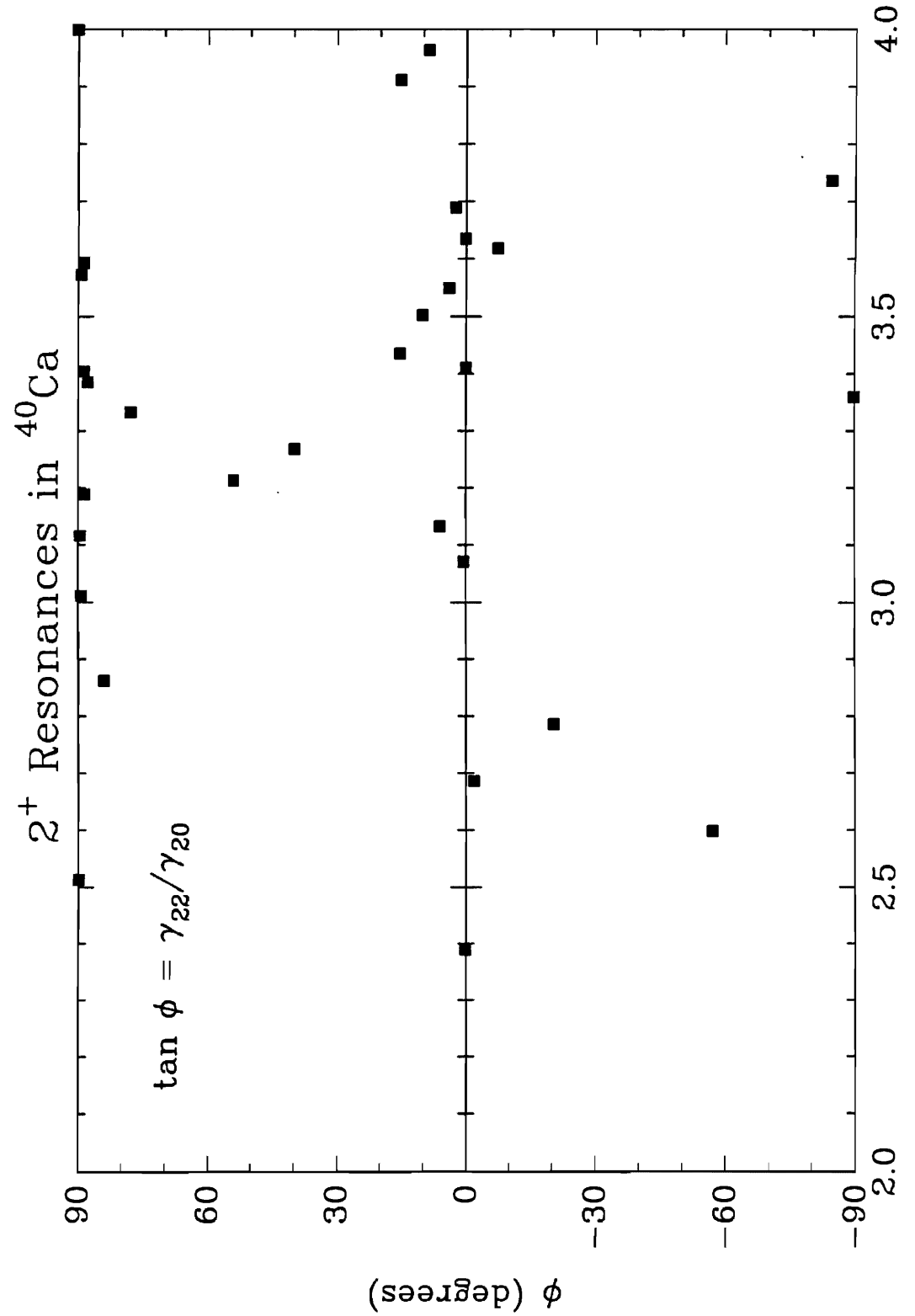
2^+ Resonances in ^{40}Ca
tan $\phi = \gamma_{22}/\gamma_{20}$
ϕ (degrees)
90
60
30
0
−30
−60
−90
2.0
2.5
3.0
3.5
4.0
E_p (MeV)

processes in the nucleus.

C. The Zero Representation

It has been demonstrated that the relationship between $\rho(\gamma_{20},\gamma_{22})$ and $\rho(\gamma_{20}^2,\gamma_{22}^2)$, predicted by the Krieger-Porter theory, does not appear to hold in the channel spin representation. However, the correlation coefficients have different values in other coupling schemes. Shriner *et al.* (1987b) recommend the use of the zero representation, the representation in which the reduced width amplitude correlation is zero, for the comparison of the linear correlation coefficients.

To convert from one representation to another, the reduced width amplitudes are modified by an orthogonal transformation. The general transformation for a three channel case is described by a 3×3 matrix whose elements are defined in terms of the Euler angles $\alpha\beta\gamma$. For the resonances in this experiment, only one pair of amplitudes were determined, and consequently, only two channels need to be mixed. The transformation matrix can then be written in terms of one transformation angle θ as

$$\begin{pmatrix}\gamma_a\\ \gamma_b\\ \gamma_c\end{pmatrix}=\begin{pmatrix}\cos\theta & \sin\theta & 0\\ -\sin\theta & \cos\theta & 0\\ 0 & 0 & 1\end{pmatrix}\begin{pmatrix}\gamma_{20}\\ \gamma_{22}\\ \gamma_{12}\end{pmatrix}. \qquad (5.13)$$

Since only the relative signs of the reduced width amplitudes γ_a and γ_b are known, θ can be restricted to $\pm 90°$. Once the amplitudes are transformed and the widths calculated, $\rho(\gamma_a,\gamma_b)$ and $\rho(\gamma_a^2,\gamma_b^2)$ can be computed.

A plot of the reduced width and amplitude correlation coefficients as a function of the transformation angle is shown in Figure 5.11. This graph shows that for the two values of θ at which $\rho(\gamma_a,\gamma_b)$ is zero, the values of $\rho(\gamma_a^2,\gamma_b^2)$ are also identical. Table 5.2 summarizes the linear correlation coefficients results in the zero representation, and the

bootstrap distributions are shown in Figure 5.12. Again, the widths have a large correlation coefficient, in disagreement with the Krieger-Porter theory.

Figure 5.11 $\rho(\gamma_a,\gamma_b)$ and $\rho(\gamma_a^2,\gamma_b^2)$ as a function of the transformation angle θ. The transformation is given by Eqn. 5.13, where $\theta = 0°$ corresponds to the channel spin representation.

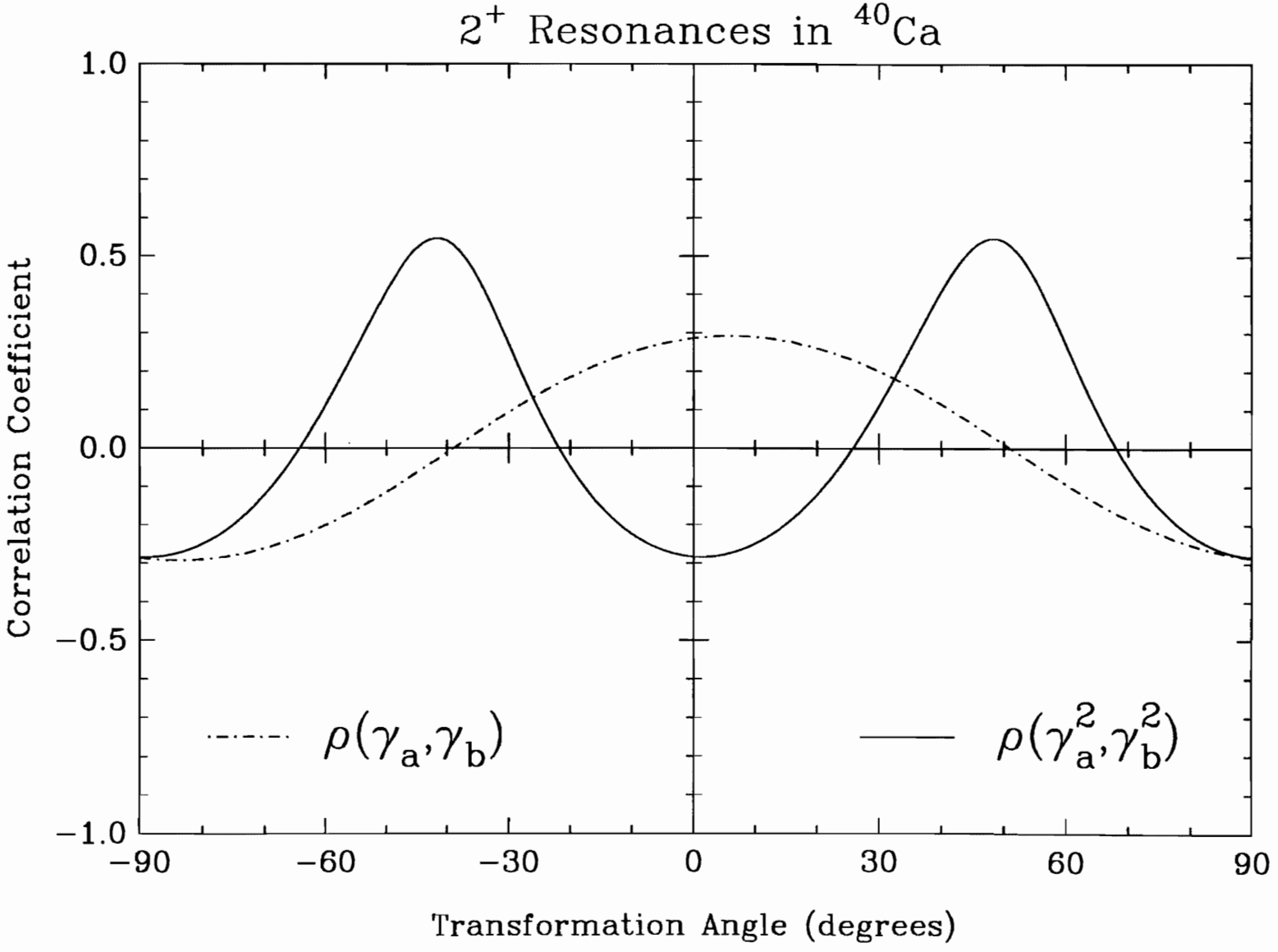
2+ Resonances in 40Ca
1.0
0.5
0.0
−0.5
−1.0
Correlation Coefficient
ρ(γa,γb)
ρ(γa2,γb2)
−90
−60
−30
0
30
60
90
Transformation Angle (degrees)

Table 5.2

Linear Correlation Coefficients for 30 2^+ Resonances in ^{40}Ca

in the Zero Representation

Transformation Angles -39°, 51°

	ρ	σ	Significance Level
γ_a, γ_b	0.00	$\pm$ 0.23	50%
γ_a^2, γ_b^2	0.53	$\pm$ 0.24	97%

Figure 5.12 Bootstrap probability functions for $\rho(\gamma_a,\gamma_b)$ (upper figure) and $\rho(\gamma_a^2,\gamma_b^2)$ (lower figure) in the zero representation. The vertical arrow marks the value of the experimental correlation, and the horizontal arrow indicates the width of the central 68% of the distribution.

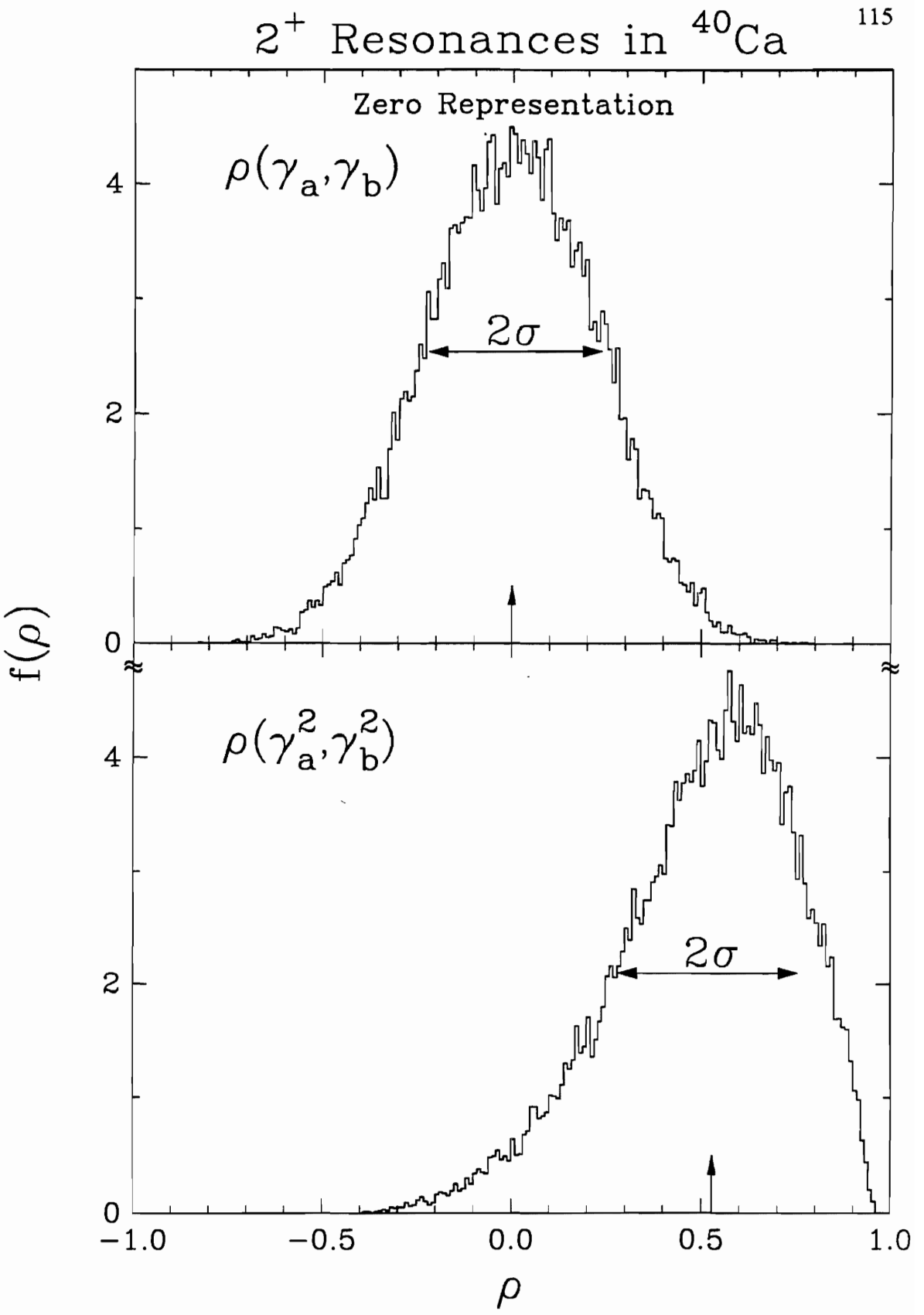
2+ Resonances in 40Ca
Zero Representation
ρ(γa,γb)
2σ
ρ(γa2,γb2)
2σ
f(ρ)
ρ
0
2
4
−1.0
−0.5
0.0
0.5
1.0

CHAPTER VI

SUMMARY

Angular distributions and excitation functions of the $^{39}K(p,\alpha_0)^{36}Ar$ reaction were measured for 68 resonances in the proton energy range 2.2 MeV to 4.0 MeV. Of these resonances, 21 were identified as 1^- states and 39 were assigned a J^π value of 2^+.

The angular correlations were discussed, and the angular distribution equations for the (p,α_0) reaction on a spin and parity $3/2^+$ target were presented for $J = 1$ to $J = 4$. The correlation equations for $J^\pi = 1^-$ and $J^\pi = 2^+$ resonances were discussed in detail. The R-matrix analysis of the reaction cross sections was outlined.

For the 2^+ resonances, the (p,α_0) angular distribution provides two possible solutions for the mixing parameters. Comparison of the two solutions with results from the elastic scattering data removes the ambiguity, and three sets of reduced widths and one pair of reduced width amplitudes were obtained for 30 2^+ resonances. For the 1^- resonances, the angular correlation equation provides only a relation between the mixing parameters. Of the 1^- resonances, the elastic scattering data reduced the number of solutions to two for 11 resonances while providing unique solutions for only 2 resonances.

Statistical analyses were performed on the 2^+ widths. These data are the first results on entrance channel width and amplitude correlations. The proton partial reduced widths agreed well with the Porter-Thomas distribution. However, the amplitude mixing angle distribution is in poor agreement with the Krieger-Porter distribution. The resonances show little l-mixing between the $s = 2$, $l = 0$ channel and the $s = 2$, $l = 2$ channel.

Strong width correlations were observed between two of the three proton channels. A negative width correlation was found between the γ_{20}^2 and γ_{22}^2 widths, which violates the Krieger-Porter theory. The reduced width amplitude pair γ_{20} and γ_{22} also had a high correlation coefficient. These amplitudes and widths were transformed to the zero representation, where again a high width correlation was obtained. These high correlation coefficients are indicative of direct reaction processes. Further study of entrance channel correlations are needed to determine whether these high correlation values are the exception or the norm for nuclei in this mass and energy range.

APPENDIX A

HIGH RESOLUTION LABORATORY DATA ACQUISITION SOFTWARE

The XSYS data acquisition and analysis system for VAX computers is used at TUNL. It was developed at TUNL in the early 1980s and was designed as a general software package adaptable for use with a variety of nuclear physics experiments. Since then, several other nuclear laboratories have used and adopted XSYS as their data acquisition system. At the High Resolution Laboratory (HRL), typical experiments involve several thousand data runs, lasting from one to two minutes each. After every data run is completed, a series of procedures are performed before the experiment is resumed. This specialization of the experimental procedures has lead to the modification of several XSYS programs. Although many people in the past several years have worked on the adaptation of XSYS for HRL, John Shriner, Ron Nelson, and Barry Warthen have been the main contributors. The purpose of this appendix is to acquaint the reader with the data acquisition programs and procedures developed for HRL. For a overview of XSYS, refer to the latest edition of the XSYS reference manual (Soderstrum, 1987).

Before beginning an experiment, the data acquisition system must first be initialized. The command file HIRES contains all the commands necessary to setup the data acquisition system and start the data accumulation. This command procedure first clears all the XSYS flags and deallocates the old data areas before setting up the new data areas. A data area are a one or two dimensional array, accessible by any XSYS program, in which data is stored. A data area can contain either real or integer data, and is

variable in length. At HRL, only one dimensional data areas are used, and the number assigned to them specify their function. Data areas 1 - 9 are reserved for the detector spectra and the yield curves of the reactions are contained in data areas 11 - 99. For the yield data areas, the first digit of the data area number refers to the number of the window which is used to calculate the yield while the second digit indicates the spectrum. For example, data area 23 contains the yield curve summed from the second window of detector #3. Data areas 100 to 700 are used for any extra spectra that are to be written to tape. These are spectra such as coincidence spectra for which no windows will be set. The rest of the data areas store various values used by the data acquisition programs. Table A.1 lists all the data areas and their contents.

Next, HIRES defines 19 gates for each spectrum data area. These also have specific uses. Gates, or windows, 1 - 9 are set on the individual reaction peaks. The spectrum counts inside these windows are summed to determine the yield. The window number corresponds to the reaction number assigned when the reaction kinematic parameters are entered. Gates 11 - 19 are used to identify the calibration peaks. The use of these gates will be discussed later. Gate 10 can be used to obtain the energy of one or two channels of a calibrated spectrum. This method to obtain the spectrum channel energies has become obsolete since the calibration program used at HRL has been interfaced with the regular XSYS calibration program. Spectrum energies can be obtained from either the XSYS ENERGY command or the graphics display program DISP.

Once the data areas and gates have been defined, information specific to the experiment is requested. Before exiting, HIRES run the program ANGL. This program asks for the number of detectors and the value of the detector angles. It also asks whether the windows of a spectrum are to be shifted as the energy of the beam changes. For charged particle spectra, the energy of the reaction peaks increase as the proton beam energy is increased. However, the peaks of γ-ray spectra are often independent of the

Table A.1

List of Data Areas and Their Contents

Data Area	Channel Number	Contents
901	1-4096	large data area used to sort the data
1	1-512	detector spectrum; equivalenced over channels 512-1023 of data area 901
2	1-512	detector spectrum; equivalenced over channels 1024-1535 of data area 901
3	1-512	detector spectrum; equivalenced over channels 1536-2047 of data area 901
4	1-512	detector spectrum; equivalenced over channels 2048-2559 of data area 901
5	1-512	detector spectrum; equivalenced over channels 2560-3071 of data area 901
6	1-512	detector spectrum; equivalenced over channels 3072-3583 of data area 901
7	1-512	detector spectrum; equivalenced over channels 3584-4095 of data area 901
8-9	1-512	detector spectra
11-99	1-2000	yield curves; data area *jk* is the yield calculated from window *j* of detector spectrum *k*
10	1-2000	yield curve run numbers
20	1-2000	yield curve beam energies in MeV
30	1-2000	elapsed time (in seconds) since the first data run was completed for each yield point
100-799	1-512	extra spectra

Table A.1 - continued

Data Area	Channel Number	Contents
800	1-9	detector angle (in degrees) of spectra 1 - 9
	10	number of detectors
	11	beam energy in MeV
	12	energy step size in eV
	13	number of extra spectra
	21-29	flag to indicate whether or not the spectra windows are to be shifted
801	1-40	masses and Q-values of calibration reactions
	41	number of calibration reactions
802	1-40	masses and Q-values of reactions for windows
	41	number of windows per spectrum
803	1-486	window parameters; 6 for each window
	487	yield curve channel index
804	1-18	spectra calibration values; keV/channel, keV for each spectra
805	1-81	latest yield curve sums for XBOXSP to access
806	1-9	detector normalization factors
807	1-9	dead time factor for each spectrum
	10	time (in seconds) the last data run was completed
850	1-5	process id numbers for master subprocesses
	6-25	names of master subprocesses
	26	number of master subprocesses
	27	pointer to active master subprocess

Table A.1 - continued

Data Area	Channel Number	Contents
947		several parameters saved to tape
	1-20	title of experiment
	21	run number
	22	beam energy in eV
	23	beam energy step size in eV
	24	preset value
	30-53	scaler values
	54-101	scaler headers
	103-110	dead time factors
	120-122	date
	123-125	time
	128	tape record length in bytes

beam energy. The windows of each individual spectra can be set to shift or not.

The next task to be performed before the experiment can begin is the spectra calibration. This procedure is begun with the command MQ CAL. This program first asks for the number of reaction peaks to be used in the calibration of the spectra. At least two reactions are needed to calibrate the spectra. MQ CAL then asks for the kinematic parameters for each calibration reaction. These parameters include the mass (in amu) of all the of particles in the reaction and the *Q*-value. To enter an elastic proton reaction, only the mass of the target is needed; MQ CAL will supply the mass of the proton. Once the calibration reactions have been entered, the appropriate peaks of the spectra associated with the calibration reactions must be indicated. Using the program DISP, windows are manually set on the calibration peaks for each spectrum. Gate 11 should be set around the first calibration reaction specified, gate 12 around the next, etc. These windows do not need to be set carefully, since the maximum point inside the marked window is used as the reaction peak.

Once the calibration windows are set, the command CALIB will calibrate the spectra by performing a linear fit between the spectrum channel numbers and the calibration reaction energies. Two calibration peaks are usually sufficient to obtain a reliable calibration. The most common reactions used are the $^{16}O(p,p)$ and the elastic scattering reaction from the highest Z element on the target. If a reaction which emits a higher energy particle exists, such as a (p,α) reaction, it is useful to include this reaction for a third calibration point. This does not mean that the proton beam must be on resonance to calibrate the spectra. When the program MQ CAL is executed, the number of calibration reactions can be given as two. Then, once the proton beam is on resonance and reaction peak reappears in the spectra, MQ CAL can be run again to include the third reaction. Once the kinematic parameters for the third reaction have been entered, they will be saved, even if the number of the calibration reactions is reduced back to

two.

Next, the windows for the yield calculations must be defined. This time, the command MQ WIN is used to enter the reactions whose yields are to be studied. The kinematic parameters are entered in the same manner as the calibration reaction parameters were for the command MQ CAL. The windows are then manipulated by the program WINDow. Each window of a spectrum is defined by six parameters. These parameters are illustrated in Figure A.1. The first parameters, labeled *winlo* and *winhi*, define the range of the spectra to be used to calculate the yield. The value of these parameters is the number of channels away from the channel at which the resonance peak has been calculated to appear (the dashed line of Figure A.1). Their limits can be viewed by using the 'D' command of DISP. The next two window parameters, *bklo* and *bkhi*, help define the range to be used as the spectrum background. Their values are measured from the *winlo* and *winhi* values. The last two window parameters are called *bkwlo* and *bkwhi*. These values indicate the number of channels of the spectrum to be used to calculate the background subtraction. If both *bkwlo* and *bkwhi* are zero, no background subtraction will be computed. If *bkwlo* + *bkwhi* = 1 or 2, then the average of the channels is subtracted as the background. Otherwise, a least squares fit to the background points is performed in order to compute the linear background to be subtracted from the window sum.

There are four options to the WINDow program. WIND INIT initializes the six window parameters to the values given in the command line. If no parameters are listed, the default values of the window parameters are used. The option WIND CHAN allows specific adjustments to be made to the window parameters. First, this option lists the current window parameters, followed by a command line to enter changes. For either the angle or window number, the character '*' may be used as a wildcard character. WIND SET allows the first two parameters *winlo* and *winhi* to be set by arranging the

Figure A.1 A portion of a spectrum illustrating the window placement. The dashed line in the center represents the channel of the reaction. *Winlo* and *winhi* define the limits of the gate. The value of both of these parameters is 4, as measured from the reaction channel. The background region of the spectrum is defined by *bklo*, *bkhi*, *bkwlo*, and *bkwhi*. Their values are 1, 1, 3, and 3, respectfully. In this example, the sum of channels 325 - 333 is used to calculate the yield. The background is computed from a linear fit to channels 321 - 324 and 334 - 337 and subtracted from the yield sum to obtain the final value of the yield.

Window Parameters

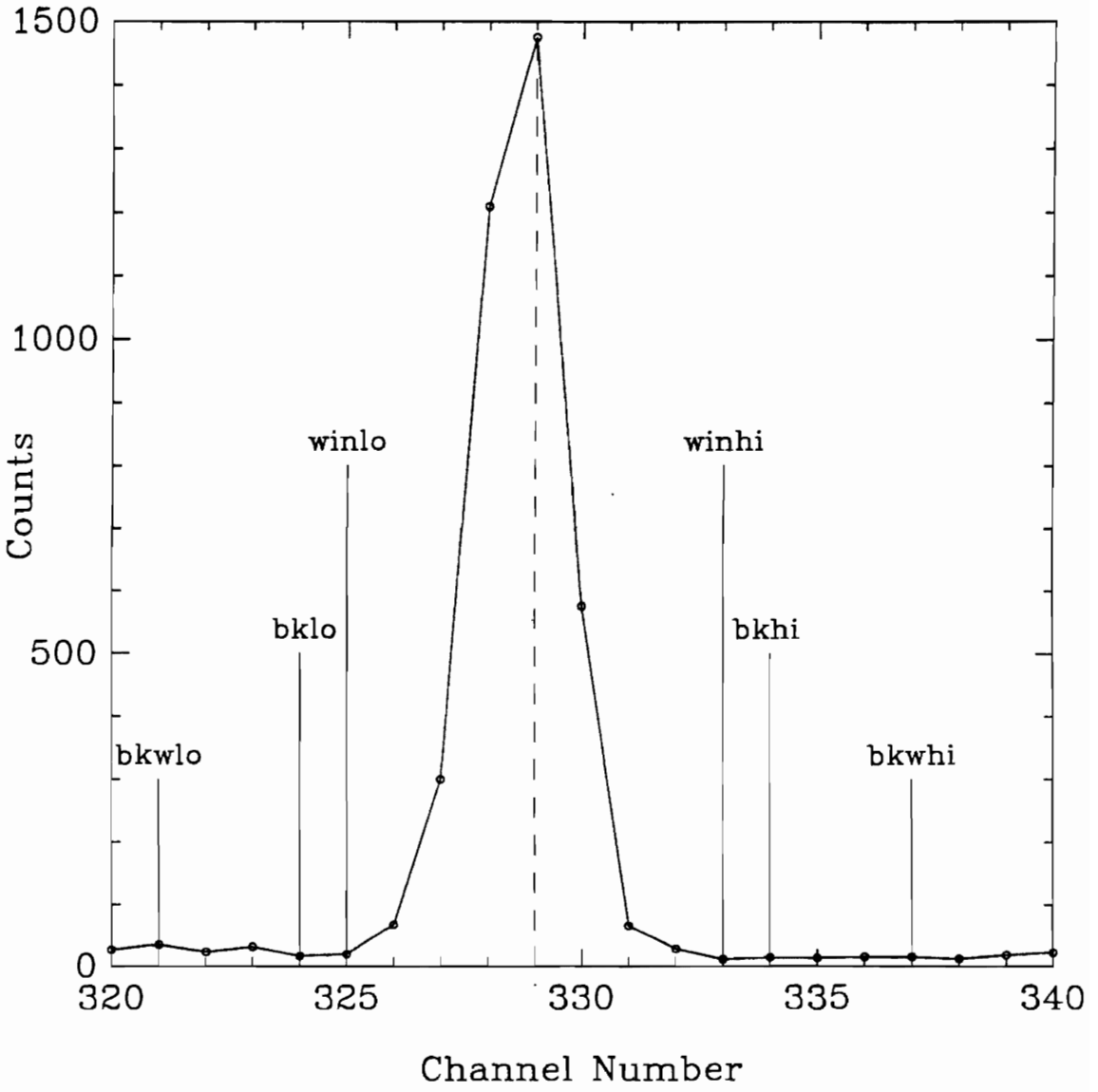

gates in the DISP program. Once the gates have been adjusted, WIND SET changes the window parameters to those set in the DISP program. Finally, WIND SHIFt transforms the windows to the current window parameters based on the beam energy.

It is recommended that after all the data areas have been allocated and the spectra calibrated, the data areas and their setups be saved using the XSYS SAVE and WRT commands. Therefore, in case of an accidental removal of one or more data areas, the data area configuration and their contents can easily be restored. This is also useful for setting up the data areas for offline analysis or for later runs of the same experiment. In these cases HIRES need not be run, nor will it be necessary to reenter the angle, window, and calibration information.

One other command procedure to be executed if the spectra are to be stored on tape is TAPE. This is a command file which allocates the tape drive and mounts the tape. It asks for the number of spectra to be stored and then asks whether or not a new tape is used. For a new tape, an end of tape mark is written and anything else on the tape will be lost.

HIRES also executes another command procedure, HIRESON. This is a separate routine because, if all the data areas are already allocated, then only HIRESON needs to be executed to commence data acquisition. First, this routine allocates the VAX port TTA4:. This line is used to communicate the desired beam energy to the PDP microprocessor which controls the voltage on the analyzer plates. Before the beam is tuned into the electrostatic analyzer, the experimenter should have the analyzer plates set to the correct voltage. The PDP microprocessor is used to control the analyzer plate voltage. Initially, the experimenter must connect the computer terminal in the laboratory to the PDP by flipping the switch on the terminal port box located beneath the NIM modules. The experimenter then executes the command file SETUP on the PDP. This file first

zeros the DACs which control the plate voltage so that the voltage power supplies may be turned on. Next, the Fluke digital voltmeter used to measure the plate voltages is initialized. Finally, the program CONTRL is run. This program regulates the analyzer plate voltage such that beam with the desired energy can be steered through the analyzer. Once the analyzer plates are at voltage, the terminal should be switched back to the VAX. This also connects the PDP to the VAX, enabling the VAX to communicate with the PDP.

Next, HIRESON allocates and downloads the microprogrammable branch driver (MBD) before the data acquisition subprocesses are created. Typically, four subprocesses in addition to the experimenter's process are used by the VAX for data acquisition. A block diagram of these processes is shown in Figure A.2. The first subprocess is called XSORT. This process sorts the data from the ADC buffers and distributes them into the appropriate data areas. At HRL, two ADCs are available for use, and different XSORT subprocesses are used with each ADC. The ADC most commonly used is connected to the Multiplexer, which allows the ADC to digitize signals from up to seven detectors. The instructions to XSORT on handling a data pulse from this ADC are contained in the files BUFF.DAP and BUFF.EVL. (See the XSYS manual about *.DAP and *.EVL files.) This XSORT routine writes all of the spectra into the large data area 901. Data area 901 is divided into 7 sections of 512 channels each, representing the 7 different detector spectra. The individual spectra data areas 1-7 are equivalenced over the sections of data area 901. The ADC converts the pulse originating from a detector into a 9-bit binary word representing the channel number. The 3-bit code indicating the detector from which the signal originated is added as the most significant bits to the 9-bit word to form a 12-bit word representing a channel in data area 901. This method allows the data to sort themselves, and thus reduces the time required to process the data.

Figure A.2 Block diagram of the data acquisition processes.

HRL Data Acquisition Processes

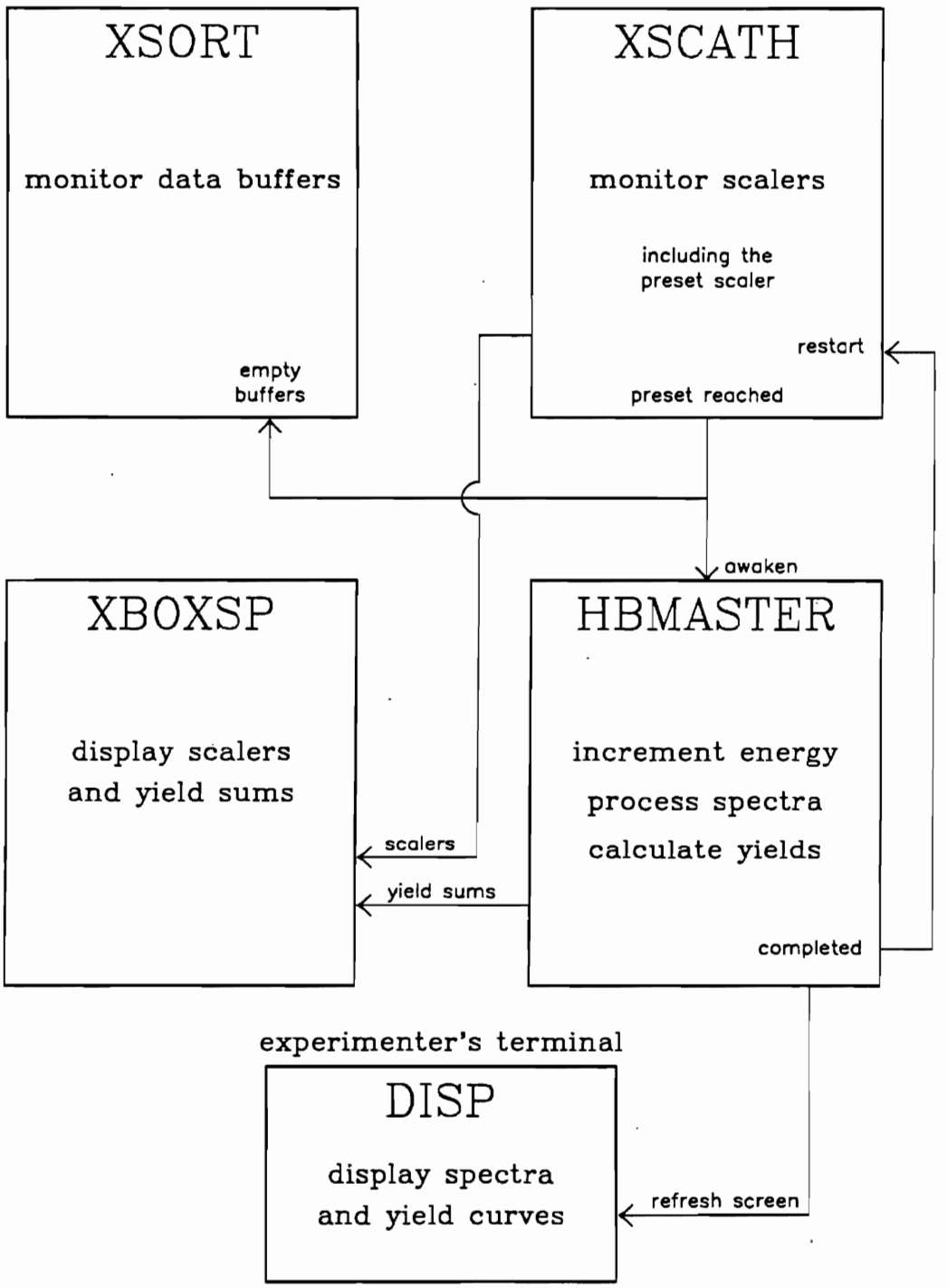

The two other XSORT routines are used with the stand-alone ADC. Only the signals from one detector can be digitized by this ADC. The instructions for this XSORT subprocess are contained in the files ADC.DAP and ADC.EVL. The other XSORT routine sorts the pulses into a 8192 channel spectrum instead of the usual 512 channels. These instructions are contained in the files AD8K.DAP and AD8K.EVL. This XSORT subprocess is used for high resolution γ-ray detectors.

XSCAT is the second data acquisition subprocess. This subprocess monitors the CAMAC scaler modules and administers the scaler information on the VAX. The usual scaler configuration for HRL experiments includes the preset scaler, a scaler connected to a timer, a spare, and one scaler for each of the detectors. The preset scaler is the scaler which signifies the end of the data run. It is connected to the current integrator, which measures the amount of beam charge deposited on the Faraday cup. When this scaler reaches a predetermined value, XSCAT ends the data run by first inhibiting the CAMAC crate so that no more data will be collected. XSCAT then signals XSORT to process the data that is still stored in the buffer, and notifies the VAX that the run has completed.

At the end of a data run, several functions need to be performed to process the spectra and to prepare for the collection of the next set of spectra. First, the energy of the proton beam is increased by instructing the PDP to increment the analyzer plate voltage. Next, the spectra, scalers, and other information are written on tape to be extracted during the offline analysis. After that, all the windows are checked to see if the beam energy requires that the windows be adjusted. The yield sums are then calculated and stored in the appropriate data areas along with the beam energy, run number, and elapsed time of the data run. Finally, all the spectra and scalers are cleared and the data acquisition is restarted.

In the regular XSCAT subprocess, when preset is reached, a new process is created which executes a command file containing calls to the individual programs to pro-

cess the data. A significant amount of time was used for this procedure and steps were taken to reduce this time interval. First, all the individual programs were combined into one large program, which shortened the processing time to around 10 seconds, but still long compared with 60 to 90 seconds required for each data run. It was determined that the major portion of this time interval was spent in creating the new process.

This problem was corrected by writing a new version of XSCAT, called XSCATH, which awakens an existing process from a hibernate state when the preset is reached. This process then performs the necessary procedures to process the data and start the next run before returning to a hibernate state. This process, called the master subprocess, is the third subprocess required for data acquisition.

The command SUBPRO controls the master subprocesses. Currently, up to five master subprocesses can be loaded into the computer at once. SUBPRO is used to create and delete the master subprocesses, as well as to indicate which process is to be awakened when the run is over. If no master subprocess has been created, XSCATH then behaves like the XSCAT and executes the command procedure MASTER.COM at the end of the run. The use of master subprocesses has reduced the time between runs to 3 seconds, saving over 8 hours for a typical experiment of 5000 data runs. The limiting factor between runs now is the time required to change the voltage on the analyzer plates.

Presently, there are two master programs written. HBMASTER is the routine usually used for data acquisition. It performs all the functions described above, plus it writes to the file SBORN.LIS the energy, run number, and which windows have been shifted for each run. The other master program used is TARGETER. It is used primarily for target testing. It only sums the yields and clears the spectra before restarting the data acquisition. For both of the subprocesses, if an error occurs during their execution, the experimenter's terminal will be notified, and the error message will be written to the file *.ERROUT. If the error causes the subprocess to delete itself, i.e. the tape is not

loaded into the tape drive when HBMASTER tries to write the spectra to tape, the sub-process has to be recreated with SUBPRO.

The final subprocess created for data acquisition is XBOXSP. This program controls the box display next to the experimenter's terminal, which shows the pertinent information about the experiment. This includes the current proton energy, run number, values of the scalers, yield sums, and dead time factors.

To observe the spectra and yield curves, the XSYS graphics display program DISP is used. It is run on the experimenter's terminal to graph the data areas. A slightly modified version of this program is used at HRL which enables the master subprocess to automatically refresh the screen after the new yields have been calculated. Just before HBMASTER returns to a hibernate state, it sets a common event flag. When DISP is waiting for a command to be entered from the keyboard, it is also checking to see if that event flag has been set. If it has, DISP then executes the 'P' command for the data area currently displayed on the screen.

For hardcopy plots of the data, three programs exist. The DISP program allows the experimenter to obtain a hard copy plot of the present screen display. This plot can be directed to three different devices: the laser printer, the HP plotter, or the dot matrix printer. SPECTPLOT is a program which produces a line plot of a data area on the HP plotter. For both of these plots, the x-axis is the data area channel number. The third program is YCPLOT, which plots the yield versus beam energy on the HP plotter. This is useful for comparing resonances which have been measured more than once. Also YCPLOT writes the run numbers and energies of each yield section at the top of the plot.

Several programs have also been written for use during offline analysis. The main goal in the offline analysis is to recreate the yield curves from the spectra stored on tape, but with greater attention paid to the window placement. The data areas are set up

exactly as they were during the experiment, and the same procedure is used to calibrate the spectra as before. XREAD is the program which reads the data from the tape and into the data areas. If a number follows the command XREAD, the data run associated with that run number will be read. Otherwise, the next run is read into the data areas. STRIP is the offline version of the master subprocess. This program is used to read the spectra, shift the windows, and calculate the yields several runs at a time. A number following the STRIP command indicates the number of data runs the program is to read and process. RWND # will rewind the data tape for # runs. If no number is given, the tape is rewound one run. Once the yields are completed, it is then necessary to extract the yield values into a file which can then be used by MULTI or any other program. The program used to do this is YCLIST. It asks for the number of angles and reactions and then creates a file listing the energy and yield by angle and reaction in the form ready for use by MULTI.

In addition to the programs described here, several other routines have been written to aid in the data acquisition. These are listed in Table A.2. At the beginning of each program is an explanation and instructions on its use.

Table A.2

List of HRL Data Acquisition Programs

Command	Options	Description
ANGL		reads in the angle for each detector
	list	lists all angles
CALIB		calibrates spectra
	en	returns the spectrum energy for the channels marked by gate 10
	print	writes output to file FOR100.DAT
CURSDAT		writes run numbers, beam energies, and yields found in data area N1 into a file. The range of points is given by the cursor.
DT		calculates detector dead time factors
	list	prints the dead time factors to the terminal
EN		changes beam energy to R1 (in MeV)
	fast	adjusts beam energy quickly to R1
	incr	increments energy by previously defined step size
	nomic	does not write new energy to microprocessor
	step	changes step size to N1 (in eV)
FIXPT		changes value of channel N2 of data area N1 to N3
MQ		used to enter the reaction kinematic factors
	cal	used to enter the calibration reactions
	wind	used to enter the spectra window reactions
RWND		rewinds the tape N1 runs
	all	rewinds the tape to the load point and then unloads the tape
SPECTPLOT		plots data area N1 on the HP plotter
STRIP		reads N1 data runs from the tape and calculates the yields

Table A.2 - continued

Command	Options	Description
SUBPRO		controls the master subprocesses
	act	sets which subprocess is to be awakened after preset is reached
	create	starts a master subprocess
	delete	stops a master subprocess
	list	lists the master subprocesses
WINDOW		controls the window parameters
	change	allows the individual adjustment of any window parameter
	init	initializes the window parameters
	set	sets winlo and winhi to correspond to windows set with the DISP program
	shift	sets windows to correspond to current window parameters and beam energy
XDUMP		writes data areas 1-9 (the spectra) and data area 947 to tape.
	mark	writes a file mark at the current tape position
XREAD		reads the spectra stored on tape
YC		calculates yields and provides information from the yield curves
	N1	yield curve channel index set to N1
	en	shows energy and yield for the yield curve points selected by the cursor
	i	increments the yield curve channel index by N1
	rn	shows the run number and yield for the yield curve points selected by the cursor
	su	calculates yields and places values in the yield curves
	su list	calculates yields and lists them on the screen for window N1. It does not place the values in the yield curves
YCAXIS		sets the horizontal display limits to N1 and N2 of all the yield curves (data areas 10-99)
YCPLOT		plots the yield versus energy for the HP plotter.

APPENDIX B

Results extracted from the (p,α_0) angular distributions rely heavily on knowledge of the spin, parity, and total width of the resonances studied. From these parameters and the angular distributions, the partial widths are then determined. For these reasons, several adjustments were made not only to the resonances studied, but also to nearby resonances in order to obtain the best fit to the reaction cross sections. Table B.1 lists the changes made to the resonance parameters of ^{40}Ca as a result of the analysis completed for this experiment. The values of the widths presented in this table often were calculated from the angular correlation equations, and are presented here for comparison only. These widths have not been rounded to the appropriate number of significant digits. The dashed lines in the table indicate groups of resonances which were analyzed together. Table B.2 lists the total number of resonances for each J^{π}.

Table B.1

Comparison of ^{40}Ca Resonance Parameters obtained by Bull (1989) and Warthen (1987)

Bull (1989)			Warthen (1987)			
E_p (MeV)	J^π	laboratory widths Γ_{sl} (eV)	E_p (MeV)	J^π	laboratory widths Γ_{sl} (eV)	comments
2.2446	1^-		2.2444	1^-		
		Γ_{11} 2026.			Γ_{11} 1200.	satisfactory 1^- resonance
		Γ_{21} 220.				
		Γ_{23} 153				
		Γ_α 16.			Γ_α 10.	
2.2455	1^+		2.2453	1^+		
		Γ_{10} 520.			Γ_{10} -300.	
		Γ_{22} 140.			Γ_α 3.5	
2.3891	2^+		2.3891	2^+		
		Γ_{20} -337.			Γ_{20} -400.	satisfactory 2^+ resonance
		Γ_{12} 13.			Γ_{22} 40.	
		Γ_α 3.5			Γ_α 10.	
2.4076	1^-		2.4076	1^-		
		Γ_{11} -942.			Γ_{11} 1200.	satisfactory 1^- resonance
		Γ_{21} 259.			Γ_{21} -280.	
		Γ_{23} 15.			Γ_{23} 20.	
		Γ_α 58.			Γ_α 60.	
2.5130	2^+		2.5130	2^+		
		Γ_{20} -4.			Γ_{12} 36.	satisfactory 2^+ resonance
		Γ_{12} 39.			Γ_{22} 144.	
		Γ_{22} -137.			Γ_α 5.5	
		Γ_α 4.3				
2.5154	3^-		2.5154	1^-		
		Γ_{21} 1400.			Γ_{21} 1493.	changed J^π
		Γ_{23} 150.			Γ_{23} -107.	
		Γ_α 5.			Γ_α 10.	
2.5982	2^+		2.5982	2^+		
		Γ_{20} 32.			Γ_{20} -36.	satisfactory 2^+ resonance
		Γ_{12} -3.			Γ_{12} 12.	
		Γ_{22} -5.			Γ_{22} 12.	
		Γ_α 5.			Γ_α 2.	

Table B.1 - Continued

Bull (1989)			Warthen (1987)			
E_p (MeV)	J^π	laboratory widths Γ_{sl} (eV)	E_p (MeV)	J^π	laboratory widths Γ_{sl} (eV)	comments
2.6522	1^-		2.6529	1^-		
		Γ_{11} 647.			Γ_{11} 2300.	satisfactory 1^- resonance
		Γ_{21} 3962.			Γ_{21} 2700.	
		Γ_{23} -9.			Γ_α -40.	
		Γ_α -33.				
2.6539	3^+		2.6539	1^+		
		Γ_{12} 100.			Γ_{22} 700.	changed J^π
		Γ_{22} 50.				
2.6711	1^-		2.6713	1^-		
		Γ_{11} 158.			Γ_{11} 200.	satisfactory 1^- resonance
		Γ_{21} 2419.			Γ_{21} 1800.	
		Γ_{23} -6.			Γ_α -8.	
		Γ_α 10.				
2.6720	2^-					
		Γ_{11} 100.				new resonance
2.6859	2^+		2.6859	2^+		
		Γ_{20} 203.			Γ_{20} 120.	satisfactory 2^+ resonance
		Γ_{12} 12.			Γ_{12} 30.	
		Γ_{22} -1			Γ_α 8.	
		Γ_α -11.				
2.7392	3^-		2.7392	3^-		
		Γ_{21} 300.			Γ_{21} 200.	adjusted widths
		Γ_α 3.			Γ_α 2.	
			2.7406	3^-		
					Γ_{21} 200.	resonance deleted*
					Γ_α 0.8	
			2.7646	1^-		
					Γ_{21} 1000.	resonance deleted
					Γ_α -10.	
2.7647	3^-		2.7651	3^-		
		Γ_{21} 300.			Γ_{21} 100.	adjusted widths
		Γ_α 17.			Γ_α 12.	

Table B.1 - Continued

Bull (1989)			Warthen (1987)			
E_p (MeV)	J^π	laboratory widths Γ_{sl} (eV)	E_p (MeV)	J^π	laboratory widths Γ_{sl} (eV)	comments
2.7859	2^+		2.7859	2^+		
		Γ_{20} 480.			Γ_{20} 450.	satisfactory 2^+ resonance
		Γ_{22} -21.			Γ_{22} 50.	
		Γ_α -2.			Γ_α 1.	
2.8623	2^+		2.8623	0^+		
		Γ_{20} 10.			Γ_{22} 100.	changed J^π
		Γ_{12} 18.			Γ_α 32.	satisfactory 2^+ resonance
		Γ_{22} 12.				
		Γ_α 5.5				
3.0114	2^+		3.0114	2^+		
		Γ_{20} 12.			Γ_{20} 30.	satisfactory 2^+ resonance
		Γ_{12} 200.			Γ_{12} -300.	
		Γ_{22} 113.			Γ_{22} -50.	
		Γ_α -16.			Γ_α -25.	
3.0705	2^+		3.0705	2^+		
		Γ_{20} -450.			Γ_{20} 450.	satisfactory 2^+ resonance
		Γ_{12} 23.			Γ_{12} 23.	
		Γ_{22} -0.5			Γ_α 50.	
		Γ_α 41.				
3.0781	2^+					
		Γ_{12} 40.				new resonance
		Γ_{22} 20.				
3.0793	1^-		3.0795	1^-		
		Γ_{11} 1064.			Γ_{11} 2000.	satisfactory 1^- resonance
		Γ_{21} 234.			Γ_{21} 2000.	
		Γ_{23} -126.			Γ_α 30.	
		Γ_α 24.				
			3.1120	1^+		
					Γ_{10} 200.	resonance deleted
					Γ_{12} 500.	
3.1153	2^-		3.1167	2^-		
		Γ_{11} 1000			Γ_{11} 1000.	changed E_p
		Γ_{21} 3400.			Γ_{21} 3400.	

Table B.1 - Continued

Bull (1989)			Warthen (1987)			
E_p (MeV)	J^π	laboratory widths Γ_{sl} (eV)	E_p (MeV)	J^π	laboratory widths Γ_{sl} (eV)	comments
3.1157	2^+		3.1157	2^+		
		Γ_{20} 4.			Γ_{12} 20.	satisfactory 2^+ resonance
		Γ_{12} 18.			Γ_{22} 68.	
		Γ_{22} 66.			Γ_α 100.	
		Γ_α 100.				
3.1322	2^+		3.1322	2^+		
		Γ_{20} -2401.			Γ_{20} 2500.	satisfactory 2^+ resonance
		Γ_{12} 64.			Γ_{12} 50.	
		Γ_{22} 35.			Γ_α 60.	
		Γ_α 65.				
3.1883	2^+		3.1883	2^+		
		Γ_{20} 8.			Γ_{12} 160.	satisfactory 2^+ resonance
		Γ_{12} -145.			Γ_{22} 40.	
		Γ_{22} 46.			Γ_α 12.	
		Γ_α 15.				
3.1984	1^-		3.1990	1^-		
		Γ_{11} 1707.			Γ_{11} 2000.	satisfactory 1^- resonance
		Γ_{21} 3587.			Γ_{21} 3000.	
		Γ_{23} 214.			Γ_α 340.	
		Γ_α 306.				
3.2005	2^-					
		Γ_{11} 120.				new resonance
3.2032	1^+		3.2033	1^+		
		Γ_{10} -437.			Γ_{10} 350.	
		Γ_{12} 313.			Γ_{12} 250.	
3.2125	2^+		3.2125	2^+		
		Γ_{12} -133.			Γ_{12} 30.	satisfactory 2^+ resonance
		Γ_{22} 151.			Γ_{22} 200.	
		Γ_α -143.			Γ_α 150.	
3.2173	1^-		3.2173	2^+		
		Γ_{11} 10.			Γ_{20} 20.	changed J^π
		Γ_{21} 40.			Γ_{12} 1.	
		Γ_{23} 10.			Γ_{22} 5.	
		Γ_α 300.			Γ_α -100.	

Table B.1 - Continued

Bull (1989)			Warthen (1987)			
E_p (MeV)	J^π	laboratory widths Γ_{sl} (eV)	E_p (MeV)	J^π	laboratory widths Γ_{sl} (eV)	comments
3.2681	2^+		3.2681	2^+		
		Γ_{20} 240.			Γ_{20} 350.	satisfactory 2^+ resonance
		Γ_{12} -230.			Γ_{12} 150.	
		Γ_{22} 30.			Γ_α 100.	
		Γ_α 115.				
3.2964	2^+		3.2964	2^+		
		Γ_{20} 600.			Γ_{20} 400.	adjusted widths
		Γ_{12} 120.			Γ_{12} 67.	
		Γ_α 39.			Γ_{22} 133.	
					Γ_α -17.	
3.2978	3^-		3.2979	1^+		
		Γ_{13} 40.			Γ_{10} 900.	changed J^π
		Γ_{21} 550.				
		Γ_{23} 40.				
		Γ_α 5.				
3.3010	2^-		3.3010	2^-		
		Γ_{11} 16000.			Γ_{11} 18000.	adjusted widths
		Γ_{21} 2000.				
3.3331	2^+		3.3331	2^+		
		Γ_{20} 104.			Γ_{20} 80.	satisfactory 2^+ resonance
		Γ_{22} 76.			Γ_{22} 100.	
		Γ_α 45.			Γ_α 40.	
3.3591	2^+		3.3591	2^+		
		Γ_{20} -1.			Γ_{20} -30.	satisfactory 2^+ resonance
		Γ_{12} 117.			Γ_{12} 110.	
		Γ_{22} 131.			Γ_{22} 110.	
		Γ_α 29.			Γ_α 30.	
3.3671	3^-		3.3671	1^-		
		Γ_{21} 100.			Γ_{21} 700.	changed J^π
		Γ_α 26.			Γ_α 160.	
3.3847	4^+		3.3849	3^+		
		Γ_{22} 950.			Γ_{12} 700.	changed J^π

Table B.1 - Continued

Bull (1989)			Warthen (1987)			
E_p (MeV)	J^π	laboratory widths Γ_{sl} (eV)	E_p (MeV)	J^π	laboratory widths Γ_{sl} (eV)	comments
3.3855	2^+		3.3852	2^+		
		Γ_{20} 11.			Γ_{20} 360.	satisfactory 2^+ resonance
		Γ_{12} 13.			Γ_{12} 80.	
		Γ_{22} 46.			Γ_{22} 360.	
		Γ_α -15.			Γ_α 10.	
3.4038	2^+		3.4037	2^+		
		Γ_{20} 49.			Γ_{12} 200.	satisfactory 2^+ resonance
		Γ_{12} -228.			Γ_α 2.	
		Γ_{22} 324.				
		Γ_α 1.5				
3.4092	3^-					
		Γ_{21} 450.				new resonance
		Γ_{23} -150.				
3.4105	2^+		3.4104	2^+		
		Γ_{20} -1500.			Γ_{20} 1800.	satisfactory 2^+ resonance
		Γ_α -91.			Γ_α 110.	
3.4190	1^-		3.4190	1^-		
		Γ_{11} 10.			Γ_{11} 20.	satisfactory 1^- resonance
		Γ_{21} 49.			Γ_{21} 40.	
		Γ_{23} 16.			Γ_α 1500.	
		Γ_α 1140.				
3.4347	2^+		3.4347	2^+		
		Γ_{20} 159.			Γ_{20} 160.	satisfactory 2^+ resonance
		Γ_{12} -14.			Γ_{22} 20.	
		Γ_{22} 7.			Γ_α 600.	
		Γ_α 765.				
3.4651	1^-		3.4663	1^-		
		Γ_{11} -53.			Γ_{11} 100.	satisfactory 1^- resonance
		Γ_{21} 104.			Γ_{21} 200.	
		Γ_{23} 171.			Γ_α 2.	
		Γ_α 4.5				

Table B.1 - Continued

Bull (1989)			Warthen (1987)			
E_p (MeV)	J^π	laboratory widths Γ_{sl} (eV)	E_p (MeV)	J^π	laboratory widths Γ_{sl} (eV)	comments
3.4665	2^+					
		Γ_{20} 150.				new resonance
		Γ_α -2.				
3.4903	3^+		3.4905	1^+		
		Γ_{12} 380.			Γ_{12} 400.	changed J^π
		Γ_{22} -20				
3.4905	1^-		3.4904	1^-		
		Γ_{11} 1571.			Γ_{11} 448.	adjusted widths
		Γ_{21} 992.			Γ_{21} -179.	
		Γ_α 750.			Γ_{23} 13.	
					Γ_α 3000.	
3.4922	1^+					
		Γ_{10} -200.				new resonance
		Γ_{12} 100.				
3.4982	2^-		3.4982	2^-		
		Γ_{11} 3750.			Γ_{11} 3000.	adjusted widths
3.5021	2^+		3.5023	2^+		
		Γ_{20} 728.			Γ_{20} 240.	satisfactory 2^+ resonance
		Γ_{22} 22.			Γ_α 600.	
		Γ_α 316.				
3.5047	4^+		3.5048	2^+		
		Γ_{22} 30.			Γ_{20} 38.	changed J^π
		Γ_α -40.			Γ_{22} 12.	
					Γ_α -500.	
3.5092	1^-		3.5097	1^-		
		Γ_{11} -2299			Γ_{11} 540.	satisfactory 1^- resonance
		Γ_{21} 492.			Γ_{21} 160.	
		Γ_{23} 39.			Γ_α -2500.	
		Γ_α 733.				
3.5131	2^-					
		Γ_{23} 250.				new resonance
3.5136	3^-		3.5137	1^-		
		Γ_{13} 70.			Γ_{21} 100.	changed J^π
		Γ_{21} 30.			Γ_{23} 200.	
		Γ_α 25.			Γ_α 50.	

Table B.1 - Continued

Bull (1989)			Warthen (1987)			
E_p (MeV)	J^π	laboratory widths Γ_{sl} (eV)	E_p (MeV)	J^π	laboratory widths Γ_{sl} (eV)	comments
3.5490	2^+		3.5491	2^+		
		Γ_{20} 1864.			Γ_{20} 2473.	satisfactory 2^+ resonance
		Γ_{12} -317.			Γ_{12} 450.	
		Γ_{22} 23.			Γ_{22} 77.	
		Γ_{α} -343.			Γ_{α} -440.	
3.5702	3^+		3.5702	1^+		
		Γ_{12} -400.			Γ_{10} 200.	changed J^π
		Γ_{22} 90.			Γ_{12} 900.	
		Γ_{24} 90.				
3.5720	2^+		3.5720	2^+		
		Γ_{20} 42.			Γ_{20} 160.	satisfactory 2^+ resonance
		Γ_{12} -153.			Γ_{12} 160.	
		Γ_{22} 573.			Γ_{22} 960.	
		Γ_{α} 969.			Γ_{α} 600.	
3.5727	3^-		3.5727	3^-		
		Γ_{21} 372.			Γ_{21} 200.	adjusted widths
		Γ_{13} 84.			Γ_{13} 60.	
		Γ_{23} 75.			Γ_{α} 2.	
		Γ_{α} -2.				
3.5817	3^-		3.5819	1^-		
		Γ_{13} 100.			Γ_{11} 2100.	changed J^π
		Γ_{21} -1200.			Γ_{21} 900.	
		Γ_{23} 100.			Γ_{23} 500.	
					Γ_{α} -30.	
3.5924	2^+		3.5924	1^-		
		Γ_{20} 6.			Γ_{11} 50.	changed J^π
		Γ_{12} 17.			Γ_{21} 4.	satisfactory 2^+ resonance
		Γ_{22} 47.			Γ_{23} -40.	
		Γ_{α} 231.			Γ_{α} -140.	
3.6180	2^+		3.6180	2^+		
		Γ_{20} 315.			Γ_{20} 500.	satisfactory 2^+ resonance
		Γ_{12} -3.			Γ_{22} -80.	
		Γ_{22} -7.			Γ_{α} 60.	
		Γ_{α} -60.				

Table B.1 - Continued

Bull (1989)			Warthen (1987)			
E_p (MeV)	J^π	laboratory widths Γ_{sl} (eV)	E_p (MeV)	J^π	laboratory widths Γ_{sl} (eV)	comments
3.6196	1^+		3.6196	1^+		
		Γ_{10} 100.			Γ_{10} 300.	adjusted widths
		Γ_{12} 700.			Γ_{12} 500.	
		Γ_{22} 500.			Γ_{22} 500.	
3.6315	4^+		3.6314	4^+		
		Γ_{22} 30.			Γ_{22} 30.	adjusted widths
		Γ_{24} -30.			Γ_α 2.	
		Γ_α 2.				
3.6326	3^-		3.6326	2^+		
		Γ_{21} 15			Γ_{20} 5.	changed J^π
		Γ_α 175.			Γ_{22} 5.	
					Γ_α 30.	
3.6348	2^+		3.6349	2^+		
		Γ_{20} 428.			Γ_{20} 300.	satisfactory 2^+ resonance
		Γ_{12} -21.			Γ_α 250.	
		Γ_α 421.				
3.6408	1^-		3.6408	1^-		
		Γ_{11} 76.			Γ_{21} -270.	satisfactory 1^- resonance
		Γ_{21} 433.			Γ_{23} 30.	
		Γ_{23} -123.			Γ_α -15.	
		Γ_α 12.				
3.6886	2^+		3.6886	2^+		
		Γ_{20} 1854.			Γ_{20} 1700.	satisfactory 2^+ resonance
		Γ_{12} 331.			Γ_{12} 250.	
		Γ_{22} 15.			Γ_{22} 250.	
		Γ_α 2.5			Γ_α 2.5	
3.6990	1^+		3.6993	1^+		
		Γ_{10} 600.			Γ_{10} 400.	adjusted widths
		Γ_{22} 200.			Γ_{22} 400.	
3.7073	3^-		3.7073	3^-		
		Γ_{21} 500.			Γ_{21} 400.	adjusted widths
		Γ_{23} -100.			Γ_{23} -80.	
		Γ_α 20.			Γ_α 9.	

Table B.1 - Continued

Bull (1989)			Warthen (1987)			
E_p (MeV)	J^π	laboratory widths Γ_{sl} (eV)	E_p (MeV)	J^π	laboratory widths Γ_{sl} (eV)	comments
3.7094	1^-		3.7095	1^-		
		Γ_{23} 700.			Γ_{11} 80.	adjusted widths
		Γ_α 8.			Γ_{23} 320.	
					Γ_α 8.	
3.7232	2^+		3.7236	2^+		
		Γ_{20} 370.			Γ_{20} -600.	adjusted widths
		Γ_{22} 130.			Γ_{12} 200.	
					Γ_{22} 200.	
					Γ_α 5.	
3.7236	1^-					
		Γ_{11} 400.				new resonance
		Γ_{21} 50.				
		Γ_{23} 50.				
		Γ_α 7.				
3.7350	1^+		3.7350	1^+		
		Γ_{12} 600.			Γ_{12} 800.	adjusted widths
3.7362	2^+		3.7362	2^+		
		Γ_{20} -38.			Γ_{20} -80.	satisfactory 2^+ resonance
		Γ_{12} -123.			Γ_{12} 104.	
		Γ_{22} 79.			Γ_{22} 56.	
		Γ_α 18.			Γ_α 30.	
3.8348	2^+		3.8350	2^+		
		Γ_{20} -580.			Γ_{20} -840.	adjusted widths
		Γ_{12} 120.			Γ_{12} 100.	
		Γ_α -200.			Γ_{22} 60.	
					Γ_α 150.	
3.8356	4^+		3.8355	2^+		
		Γ_{22} 300.			Γ_{20} -100.	changed J^π
		Γ_{14} 400.			Γ_{12} 400.	
		Γ_α 10.			Γ_{22} 560.	
					Γ_α 100.	

Table B.1 - Continued

Bull (1989)			Warthen (1987)			
E_p (MeV)	J^π	laboratory widths Γ_{sl} (eV)	E_p (MeV)	J^π	laboratory widths Γ_{sl} (eV)	comments
3.8447	2^-					
		Γ_{11} 300.				new resonance
		Γ_{13} 200.				
		Γ_{21} 500.				
3.8457	1^-		3.8447	1^-		
		Γ_{11} -939.			Γ_{11} 2400.	satisfactory 1^- resonance
		Γ_{21} 336.			Γ_{21} 600.	
		Γ_{23} 4.			Γ_α 70.	
		Γ_α 36.				
3.9108	2^+		3.9108	2^+		
		Γ_{20} 946.			Γ_{20} 1800.	
		Γ_{22} 55.			Γ_{12} 200.	
		Γ_α -240.			Γ_α -300.	
3.9481	1^-		3.9482	1^-		
		Γ_{11} -113.			Γ_{11} 80.	satisfactory 1^- resonance
		Γ_{21} 126.			Γ_{21} 90.	
		Γ_{23} -3.5			Γ_{23} 30.	
		Γ_α 66.			Γ_α 20.	
3.9508	4^+		3.9508	2^+		
		Γ_{22} 300.			Γ_{12} 840.	changed J^π
		Γ_{14} 100.			Γ_{22} 560.	
		Γ_α -10.			Γ_α 100.	
3.9636	2^+		3.9636	2^+		
		Γ_{20} 871.			Γ_{20} 800.	satisfactory 2^+ resonance
		Γ_{12} -100.			Γ_{12} 200.	
		Γ_{22} 29.			Γ_α 200.	
		Γ_α 238.				
3.9982	2^+		3.9982	2^+		
		Γ_{22} 273.			Γ_{22} 100.	
		Γ_α -929.			Γ_α -2500.	
4.0164	4^+		4.0162	4^+		
		Γ_{22} 30.			Γ_{22} 20.	adjusted widths
		Γ_α 30.			Γ_α 10.	

Table B.1 - Continued

Bull (1989)			Warthen (1987)			
E_p (MeV)	J^π	laboratory widths Γ_{sl} (eV)	E_p (MeV)	J^π	laboratory widths Γ_{sl} (eV)	comments
4.0178	1^-	Γ_{11} -549 Γ_{21} 441. Γ_{23} -16. Γ_α 1083.	4.0175	1^-	Γ_{11} 600. Γ_{21} 400. Γ_α 1000.	satisfactory 1^- resonance

* Warthen's data indicates a resonance at E_p = 2.7406 MeV, but the present data over the same energy region shows no sign of this resonance.

Table B.2

Number of Resonances Observed in the $^{39}K(p,p)$ and $^{39}K(p,\alpha_0)$ Reactions

J^π	(p,p)	(p,α_0)
0^+	16	14
0^-	6	–
1^+	37	–
1^-	47	41
2^+	49	41
2^-	38	–
3^+	5	–
3^-	27	26
4^+	29	27
4^-	0	–
Total	254	149

APPENDIX C

Table C.1 lists the errors and covariances of the reduced widths for the 2^+ resonances in ^{40}Ca. These values were computed utilizing the error equations for reduced widths derived by Shriner (1983) and based on standard error propagation analysis. The quantities required for these calculations are the errors in the mixing parameters ξ and ψ_2 and the widths Γ_p and Γ_α. Since MULTI makes no assessment of the errors, σ_{Γ_p} and σ_{Γ_α} were estimated to be a certain percentage of the widths, based on the magnitude of the widths. These errors were estimated as follows:

$$\begin{aligned}
&\text{if} \quad 50\ \text{eV} \le \Gamma, && \sigma_\Gamma = 0.1\Gamma \\
&\text{if} \quad 30\ \text{eV} \le \Gamma < 50\ \text{eV}, && \sigma_\Gamma = 0.15\Gamma \\
&\text{if} \quad 20\ \text{eV} \le \Gamma < 30\ \text{eV}, && \sigma_\Gamma = 0.2\Gamma \\
&\text{if} \quad \Gamma < 20\ \text{eV}, && \sigma_\Gamma = 0.25\Gamma.
\end{aligned}$$

The errors of each channel are summarized in Table C.2. Here, the average reduced widths is compared with the average error in each channel. None of the averaged errors were greater than 25% of the average reduced width.

Table C.1

Errors and Covariances* for the Reduced Widths of 30 2^+ Resonances in ^{40}Ca

E_p (MeV)	$\sigma_{\gamma_p^2}$	$\sigma_{\gamma_\alpha^2}$	$\sigma_{\gamma_{20}^2}$	$\sigma_{\gamma_{20}^2\gamma_{12}^2}$ $\sigma_{\gamma_{12}^2}$	$\sigma_{\gamma_{20}^2\gamma_{22}^2}$ $\sigma_{\gamma_{12}^2\gamma_{22}^2}$ $\sigma_{\gamma_{12}^2}$
2.3891	0.45	1.20	0.14	-0.0080 0.42	0.0002 -0.0024 0.02
2.5130	0.57	0.90	0.01	-0.0006 0.18	0.0004 0.0446 0.45
2.5982	0.08	0.74	0.01	-0.0001 0.04	-0.0000 0.0012 0.04
2.6859	0.16	1.20	0.05	-0.0007 0.13	-0.0001 0.0012 0.02
2.7859	0.20	0.15	0.10	0.0000 0.00	0.0011 0.0000 0.15
2.8623	0.15	0.32	0.02	-0.0005 0.06	-0.0012 0.0045 0.09
3.0114	0.39	0.58	0.01	-0.0003 0.25	-0.0005 0.0317 0.15
3.0705	0.16	0.62	0.07	-0.0008 0.14	0.0001 -0.0006 0.02

Table C.1 - Continued

E_p (MeV)	$\sigma_{\gamma_p^2}$	$\sigma_{\gamma_\alpha^2}$	$\sigma_{\gamma_{20}^2}$	$\sigma_{\gamma_{20}^2\gamma_{12}^2}$ $\sigma_{\gamma_{12}^2}$	$\sigma_{\gamma_{20}^2\gamma_{22}^2}$ $\sigma_{\gamma_{12}^2\gamma_{22}^2}$ $\sigma_{\gamma_{12}^2}$
3.1157	0.09	0.89	0.00	-0.0000 0.03	0.0000 0.0010 0.07
3.1322	0.78	0.54	0.34	-0.0347 0.65	0.0032 -0.0291 0.30
3.1883	0.18	0.31	0.01	-0.0001 0.13	-0.0002 0.0057 0.05
3.2125	0.85	0.95	0.15	-0.0155 0.31	-0.0505 0.1095 0.59
3.2681	0.30	0.65	0.04	0.0034 0.20	-0.0030 0.0085 0.14
3.3331	0.11	0.32	0.02	0.0000 0.00	-0.0005 0.0000 0.10
3.3591	0.17	0.26	0.00	0.0000 0.08	-0.0000 0.0063 0.10
3.3855	0.05	0.18	0.00	-0.0000 0.02	-0.0000 0.0004 0.04

Table C.1 - Continued

E_p (MeV)	$\sigma_{\gamma_p^2}$	$\sigma_{\gamma_\alpha^2}$	$\sigma_{\gamma_{20}^2}$	$\sigma_{\gamma_{20}^2\gamma_{12}^2}$ $\sigma_{\gamma_{12}^2}$	$\sigma_{\gamma_{20}^2\gamma_{22}^2}$ $\sigma_{\gamma_{12}^2\gamma_{22}^2}$ $\sigma_{\gamma_{12}^2}$
3.4038	0.40	0.02	0.03	-0.0014 0.18	-0.0014 0.0324 0.24
3.4105	0.16	0.35	0.16	0.0000 0.00	-0.0000 0.0000 0.01
3.4347	0.05	2.80	0.02	-0.0000 0.03	-0.0000 0.0001 0.03
3.5021	0.12	0.96	0.07	0.0000 0.00	-0.0004 0.0000 0.09
3.5490	0.47	0.92	0.18	0.0142 0.34	0.0001 -0.0015 0.12
3.5720	0.39	2.47	0.02	-0.0010 0.12	-0.0000 0.0208 0.31
3.5924	0.04	0.56	0.00	-0.0000 0.01	-0.0000 0.0002 0.03
3.6180	0.07	0.14	0.03	-0.0004 0.05	-0.0001 0.0005 0.02

Table C.1 - Continued

E_p (MeV)	$\sigma_{\gamma_p^2}$	$\sigma_{\gamma_\alpha^2}$	$\sigma_{\gamma_{20}^2}$	$\sigma_{\gamma_{20}^2\gamma_{12}^2}$ $\sigma_{\gamma_{12}^2}$	$\sigma_{\gamma_{20}^2\gamma_{22}^2}$ $\sigma_{\gamma_{12}^2\gamma_{22}^2}$ $\sigma_{\gamma_{12}^2}$
3.6348	0.07	0.92	0.04	-0.0002 0.06	0.0000 -0.0001 0.00
3.6886	0.40	0.01	0.16	0.0110 0.29	0.0003 -0.0017 0.08
3.7362	0.11	0.09	0.01	-0.0001 0.06	-0.0007 0.0025 0.07
3.9108	0.13	0.28	0.07	0.0000 0.00	-0.0005 0.0000 0.09
3.9636	0.14	0.25	0.07	0.0005 0.09	-0.0001 0.0001 0.06
3.9982	0.13	0.91	0.00	-0.0000 0.05	0.0000 0.0035 0.09

*Errors are in units of keV and covariances are in units of $(keV)^2$

Table C.2

Average Value and Error of the Reduced Widths for 30 2^+ Resonances in ^{40}Ca

Channel	$\langle\gamma^2\rangle$ (keV)	$\langle\sigma_{\gamma^2}\rangle$ (keV)	$\langle\sigma_{\gamma^2}\rangle/\langle\gamma^2\rangle$
γ_p^2	1.74	0.25	0.14
γ_α^2	5.42	0.68	0.13
γ_{20}^2	0.53	0.06	0.11
γ_{12}^2	0.60	0.13	0.22
γ_{22}^2	0.61	0.12	0.20

BIBLIOGRAPHY

Bevington, P. R. Data Reduction and Analysis for the Physical Sciences. New York: McGraw-Hill, 1969.

Biedenharn, L. C. "Angular Correlations" in Ajzenberg-Selove, F. Nuclear Spectroscopy, Part B. New York: Academic Press, 1960.

Biedenharn, L. C. and Rose, M. E. Rev. Mod. Phys. 25, 729 (1953).

Bilpuch, E. G., Lane, A. M., Mitchell, G. E., and Moses, J. D. Phys. Reports 28C, 147 (1976).

Blatt, J. M. and Biedenharn, L. C. Rev. Mod. Phys. 24, 258 (1952).

Bohigas, O., Giannoni, M. J., and Schmidt, C. Phys. Rev. Lett. 52, 1 (1984).

Brody, T. A., Flores, J., French, J. B., Mello, P. A., Pandey, A., and Wong, S. S. M. Rev. Mod. Phys. 53, 385 (1981).

Brooks, W. K., Jr. "Proton Resonance Spectroscopy in ^{36}Ar." Ph.D. dissertation, Duke University, 1988.

Chou, B. H., Mitchell, G. E., Bilpuch, E. G., and Westerfeldt, C. R. Phys Rev. Lett. 45, 1235 (1980).

Coester, F. and Jauch, J. M. Helv. Phys. Acta. 26, 3 (1953).

Condon, E. U. and Shortley, G. H. The Theory of Atomic Spectra. Cambridge: Cambridge University Press, 1951.

Devons, S. and Goldfarb, L. J. B. "Angular Correlations" in Handbuch der Physik, Vol. 42, 1957.

Efron, B. SIAM Rev. 21, 460 (1979).

Fano, U. Phys. Rev. 90, 577 (1953).

Ferguson, A. J. Angular Correlation Methods in Gamma-ray Spectroscopy. Amsterdam: North Holland, 1965.

Heisenberg, W. Z. Phys. 120, 513; 673 (1943).

Huby, R. Proc. Phys. Soc. A67, 1103 (1954).

King, S. E., Lau, Y. C., and Gould, C. R. IEEE Trans. Nucl. Sci. NS-28, 3822 (1981).

Krieger, T. J. and Porter, C. E. J. Math. Phys. 4, 1272 (1963).

Lane, A. M. and Thomas, R. G. Rev. Mod. Phys. 30, 257 (1956).

Liou, H. I., Camarda, H. S., Wynchank, S., Slagowitz, M., Hacken, G., Rahn, F., and Rainwater, J. Phys. Rev. C5, 974 (1972).

Mitchell, G. E., Bilpuch, E. G., Shriner, J. F., Jr., and Lane, A. M. Phys. Rep. 117, 1 (1985).

Nelson, R. O., "Proton Resonance Spectroscopy in ^{28}Si and ^{30}P." Ph.D. dissertation, Duke University, 1983.

Nelson, R. O., Bilpuch, E. G., and Mitchell, G. E. Nucl. Instrum. Methods A236, 128 (1985).

Parks, P. B., Newson, H. W., and Williamson, R. M. Rev. Sci. Instrum. 29, 834 (1958).

Porter, C. E. and Thomas, R. G. Phys. Rev. 104, 483 (1956).

Porter, C. E., ed. Statistical Theories of Spectra: Fluctuations. New York: Academic, 1965.

Ramakrishnan, P. K. "Amplitude and Width Correlations in ^{57}Co and ^{49}V." Ph.D. dissertation, North Carolina State University, 1984.

Roberson, N. R. and Gould, C. R. IEEE Trans. Nucl. Sci. NS-32 1447 (1985).

Sellin, D. L. "Excited States in ^{19}F." Ph.D. dissertation, Duke University, 1969.

Shriner, J. F., Jr. "Nuclear Resonance Spectroscopy in ^{45}Sc and ^{40}Ca." Ph.D. dissertation, Duke University, 1983a.

Shriner, J. F., Jr., Bilpuch, E., G., and Mitchell, G. E. Phys. Lett, 130B, 144 (1983b).

Shriner, J. F., Jr., Mitchell, G. E., and Bilpuch, E., G. Nucl. Instrum. and Methods A254, 139 (1987a).

Shriner, J. F., Jr., Mitchell, G. E., and Bilpuch, E., G. Phys. Rev. Lett. 59, 435 (1987b).

Soderstrum, John P., Boyd, Mark A., Gould, C. R., and Roberson, N. R. XSYS Reference Manual, 6th ed. Triangle Universities Nuclear Laboratory, 1987.

Thompson, A. J. and van Rij, W. I. "Notes on Applied Angular Correlation Theory." Florida State University, 1968.

Vanhoy, J. R. "Proton Resonance Spectroscopy in ^{24}Mg." Ph.D. dissertation, Duke University, 1986.

Vogt, E. Rev. Mod. Phys. 34, 723 (1962).

Warthen, B. J. "Proton Resonance Spectroscopy in ^{40}Ca." Ph.D. dissertation, Duke University, 1987.

Watson, W. A., III, Bilpuch, E. G., Mitchell, G. E. Z. Phys. A300, 89 (1981).

Westerfeldt, C. R., Nelson, R. O., Bilpuch, E. G., and Mitchell, G. E. Nucl. Instrum. and Methods A270, 467 (1988).

Weidenmüller, H. A. Comments Nucl. Part. Phys. 16, 199 (1986).

Wigner, E. P. Ann. Math. 53, 36 (1951).

Wigner, E. P. Oak Ridge National Laboratory Report ORNL-2309, 59 (1957).

Wigner, E. P. and Eisenbud, L. Phys. Rev. 72, 29 (1947).

BIOGRAPHY

Jeffrey Scott Bull

Personal: Born July 22, 1961 Knoxville, Tennessee

Education: B. S. Physics, University of the South
M. A. Physics, Duke University

Positions: Teaching Assistant, Duke University, 1983 - 1984
Research Assistant, Duke University, 1984 - present

Abstracts: "Amplitude and Width Correlations in ^{40}Ca," J. S. Bull, C. R. Westerfeldt, E. G. Bilpuch, J. F. Shriner, Jr., and G. E. Mitchell, Bull. Am. Phys. Soc., 32, 2145 (1987).

"A Study of Entrance Channel Correlations in ^{40}Ca," J. S. Bull, C. R. Westerfeldt, E. G. Bilpuch, J. F. Shriner, Jr., and G. E. Mitchell, Bull. Am. Phys. Soc., 33, 2194 (1988).

Memberships: American Physical Society